Karlsruhe Institute of Technology

# Electrostatic Field Simulations and Low-Temperature Measurements for a Xenon-based Dual-Phase Noble Gas Dark Matter Detector

# Elektrostatische Feldsimulationen und Niedrig-Temperatur Messungen für einen auf Xenon-basierenden zwei-phasigen Dunkle Materie Detektor

Master Thesis of

Julien Wulf

At the Department of Physics
Institute of Experimental Nuclear Physics (IEKP)

| | |
|---|---|
| Reviewer: | Prof. Dr. Guido Drexlin |
| Second reviewer: | Prof. Dr. Wim de Boer |
| Advisors: | Prof. Dr. Laura Baudis |
| | Dr. Ferenc Glück |
| | Dipl.-Phys. Daniel Hilk |

Duration: 15. April 2013 – 14. April 2014

# Declaration

I declare that I have developed and written the enclosed thesis completely by myself, and have not used sources or means without declaration in the text.

**Karlsruhe, 14.04.2014**

.....

(**Julien Wulf**)

# Summary

This work has been carried out within the DARWIN (dark matter WIMP search in noble liquids) and XENON1T project. Before building up DARWIN, the XENON collaboration constructs their first ton-scale dual phase detector XENON1T at the Gran Sasso National Laboratory (LNGS) in Italy. Both projects aim to detect dark matter particles via nuclear recoils in liquid noble gases.
A dark matter particle colliding with the liquid target material produces a light and a charge signal. The prompt light signal (S1) is detected with photomultipliers, the ionization electrons drift within the liquid volume from the interaction point to the liquid-gas interface, guided by an electric field of order $\mathcal{O}(1\ \mathrm{kV/m})$. At the liquid-gas interface they get extracted into the gaseous phase via an electric field of order $\mathcal{O}(10\ \mathrm{kV/m})$, where they generate secondary scintillation light (S2), which is proportional to the charge signal. The design of the time projection chamber (TPC) allows the precise three-dimensional reconstruction of the interaction vertex. The ratio S2/S1 has a different value for electron recoils (background) and nuclear recoils (signal) and can be used for background discrimination. The electric fields in this kind of detectors are created by several electrodes. To ensure a maximal homogeneous electrical field, the geometrical properties have to be investigated in advance with detailed electric field simulations.

This work is subdivided into an experimental and theoretical part. The theoretical part has been performed at the Karlsruhe Tritium Neutrino Experiment (KATRIN) of the Karlruhe Institute of Technology. For this experiment, a global analysis and simulation package called *Kasper* has been developed. It has been written primarily in C++, and comprises of a number of semi-independent modules. One module is called *KEMField*, which is a toolkit for solving electrostatic and magnetostatic fields from user-defined electrode and magnet configurations. *KEMField* takes advantage of the boundary element method (BEM), which is used to compute electrostatic fields and potentials from discretized charge densities.
The main goal of the first part of this thesis was to develop a new module for *Kasper* to be able to perform electrostatic field simulations for different kinds of dual-phase detectors. With this module the electrostatic design of the upcoming dark matter experiments, like DARWIN, will be optimized. A first electrostatic simulation with this module was performed with a realistic CAD-based XENON1T model. Within this simulation new field routines had to be implemented into *KEMField* as well.

The experimental part has been performed at the XENON group of the University of

Zürich. The XENON group in Zürich works at the front line for the XENON1T project. The group operates a 2 kg high-purity germanium (HPGe) spectrometer at the Gran Sasso National Laboratory. It is used to screen the XENON1T detector and the shielding components. Besides their activity at LNGS, they have several low temperature experiments in their local laboratories at Zürich. One experiment is called MarmotXL. It is used especially for low temperature measurements of photomultipliers.
The main goal of the second part of this thesis was to make a detail study about a newly developed amplifier in connection with the XENON1T photomultipliers. Therefore these measurements have been performed at low temperature to guarantee the same condition as in the XENON1T experiment. Using an additional amplifier for the PMT signal of XENON1T will result in higher gains at lower voltages, which would allow for higher linearity and lower power consumption. Also a new technique to stabilize the liquid-gaseous xenon interface of a dual-phase detectors has been developed and tested. For both low temperature measurements a special setup has been developed and installed inside the MarmotXL setup.

The present thesis is organized as follows:

1. **Introduction to Dark Matter Physics** This first chapter will give a short introduction into dark matter physics. Common techniques to detect dark matter will be discussed as well. Also the best motivated dark matter particle candidate will be explained.

2. **Direct Detection of Dark Matter with a Dual-Phase Noble Gas Detector** In this chapter the function principle of dual-phase noble gas detectors are explained on the basis of XENON1T. The excellent background reduction factor as well as the role of the electric fields inside this kind of detectors will be emphasized.

3. **Numerics and Algorithms of Electrostatic Field Simulations** The tools and algorithms, which have been used in context of this thesis, will be presented in this chapter. Especially the boundary element method (BEM) and the Robin Hood solver will be discussed in detail.

4. **Validation of the Numerical Field Computation Program** In this chapter a simple plate capacitor and wire capacitor will be discussed. One of the goals of this test is to show that the boundary element method has been successfully extended for dielectrics. Another goal is to show that the BEM is more advantageous than the finite element method (FEM) for large-scale geometries containing small-scale structures. This chapter also shows the successful implementation of a parallelized BEM solver into *KEMField*, which allows us now to calculate on modern parallelized computing platforms.

5. **Realization of a Electrostatic Field Computations for the XENON1T Detector** This chapter will first introduce the new DARWIN module and its implementation into *Kasper*. With this new software component, simulations of large dual phase detectors can be performed fast and precisely. To test the module, a complex exact CAD-based model of the XENON1T detector has been implemented and successfully simulated. The computation results will be discussed and the software implementation of the new modules for dual phase TPCs into the KATRIN software *Kasper* will be explained.

6. **Low-Temperature Hardware Tests for the XENON1T Experiment** This chapter will show the performed hardware tests for XENON1T in Zürich. Especially a low-temperature amplifier PMT test and a bell test will be discussed. The amplifier PMT test has the goal to study the behaviour of the 3" Hamamatsu model R11410 PMT in connection with an newly developed amplifier. With the bell test a new

technique to stabilize the liquid-gaseous interface of dual phase detectors will be investigated. For these tests new experimental setups have been developed at the MarmotXL detector. The setups and the results will be presented in this chapter.

7. **Conclusion** The last chapter gives a summary of the thesis and a short outlook.

# Zusammenfassung

Diese Arbeit wurde innerhalb des DARWIN (Dark Matter WIMP Search in Noble liquids) und dem XENON1T Experiment durchgeführt. Das XENON1T Experiment befindet sich zurzeit in der Aufbauphase am Gran Sasso National Laboratory (LNGS) in Italien und wird nach seiner Fertigstellung der erste zwei-Phasen Dunkle Materie Detektor mit einem sensitiven Volumen von über einer Tonne sein. Das DARWIN- Projekt hingegen befindet sich zurzeit noch in der Planungs- und Entwicklungsphase, geleitet von einem Konsortium, bestehend aus führenden Wissenschaftlern auf dem Gebiet der Dunklen Materie. Beide Experimente haben das Ziel, Dunkle Materie direkt über eine Streuung an flüssigen Edelgasatomen zu detektieren.
Bei einer Streuung von der Dunklen Materie mit flüssigen Edelgasatomen werden dabei Szintillationslicht und frei werdende Elektronen erzeugt. Das prompt erzeugte Szintillationslicht (S1) wird mithilfe von Photomultipliern detektiert, die Elektronen hingegen driften innerhalb des flüssigen Volumens, durch ein angelegtes elektrisches Feld von der Größenordnung $\mathcal{O}(1$ kV/m), vom Wechselwirkungspunkt zur flüssig-gasförmigen Grenzschicht. An der flüssig-gasförmigen Grenzschicht werden die Elektronen über ein elektrisches Feld von der Ordnung $\mathcal{O}(12$ kV/m ) in die Gasphase extrahiert, wo sie ein zweites Szintillationslichtsignal (S2) erzeugen. Dieses Szintillationslicht (S2) ist proportional zu dem Ladungssignal. Das Design dieser Zeitprojektionskammer (TPC) erlaubt die präzise dreidimensionale Rekonstruktion des Wechselwirkungspunktes. Das Verhältnis S2/S1 hat einen unterschiedlichen Wert für eine Elektronen-Streuung (Hintergrund) und eine Kern-Streuung (Signal) und kann aus diesem Grund für die Hintergrunddiskriminierung verwendet werden. Die elektrischen Felder in dieser Art von Detektoren werden durch mehrere Elektroden erzeugt. Um ein maximal homogenes elektrische Feld im TPC sicherzustellen, müssen die geometrischen Eigenschaften im Voraus mit detaillierten elektrostatischen Simulationen untersucht werden.

Diese Arbeit ist in einen experimentellen und theoretischen Teil untergliedert. Der theoretische Teil wurde dabei in der Gruppe des Karlsruher Tritium Neutrino Experiment (KATRIN) am Karlsruhe Institute of Technology durchgeführt. Für das KATRIN Experiment wurde ein globales Analyse und Simulations Paket namens Kasper entwickelt. Es ist in der Programmiersprache C++ geschrieben und besteht aus einer Reihe von unabhängigen Modulen. Eines dieser Module heißt *KEMField* und ist ein leistungsfähiges Programm zum Berechnen von elektrischen und magnetischen Feldern von beliebigen Geometrien. *KEMField* benutzt für diese Simulationen die Randelement Methode (BEM). Dabei werden die elektrische Felder und Potentiale über diskretisierte Ladungsdichten

berechnet.
Das Ziel im ersten Teil dieser Arbeit war es ein neues Modul für Kasper zu entwickeln, welches es ermöglicht, elektrostatische Simulationen für verschiedene zwei-Phasen Detektoren durchzuführen. Mit diesem neuem Modul kann die nächste Generation von Dunkle Materie Detektoren hinsichtlich des elektromagnetischen Designs optimiert und analysiert werden. Eine erste Simulation mit dem neu entwickelten Modul wurde für das XENON1T Experiment erfolgreich durchgeführt.

Der experimentelle Teil dieser Arbeit wurde in der XENON Gruppe an der Universität Zürich durchgeführt. Die XENON Gruppe in Zürich arbeitet an vorderster Front für das XENON1T Projekt. Die Gruppe betreibt am Gran Sasso National Laboratory ein Halbleiterdetektor bestehend aus 2 kg hochreinem Germanium (HPGe). Dieses wird verwendet, um genau die Untergrundrate der verschiedenen Teile vom XENON1T Detektor zu bestimmen. Neben ihrer Tätigkeit am LNGS, hat die XENON Gruppe mehrere Experimente in ihrem lokalen Labor in Zürich. Hier werden fundamentale Fragen für das XENON1T Experiment nachgegangen. Dafür haben sie mehrere Tieftemperatur Teststände. Ein Teststand wird MarmotXL genannt und wird hauptsächlich für Tieftemperatur-Messungen von Photomultipliern verwendet.
Das Ziel im zweiten Teil dieser Arbeit war es, einen neu entwickelten Verstärker für das PMT Signal im XENON1T Experiment zu untersuchen. Diese Messungen wurden bei tiefen Temperaturen am MarmotXL Detektor durchgeführt, um die Experimente bei gleichen Bedingungen wie im XENON1T Experiment durchzuführen. Des Weiteren wurde eine neue Technik entwickelt und getestet, um die flüssig-gas Grenzschicht in zwei-phasigen Zeitprojektionskammern zu stabilisieren. Für beide niedrig-Temperaturmessungen wurde ein eigens dafür entwickelt Messapparatur entwickelt und am MarmotXL in Betrieb genommen.

# Contents

# 1. Introduction to Dark Matter Physics

In the 20th century, several astronomical observations, such as studies of the rotational velocity of spiral galaxies, the gravitational lensing effect and redshift measurements of galaxy clusters, have discovered anomalies which can only been explained by assuming a large amount of non-luminous matter or a modified theory of gravitation. This non-luminous matter is called dark matter. The first pioneers in the research of dark matter were Vera Rubin and Fritz Zwicky.
In our current understanding of the universe only $\sim 6\%$ of the matter is baryonic, the other 94% matter is dark-energy (72%) and dark matter ($\sim 24\%$) [BHS05]. The evidence that dark matter is non-baryonic results from the nucleosynthesis and the cosmic microwave background (CMB) [Oli03]. It also has to be weakly interacting supported by upper-limits on the self-interaction from astrophysical observations.
This chapter will give a short overview of today's questions of dark matter. Evidences and predictions for dark matter will be discussed, followed by a presentation of possible dark matter candidates. The chapter will be closed by an overview of the possibilities to detect dark matter.

## 1.1. Observational Evidences for Dark Matter

The first observation of dark matter in our universe made Fritz Zwicky 1933 during his study of galaxy clusters, in particular during redshift measurements of the Coma cluster [Zwi33]. He used two different techniques to calculate the mass of the cluster. He took advantage of the virial theorem to calculate the mass of the Coma cluster. The viral theorem is the relation between the average total kinetic energy and the average total gravitational potential for a stable, self-gravitating, spherical distribution of equal mass objects [H.14]:

$$\frac{M_{tot} \cdot v^2}{2} = \frac{G \cdot M_{tot}^2}{4 \cdot R_{tot}}, \tag{1.1}$$

where $M_{tot}$ is the mass of the system consisting of N individual objects, $R_{tot}$ the radius of the system, $v$ the average velocity and $G$ the gravitational constant. By measuring the true overall extent of the system $R_{tot}$ and the mean square of the velocities of the individual objects that comprise the system $v$, the virial mass of the system can be calculated as follows:

$$M_{tot} = \frac{2 \cdot R_{tot} \cdot v^2}{G}. \tag{1.2}$$

The second technique to calculate the mass of the Coma cluster measures the luminosity of the galaxies. In this case, the mass is defined by the mass–luminosity relation:

$$L \propto M^{3.33}. \tag{1.3}$$

The calculated mass from the virial theorem showed that there is more mass in the cluster than seen by the mass–luminosity relation, which indicates the presence of large quantities (>90%) of invisible mass. These measurements were also performed for 89 other galaxy clusters. They all showed an average mass-to-light ratio of 230-250 [GBG$^+$00].
Another evidence for dark matter has been found during the analysis of rotational curves of stars and gas in disk galaxies by Vera Rubin [RF70]. For this analysis the redshift has been measured as a function of the distance to the galactic center. The relation between the circular velocity and mass is given by:

$$v(r) = \sqrt{\frac{G \cdot M(r)}{r}}. \tag{1.4}$$

The majority of luminous mass of the galaxy is located in the center. Hence it is expected that circular velocities of stars should scale as $r^{-1/2}$. Nevertheless this is for the most galaxies not the case. Figure 1.1 shows the circular velocity over the distance to the galactic center of galaxy NGC 6503. It was observed that the rotational curves of the most spiral galaxies are flat. But the stellar density falls of exponentially at large radii. Therefore this indicates the existence of non-luminous matter, which is superimposed to the luminous matter. To explain the behaviour of the rotational curves, a dark matter halo with a mass density proportional to $r^2$ was assumed [BBS91]. The sum of the visible

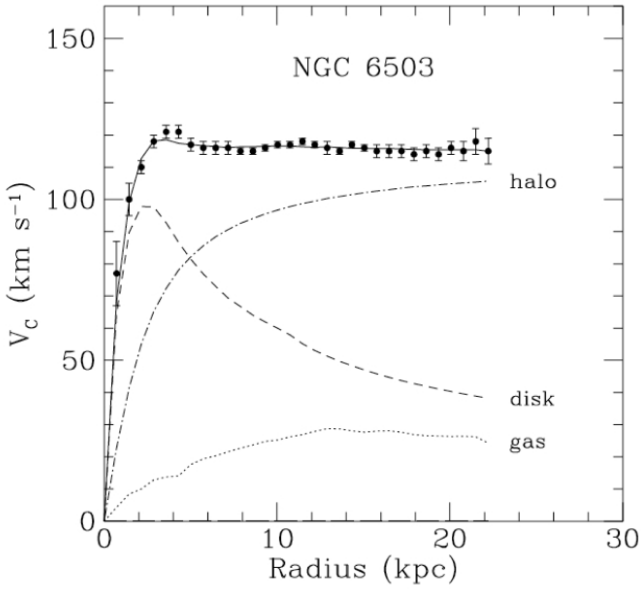


Figure 1.1.: The measured rotation curve of the galaxy NGC 6503. The rotational velocity profiles for the individual components of gas, stars, and the dark matter halo are shown, too. Figure taken from [BBS91].

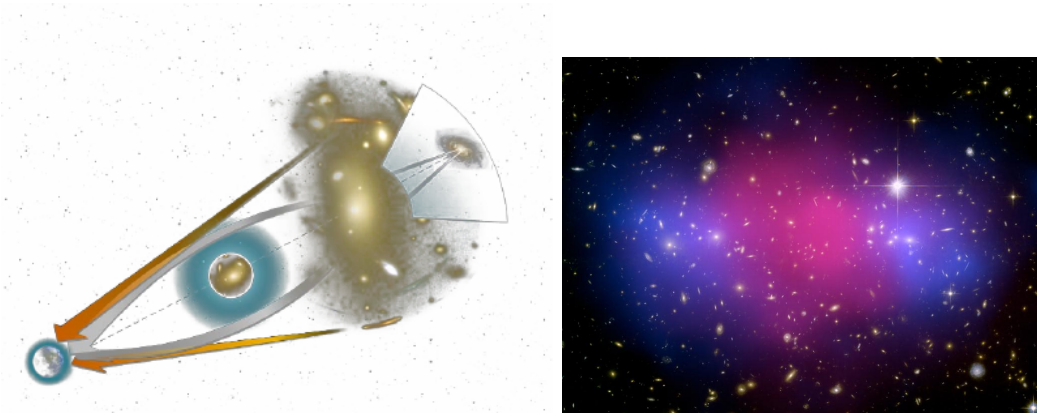

(a) The gravitational lensing effect (b) The Bullet cluster

Figure 1.2.: (a) The gravitational lensing. The galaxy cluster acts as a lens for the light coming from the galaxy behind it. (b) The Bullet cluster with two colliding galaxy clusters. The dominant cluster mass is shown in blue. The hot gas clouds of the clusters is shown in pink. This effect is explained by dark matter. Figures modified from [NAS13].

matter in the disk, the hydrogen gas and the dark matter in the halo reproduces the observed rotation curve.
An additional evidence for dark matter is the effect of gravitational lensing. A huge mass collection like a galaxy or a galaxy cluster acts as a lens for the light emitted from a more distant galaxy [Bar10]. Thereby multiple images of the background galaxy are visible. Figure 1.2 illustrates this effect.
By observing collisions of galaxy clusters and using the gravitational lensing effect, dark matter were observed. The gas clouds of the two clusters is heating up during the collision and interacts electromagnetically, the hot gas clouds slow down and emit X-rays. The stars and galaxies pass one by another without influences on each other and have different dynamics during the collision compared to the hot interstellar gas. An example of this type of collision is a collision inside the Bullet cluster (1E0657-558) shown in Figure 1.2. The clouds of hot gas are far away from the parent clusters and are indicated in pink color. The remaining clusters show a discrepancy in the gravitational lensing, indicated in blue, which is explained with dark matter [CBG$^+$06]. The Bullet cluster shows that most of the mass in the cluster pair is in the form of collisionless dark matter.
Another popular evidence for dark matter is the cosmic microwave background (CMB). The CMB is the radiation left over from an early stage in the development of the universe. Approximatively 300.000 years after the Big Bang the universe cooled down so that protons and electrons have been able to combine to form neutral atoms. These atoms could no longer absorb the thermal radiation and so the universe became transparent. The today's temperature spectrum of the CMB gives us information on the energy density at the time of decoupling. The experiments COBE [Smo99], WMAP [B$^+$13] and PLANCK [A$^+$13a] measured the CMB. With the data from WMAP it is possible to calculate the matter composition in our universe. The total matter density was measured to $\Lambda_m = 0.266 \pm 0.029$ and the baryonic matter density was measured to $\Lambda_b = 0.0449 \pm 0.0028$ [B$^+$13].
By measuring astrophysical systems at sizes ranging from galactic to universal scales, the standard cosmological model ($\Lambda$CDM) has been developed. In this model 4.6% of the universe consists of baryonic matter, 23% consists of dark matter, which does not emits or absorb light and the remaining 72% is the dark energy, which is responsible for the present acceleration of the expansion of the universe [Dur11].

## 1.2. Dark Matter Particle Candidates

A candidate for non-baryonic matter as dark matter is the neutrino [Ber00]. There is also a relic neutrino background in the universe, similar to the CMB. Measurements of $\beta$-decay showed an upper limit on neutrino mass to $< 2.05$ eV (95% C.L.) [F$^+$98] [OW08].
The KATRIN experiment has the goal to determine the mass of the electron anti-neutrino by examining the shape of the tritium-$\beta$-spectrum close to its endpoint. The experiment will be able to to set an upper limit of the neutrino mass of 0.2 eV/$c^2$ [Col04].
With this upper mass the relic Neutrinos from the Big Bang have a total density of $\Lambda_\nu < 0.07$ [B$^+$13]. This density is too small to be the dominate component of the dark matter. On the other hand with Neutrinos as the main component of dark matter, the large structure in the universe could not been explained. The neutrino component of dark matter is also called hot dark matter, because these particles travelled with a relativistic speed at the time of decoupling.
Another favoured candidate for dark matter is the *weakly interacting particle* (WIMP). It is a thermal relic of the big bang and weakly interacting. Shortly after the Big Bang the WIMPs were in thermal equilibrium with the rest of the universe. The Boltzmann equation describes the time evolution of the density $n_\chi$ of the WIMPs after the Big Bang [JKG96]:

$$\frac{dn_\chi}{dt} + 3Hn_\chi = -\langle\sigma_A v\rangle\,[(n_\chi)^2 - (n_\chi^{eq})^2], \tag{1.5}$$

where $n_\chi$ is the density of $\chi$ particles, $\langle\sigma_A \cdot v\rangle$ is the thermally averaged total cross section for annihilation times the relative velocity and $H = \frac{\dot{a}}{a}$ is the Hubble expansion rate. The left side describes the density in an expanding universe. The first term in the brackets describes the WIMP annihilation and the second term the WIMP creation. We see from figure 1.3, if the rate of the annihilation drops below the expansion rate $\Gamma = H$, the WIMPs stop to annihilate, fall out of equilibrium and the relic WIMPs remain. The present mass density of the WIMPs in units of the critical density is given by [JKG96]

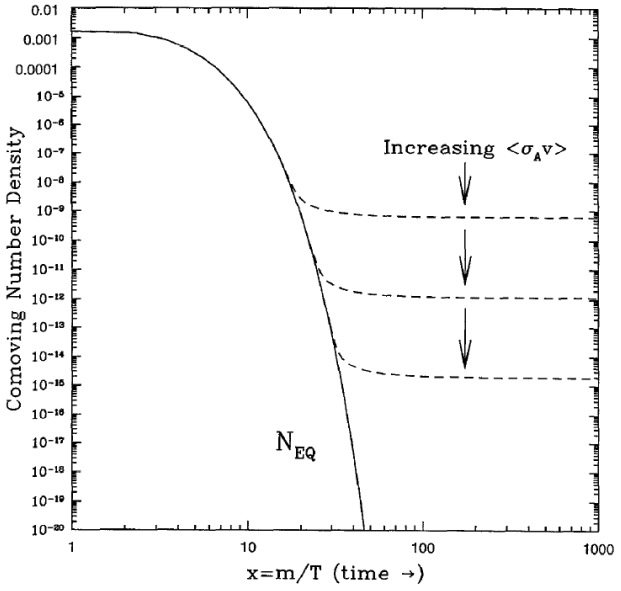


Figure 1.3.: The numerical solutions of the Boltzmann equaion. The equilibrium (solid line) and actual (dashed lines) abundances per comoving volume are plotted as a function of $x = \frac{m}{T}$. Figure taken from [JKG96]

$$\Lambda_\chi h^2 = \frac{m_\chi n_\chi}{\rho_c} = \frac{3 \cdot 10^{-27} cm^3 s^{-1}}{\langle \sigma_A v \rangle}, \tag{1.6}$$

where $\rho_c$ is the critical density and $m_\chi$ the mass of the WIMP. The cross section for annihilation $\sigma_A$ becomes very small on the level of weak interaction. With the today's observed total density for $\Lambda_\chi$, the mass for this hypothetical particle has a range from 1 GeV to 1 TeV.
The standard model of particle physics (SM) doesn't consist of a possible WIMP candidate. One of the best motivated particle is the Neutralino, which comes from the supersymmetry theory (SUSY). SUSY is an extension of the standard model and unifies the three fundamental forces of nature (electromagnetic, weak, and strong nuclear interactions) [Bil01]. The Neutralino is the lightest supersymmetric particle (LSP), stable and weak interacting. It is stable because of a new conserved quantum number, called R-parity in the SUSY theory [JKG96]:

$$R = (-1)^{3B+L+2S}, \tag{1.7}$$

where B is the Baryon number, L is the Lepton number and S is the particle spin. Because of the conserved R-parity, the supersymmetric particle is produced in pairs. Also a mixture between SUSY particles and SM particles is not possible and heavy SUSY particles can only decay in other SUSY particles [Lah07].

## 1.3. Detection Methods for Dark Matter

To confirm the theory of dark matter it is a major goal of experimental astro physicists to detect possible dark matter candidates, like weakly interacting massive particles. Therefore different kinds of techniques were developed to detect dark matter indirectly and directly. The aim is also to study the properties of dark matter such as their mass, lifetime, and coupling, in experiments at high energy particle colliders.

### 1.3.1. Indirect Detection

Dark matter can be detected indirectly by measuring the secondary particles produced by a WIMP annihilation reaction. The particles of interest are $\gamma$-rays, Neutrinos, Positrons and Antiprotons [BCP$^+$13]. The annihilation rate is given by the following equation [JKG96]:

$$N_{Ann} \propto \langle \sigma_A \cdot v \rangle \frac{\rho_\chi}{m_\chi}. \tag{1.8}$$

WIMP annihilation reactions are expected mainly in regions with a high dark matter density, like the galatic center, the sun or in the dwarf galaxies.
To the detect the low energy $\gamma$-rays (<1TeV), space telescopes are used. The $\gamma$-rays will interact with the matter via production of electron-positron pairs. After a conversion, the trajectories of the resulting electron and positron are measured by particle tracking detectors, and their energies are measured afterwards by a calorimeter [BUB98]. Such a space telescope is the Fermi Large Area Telescope (LAT) [A$^+$12b], which has been launched into the orbit and is currently taking data.
To detect the high energy $\gamma$-rays (>100GeV), on-ground installed Cherenkov telescopes are used. These telescopes observe the night sky for Cherenkov light emitted from charged particles. The Cherenkov light is produced in the upper atmosphere ($\propto$ 10km). Where an high-energy (TeV) $\gamma$-ray may produce an electron-positron pair with an enormous velocity.

The Cherenkov radiation from these charged particles is used to determine the source and intensity of the cosmic $\gamma$-ray. Examples of experiments are HESS [Bar13], MAGIC [A$^+$11a] and CTA [A$^+$13d].
Further, Muon Neutrinos from a WIMP annihilation can be produced in the core of the sun, which can escape and produce ultra relativistic Muons in terrestrial targets. These Muons can be detected in large water- or ice-based neutrino telescopes, which detect the produced Cherenkov light via photomultipliers. Examples of experiments are Super-Kamiokande [KW11] and ICECube [A$^+$12a].
To detect the positrons and antiprotons, particle detectors in the orbit are used. The main components of such particle detector are a magnet with a silicon microstrip tracker that provides momentum and the sign charge of the particle, a calorimeter for the energy and lepton-hadron separation and a time of flight module (ToF) to measure the velocity and charge of the particle. Examples of this kind experiments are AMS-02 [ILS14] and PAMELA [A$^+$13b].

### 1.3.2. Direct Detection

It is evident that our galaxy contains of another form of matter: The dark matter. We should be able to detect these particles directly via their interactions with nuclei in terrestrial targets. A WIMP elastically scatters off a nucleus in the target material, causing it to recoil [GW85]. The energy deposition can be transformed into a measurable signal, such as scintillation light, charge or heat [JKG96].
There are several experiments which try to detect such an event. Figure 1.4 shows the different experiments and their detection technique. The most experiments try to detect two different signals to get a better background discrimination. This is necessary because the expected event is very low and the background is very high. Qualitatively the expected event Rate R can be calculated simply with the following formula [PRSZ09]:

$$R = n_\chi N_t \langle v \rangle \sigma, \tag{1.9}$$

where R ist the event rate, $N_t$ the number of target nuclei, $n_\chi$ the local WIMP density, $\langle v \rangle$ is the average speed of the WIMP relative to the target and $\sigma$ is the cross section for the WIMP scattering averaged. More accurately, one should take into account the facts that the WIMPs move within the halo with velocities determined by $f(v)$, that the differential

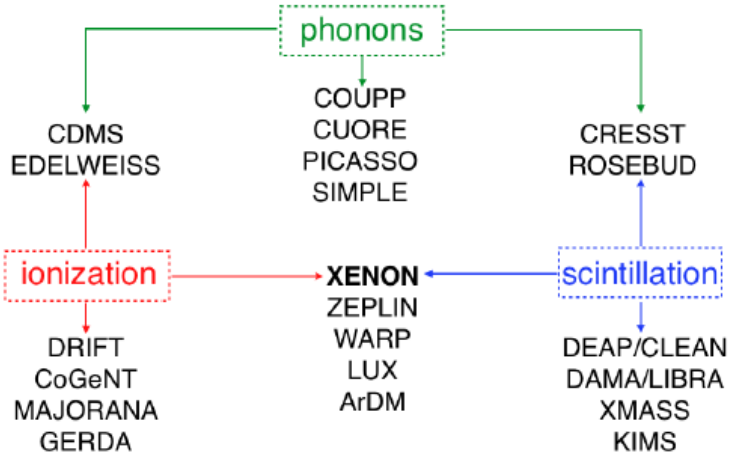


Figure 1.4.: Measurable signals from particle interactions and a chart of experiments for direct dark matter detection categorized by different measurement technique. Figure taken from [Kis11].

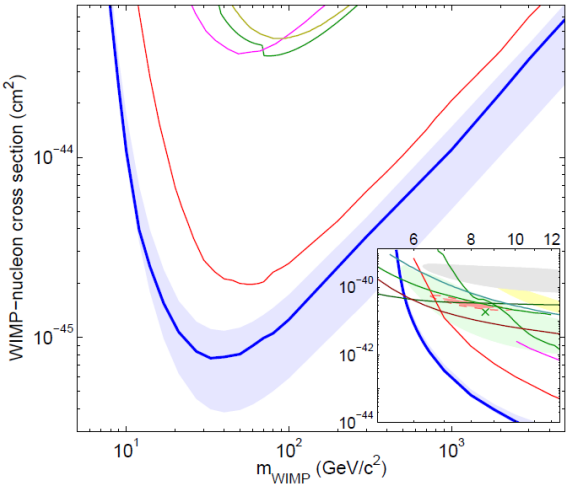


Figure 1.5.: The LUX 90% confidence limit on the spin-independent elastic WIMP-nucleon cross section (blue). Also the results of Edelweiss II (dark yellow line), CDMS-II (green line), ZEPLIN-III (magenta line), CDMSlite (dark green line), XENON10 (brown line), SIMPLE (light blue line), XENON100 100 live-day (orange line) and XENON100 225 live-day (red line) are shown. The inset (same axis units) also shows the regions measured from annual modulation in CoGeNT (light red, shaded), along with exclusion limits from low threshold re-analysis of CDMS II data (upper green line), allowed region from CRESST-II (yellow shaded) and DAMA/LIBRA allowed region. [D$^+$13] Figure taken from [D$^+$13].

cross section depends through a form factor $F$ and that detectors have a threshold energy $E_t$ [JKG96].
The different experiments make a common assumption for the galactic dark matter profile to make their results more comparable. They assume for the galactic dark matter profile an isothermal profile with a flat rotation curve, a local density of 3 $GeV/cm^2$ and a Maxwell-Boltzmann velocity distribution.
In this context we have to shortly discuss the results of the DAMA/LIBRA experiment who claims for the discovery of dark matter particles. They saw a modulation of the differential event rate over the year. The earth's motion around the sun results in an annual modulation of the WIMP flux ($\phi = n_\chi \cdot v$) over the year because the earth's speed relative to the galactic rest is largest in summer and lowest in the winter. But this result is in conflict with the null-results of other experiments. [BBC$^+$13]
There are two different WIMP-nucleon interactions. For the studies of spin-independent (scalar) interactions, heavy atoms are preferred as target material ($\sigma \propto A^2$). For spin-dependent (axial-vector) interactions, where the WIMP is expected to couple to unpaired nuclear spins J, the cross section is proportional to ($\sigma \propto J \cdot (J+1)$) [Kis11].
The best spin-independent cross section in the world delivers experiments based on noble elements. Using noble elements such as xenon and argon have several advantages. The elements are not very expensive, have a relative high density and have high scintillation and charge yields [Hit05]. XENON100 [E$^+$12], WARP [B$^+$05], LUX [A$^+$13c] and ArDM [M$^+$11] are such experiments. These detectors are double phase detectors, which detect scintillation and ionization signals. Figure 1.5 shows the current exclusion plot from different experiments. The best exclusion limit in the world delivers LUX. The XENON1T [Apr12] and DARWIN [Bau12] dark matter detector is the next generation of such a double phase detector and have the aim to improve the exclusion limit. The detailed explanation of XENON1T is covered in chapter 2.

### 1.3.3. Production of Dark Matter Particles in Collider Experiments

WIMPs can be produced in high energy particle accelerators. High energy colliders are for example the Large Hadron Colider (LHC) and Tevatron [BFH10]. The advantage to use such a collider is that they do not suffer from astrophysical uncertainties and they are sensitive to small dark matter masses [Kis11]. In such a collider, supersymmetric particles can be produced by either of two protons (LHC) or of a proton and anti-proton (TEVATRON). Because of the conserved R-parity, the supersymmetric particle is produced in pairs. The lightest supersymmetric particle is stable and can not decay in the detector volume. Due to the very low cross section, the dark matter candidates appear as missing energy [FHKT12]. But dark matter searches at high energy particle colliders must be complemented by direct and indirect detection experiments. Even if a WIMP is discovered in a collider, the existence of the galactic dark matter halo will still have to be proven by other experiments.

# 2. Direct Detection of Dark Matter with a Dual-Phase Noble Gas Detector

The XENON1T experiment, which will be installed in the Laboratori Nazionali del Gran Sasso (LNGS) is the third generation experiment within the XENON program. It follows the XENON100 [E$^+$12] experiment and it is designed to detect directly the dark matter via nucleon-WIMP scattering. The latest results of the XENON100 experiment has provided a limit of exclusion of the spin-independent WIMP-nucleon cross-section with the minimum of $2 \cdot 10^{-45}$ $cm^2$ for a 55 GeV WIMP mass [A$^+$12c]. The LUX experiment confirmed this measurement and pushed this limit down to a minimum of $7.6 \cdot 10^{-46}$ $cm^2$ for 55 GeV WIMP mass [D$^+$13]. The aim of the XENON1T experiment is to reach a sensitivity of down to $2 \cdot 10^{-47}$ $cm^2$ in 2 years of operation. This sensitivity will be achieved by using a target mass of 3 tons, a significant reduction of the background of one magnitude to XENON100 ($10^{-4}$ $events \cdot kg^{-1} \cdot day^{-1} \cdot keV^{-1}$) in the target volume and by using an innovative design with a careful selection of the construction materials [Apr12] [Kis11] [A$^+$11b]. XENON1T is based on a dual phase time-projection chamber (TPC), providing information on the 3D vertex of particle interactions. This chapter gives an introduction into the XENON1T experiment. The detection principle and the detector design will be explained more in detail. The DARWIN project aims to build such a xenon detector on a multi-ton basis.

## 2.1. Function Principle of Dual-Phase Noble Gas Detectors

The XENON1T detector has the aim to measure the scintillation signal and the ionisation signal of a nucleon-WIMP scattering. The target material is liquid xenon. The noble gas xenon has many advantages for particle detection. It is an efficient and fast scintillator. The high density of liquid xenon (3 $g/cm^3$) provides a good self-shielding and a compact detector geometry. The absence of long-lived radioactive isotopes ensures that an ultra-low background level can be achieved [Kis11].
When a WIMP interacts with a xenon atom, the energy transfer is split between ionization, excitation and heat. The scintillation light can be produced on two different ways. The recoiled xenon atom gets excited, combines with another atom and produces an excited diatomic molecule [JKG96]. In the subsequent de-excitation it releases a photon with a wavelength of 178 nm, in the vacuum ultra-violet (VUV) region. Described by the following equations:

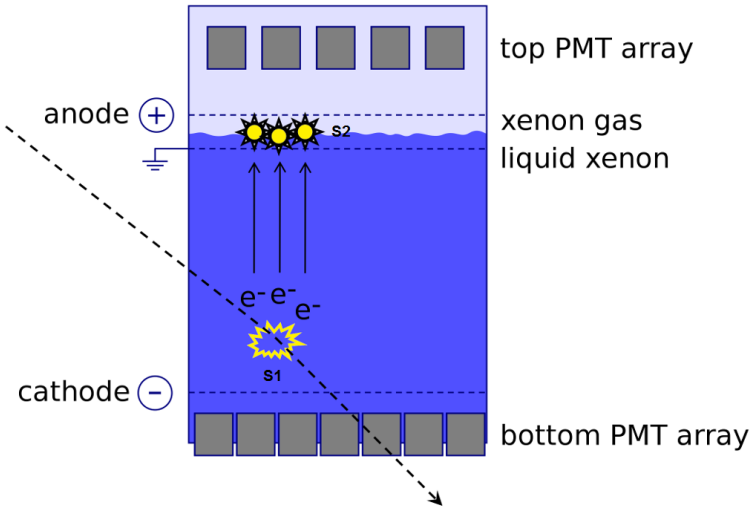


Figure 2.1.: Particle detection principle with the XENON1T detector. The WIMP scatters at the xenon atom and creates a prompt scintillation light (S1). The ionization electrons are removed from the interaction side with a drift field $E_d$, extracted into the gas phase with an electric field $E_g$ and there detected as scintillation light (S2). Figure modified from [col14].

$$Xe^* + Xe \rightarrow Xe_2^* \tag{2.1}$$
$$Xe_2^* \rightarrow 2Xe + h\nu \tag{2.2}$$

Also some of electron-ion pairs produced by ionization recombine and VUV photons are also emitted through an excimer (excited dimer) when it decays back to the ground state. Described by the following equations:

$$Xe^+ + Xe \rightarrow Xe_2^+ \tag{2.3}$$
$$Xe_2^+ + e^- \rightarrow Xe^{**} + Xe \tag{2.4}$$
$$Xe^{**} \rightarrow Xe^* + heat \tag{2.5}$$
$$Xe^* + Xe \rightarrow Xe_2^* \tag{2.6}$$
$$Xe_2^* \rightarrow 2Xe + h\nu \tag{2.7}$$

The scintillation light has two components with different decay time constants. A fast component with a decay time of 2.2 ns corresponding to the decay of the singlet state of the excited dimer and a slow component with a decay time of 27 ns of the triplet state of the excited dimer [DHK+02] [HTF+83]. Xenon atoms do not absorb their own scintillation light, because the scintillation light comes from the decay of the excimer state.
Figure 2.1 shows a schematic description of a particle detection in the double phase xenon detector XENON1T. The nucleon-WIMP scattering produces a prompt scintillation light (S1) and gets detected by photomultiplier tubes (PMTs) on the top and bottom of the target volume. With an applied electric field $E_d$ across the liquid xenon target, some of the ionization electrons are removed from the interaction site, do not recombine and can be detected independently from the S1 light signal. These electrons are drifted and extracted into the gas phase above the liquid xenon target, and accelerated with a high electric field $E_g$, producing an electro-luminescence signal (S2) via collisions with xenon atoms, which is detected by PMT arrays above and below the target volume.
WIMPs are expected to elastically scatter of xenon nuclei resulting in low energy nuclear

recoils (NR). Neutrons with energies in $MeV$ range passing through the detector also produce low energy nuclear recoils, whereas $\gamma$-rays and electrons produce electronic recoils (ER). Because of the different $\frac{dE}{dx}$, the energy deposition of NR and ER results in different probabilities of electron-ion pairs recombination, and thus different ratios of the yield of scintillation light and ionization charge. The ratio of the primary (S1) and secondary (S2) scintillation signals provides a possibility to distinguish electronic interactions (background) from nuclear recoils (signal), and to reject the electromagnetic background [A$^+$14]. Also the time difference between the S1 and S2 signals provides information about on the z-coordinate of the interaction. If a particle has deposited energy at multiple places in the target, then two or more S2 pulses are recorded. Such an event is a multiple scatter event and is rejected due to its very low scattering cross-section of the WIMPs. [Kis11]

## 2.2. Design of the Time Projection Chamber of the XENON1T Detector

This section shows the design of the XENON1T detector. All informations are taken from [Col10]. Other sources are marked.

### 2.2.1. Geometric Design of XENON1T

The XENON1T detector is projected to contain a total amount of three tons of liquid xenon with a fiducial volume after cuts of 1 ton. This liquid xenon is inside the vacuum insulated cryostat made of low activity stainless steel [Col10]. Figure 2.2 shows the current CAD-Drawing of the XENON1T detector. The TPC is defined by a structure made of polytetrauoroethylene (PTFE, Teflon) and copper and is viewed by two arrays

Figure 2.2.: The CAD-Drawing of the XENON1T detector. The TPC is enclosed in a vacuum insulated cryostat. The signal and high voltage cables for the PMTs are installed through a main feed through at the top of the detector. For the high voltage supply of the cathode a separate feed through is available. Figure taken from [Jam14]

of photomultiplier tubes (PMT). Teflon is used because of its low intrinsic radioactivity and it is a good VUV light reflector [YDK+04]. Furthermore Teflon can be handled very well in low-temperature experiments. One PMT array is installed in the liquid phase at the bottom and the other is installed at the top in the gaseous phase. The bottom PMT array should detect the $S1$ signal and the top PMT array should detect the $S2$ signal. In order to increase the light collection efficiency, the active volume is limited by a PTFE wall [Apr12]. All holders and walls are made of low radioactive PTFE.
The electrons which are created by the WIMP-nucleon scattering, drift upwards by an electric field. This is created by a cathode and 76 field shaping rings made of cooper (A. James, 2013, pers. comm.). At the cathode a voltage of $-100\ kV$ is applied and an homogeneous electric field is generated by applying a potential difference across the field shaping rings. The cathode consists of several parallel wires. In order to shield the bottom PMT array from this electric field, an additional grounded parallel wire electrode is installed below the cathode. The gaseous phase for creation of the proportional scintillation signal is maintained by using a 'diving bell' system. The bell has a slight overpressure to create a constant liquid-gaseous xenon interface. The liquid level can always been adjusted by changing the pressure inside the bell. The height of the liquid level is measured via several capacitive level meters. To extract the electrons across the liquid-gaseous interface an extraction field is created by applying high voltage ($4.5\ kV$) on the anode. The anode consists also of several parallel wires and is installed inside the diving bell. Two additional parallel wire electrodes are installed below and above the anode and are kept at ground potential in order to close the field cage (Gate) and shield the top PMT array from the high electric field. The gap between the grounded electrode and the anode is 5 mm. The liquid level is adjusted between these two electrodes, which gives us an extraction field of $\mathcal{O}(\ 12\ \frac{keV}{cm})$. This field is high enough to obtain an extraction efficiency close to 100% [AGM+04]. The scintillation light $S1$ and $S2$ is detected by 250 (3" Hamamatsu model R11410) PMTs. The top PMT array is inside the diving bell above the anode. The bottom PMT array is installed below the cathode. Both PMTs arrays are installed with a support structure made of PTFE. This support structure holds the PMTs and also increases the collection efficiency of the scintillation light (A. James, 2013, pers. comm.).

### 2.2.2. Light Signal Readout with Photomultipliers

In order to detect the scintillation light $S1$ and $S2$ 3" Hamamatsu model R11410 PMTs are used in the XENON1T experiment [BBF+13]. Figure 2.3 shows the Hamamatsu R11410 PMTs and a schematic of a PMT. These PMTs are optimized with the supplier for low

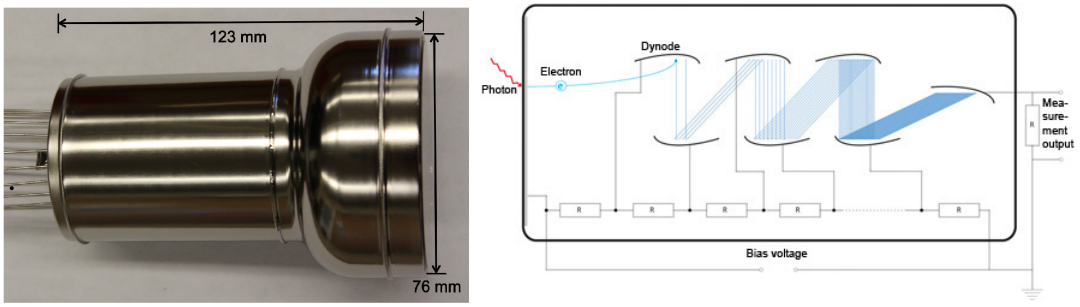


(a) Hamamatsu model R11410 (b) Schematic of a PMT

Figure 2.3.: (a) The Hamamatsu model R11410 PMT. The pins at the bottom of the PMT are for the power supply of the dynodes. Figure taken from [LAB+12]. (b) A schematic of a PMT. The created photoelectron is multiplied by passing every dynode stage. Figure taken from [COM14].

temperature measurements.
The photocathode of the PMT is the negatively charged electrode, that is coated with a photosensitive compound. When this is hit by a photon, the absorbed energy causes electron emission due to the photoelectric effect. These electrons move directly towards the electron multiplier, where electrons are multiplied by the process of secondary emission [cL07]. The electron multiplier consists of a number of other electrodes (dynodes). Each dynode is held at a more positive voltage, than the previous one. The electrons striking the first dynode, more low energy electrons are emitted, and these electrons in turn are accelerated towards the second dynode. The geometry of the dynode chain is such that a cascade occurs with an ever-increasing number of electrons being produced at each stage. This large number of electrons reach the last dynode called anode, where we can measure our signal. The metal body has the same potential as the cathode. So the electrons are forced to go from dynode to dynode.
The R11410 10 photomultiplier tube is a vacuum device with a transparent synthetic silica window and a with 12 stage box and linear-focused style dynode structure. The photocathodes, made of low temperature bialkali have a diameter of 76 $mm$. The dynode structure allows for good collection efficiency, and pulse linearity. The dynodes and photocathode are enclosed in a kovar metal body support structure with a ceramic stem and kovar leads. Intended to be used in extremely low background experiments, the R11410-10 PMT is made from very low radioactive materials. [LAB$^+$12]

### 2.2.3. Shielding of the sensitive Volume against multiple Background Sources

To shield the XENON1T detector against neutrons and muons during operation an enormous water tank was installed at the laboratory Laboratori Nazionali del Gran Sasso. The water tank is equipped with photosensors, which will act as a passive veto against external neutron backgrounds, and as an active muon veto. The water tank with installed photosensors acts as a Cherenkov detector. The water tank has a volume of 700 $m^3$ and the XENON1T detector will be installed in the center of the water tank. Figure 2.4 shows a schematic of the water tank with the XENON1T detector inside. All materials for the construction of the XENON1T detector and the support structure will be screened with a low background Ge detector ('Gator') in order to determine their intrinsic radioactivity [BFA$^+$11].

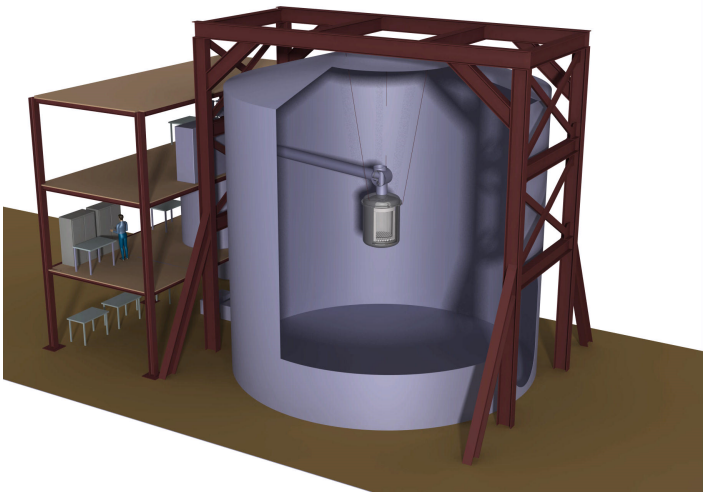

Figure 2.4.: The water tank of the Xenon1T detector. A human is drawn to show the size of the tank. Figure taken from [dS14].

Germanium is used because of the low threshold. The Germanium detector acts like a diode. Only a signal is measured when a electron-hole pair is created. The germanium detectors must be cooled with liquid nitrogen temperatures, because at a higher temperatures the electrons can easily cross the band gap in the crystal and reach the conduction band and produce too much electrical noise. Cooling to liquid nitrogen temperatures reduces thermal excitations of valence electrons so that only a gamma ray interaction can give an electron the energy necessary to cross the band gap and reach the conduction band. The measured activities will be used as an input information for Monte Carlo simulations in order to predict the background from the detector and shield materials. Because of the huge amount of materials it is planned to build up a second low background Ge detector ('Gator-2').

## 2.3. Scientific Goal of the XENON1T Dark Matter Experiment

The aim of the XENON1T experiment is to reach a sensitivity of down to $2 \cdot 10^{-47}\ cm^2$ with 2 years of operation. Figure 2.5 shows the expected exclusion plot with XENON1T. The next generation of xenon based dark matter detector is already in the planing phase (DARWIN/XENONnT) [Bau12]. In the next upcoming years the DARWIN detector should be designed. If this detector will be based on the XENON1T detector a new kind of simulation software is needed to design such huge geometry. The electric fields and electric potential is important for such a study to avoid field emission and to maintain an homogeneous field inside the TPC for a well local resolution. The next chapters shows the used algorithms and developed simulation package for simulations of the upcoming huge dark matter experiments.

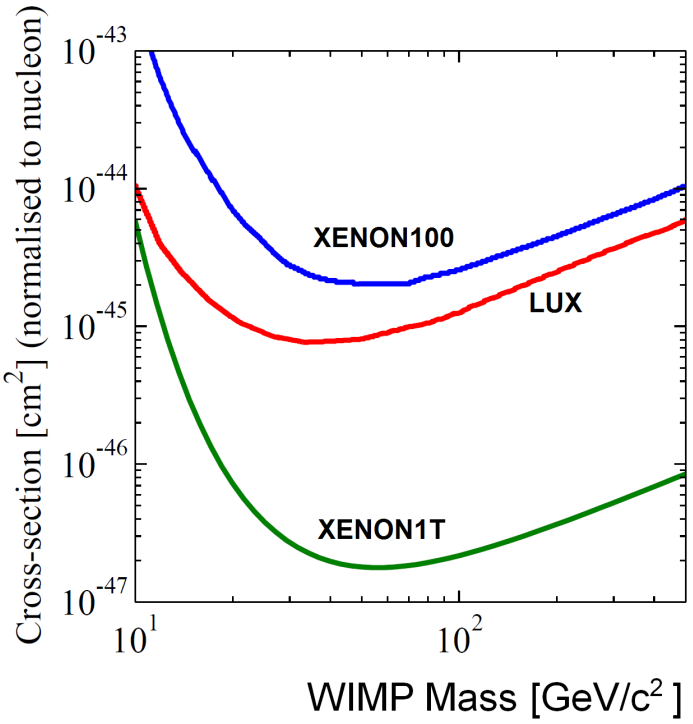


Figure 2.5.: The expected sensitivity of the XENON1T detector (green line). Also the sensitivity of LUX (red line) and XENON100 is drawn. Figure modified from [RM14]

# 3. Numerics and Algorithms of Electrostatic Field Simulations

This chapter gives an overview of numerical computational methods for solving electrostatic problems. There are two common techniques: One is the boundary element method (BEM) and the other is the finite element method (FEM). *COMSOL Multiphysics*, a commercial simulation software, is based on the FEM.
Only the schematic to obtain the electric potential with the FEM will be shown in this chapter. The BEM will be discussed in more detail, because our simulation package *KEMField* [Gro] takes advantage of the BEM. We will use both techniques to solve simple electrostatic problems in chapter 4 with and without dielectrics. For a complex simulation of a dual-phase noble gas detector in chapter 5 we will only use *KEMField*, because his calculation technique.

## 3.1. Numerical Solution Technique of Maxwell's Equation with the FEM

The finite element method is a numerical technique for finding a solution in a domain with boundary values. Therefore we have to discretize the whole computational domain into $N$ finite elements to obtain the electric potential in the inner region. Common elements are tetrahedral in three dimensions and triangles in two dimensions.
The electric potential inside one triangle can be described by the three corner potentials of the triangle: $\phi_1$, $\phi_2$ $\phi_3$. For the case we have only one element the corner potentials are well known. The electric potential inside the triangle is assumed with a linear function by the following equation [Sta14]:

$$\phi_{\text{tri}}(x, y) = c_1 + c_2 \cdot x + c_3 . \cdot y \tag{3.1}$$

x and y stands for the coordinates and $c_1$, $c_2$ and $c_3$ are coefficients. The coefficients $c_1$, $c_2$ and $c_3$ can be expressed by the the corner potentials of the triangle. In this way we obtain a linear equation system for the electric potential inside the triangle:

$$\begin{bmatrix} \phi_1 \\ \phi_2 \\ \phi_3 \end{bmatrix} = \begin{bmatrix} 1 & x_1 & y_1 \\ 1 & x_2 & y_2 \\ 1 & x_3 & y_3 \end{bmatrix} \times \begin{bmatrix} c_1 \\ c_2 \\ c_3 \end{bmatrix} \tag{3.2}$$

After solving for the coefficients we get the potential in one element in terms of the corner potentials. Given by the following formula [FAL93]

$$\phi_{\text{tri}}(x, y) = N_1\phi_1 + N_2\phi_2 + N_3\phi_3. \tag{3.3}$$

Where $N_1$, $N_2$ and $N_3$ are defined interpolation functions from the solution of 3.2.
If we have more than one triangle, we have to set up a global matrix over an additional condition. The calculation of the corner potentials of the triangles becomes then very difficult [Sta14]. Also this matrix gets very huge for a fine discretization and solving this for the node potential needs a large amount of computer memory.
This is a big disadvantage of the FEM. The discretization of the whole computational domain requires a lot of elements.

## 3.2. Numerical Solution Technique of Maxwell's Equation with the BEM

For simulations of large geometries the finite element method is not practicable, because of his huge amount of memory. With the BEM we have to discretize only the surface of the electrodes into several subelements. It is assumed that every element $i$ of the electrode has a constant charge density $\sigma_i$ and a potential $U_i$. The potential $U_i$ is equal to the applied potential $U$. This is called Dirichlet boundary condition. The potential $U_i$ in the center of the element $i$ is given by the sum of the potential contributions of all other elements $j$ [Lei09].

$$U_i = \sum_{j=1}^{N} \phi_{ij} \tag{3.4}$$

The voltages $U_i$ are applied to the electrodes and is known. $\phi_{ij}$ is the potential in the midpoint of subelement i caused by subelement $j$ and is given by:

$$\phi_{ij} = \frac{\sigma_j}{4\pi\epsilon_0} \int d^2 r_j \frac{1}{|\vec{r_i} - \vec{r_j}|}, \tag{3.5}$$

where $\sigma_j$ is the charge density of subelement $j$. After summing over all elements $j$ in equation (3.4) we get the following linear equation system:

$$U_i = \sum_{j=1}^{N} C_{ij}\sigma_j, \tag{3.6}$$

where $C_{ij} = C_j(r_i)$ is the so called Coulomb-matrix-element. It can be seen as the electric potential at the midpoint of subelement i caused by subelement j with constant charge density [Lei09]. It is a geometrical factor given by:

$$C_j(\vec{r_i}) = \frac{1}{4\pi\epsilon_0} \int d^2 r_j \frac{1}{|\vec{r_i} - \vec{r_j}|}. \tag{3.7}$$

We solve equation (3.6) (Eq. (12) in [FLC+11]) for $\sigma$. With these charge distributions, the electric potential due to the entire electrode configuration can be computed in all regions of space over following formula:

$$U(\vec{r}) = \frac{1}{4\pi\epsilon_0} \sum_j \sigma_j \int d^2 r_j \frac{1}{|\vec{r} - \vec{r_j}|} \tag{3.8}$$

After differentiating numerically the electric potential we can obtain the electric field.

$$\vec{E} = -\vec{\nabla} U(\vec{r}) \tag{3.9}$$

Or the field can be found analytically by the following formula:

$$\vec{E} = \frac{1}{4\pi\epsilon_0} \sum_j \sigma_j \int dr_j^2 \frac{\vec{r} - \vec{r_j}}{|\vec{r} - \vec{r_j}|^3} \tag{3.10}$$

With BEM we do not have to discretize the whole volume. This is a big advantage, because we can compute a very large geometry without to getting out of memory due to discretization of empty space. In the following section we extend this formalism for dielectric materials.

### 3.2.1. Extension of the BEM to Dielectrics

For the DARWIN experiment we need to calculate the electrostatic potentials and electric fields in the presence of dielectric media, because we didn't implemented only conductive surfaces. For dielectric media surfaces can not be treated as an equipotential. So we have to derive a solution to integrate dielectrics into the boundary element method. First we focus on the boundary condition at the insulator-insulator interface. The displacement vector $\vec{D}$ is continuous across the surface. If this surface is the boundary between two dielectric materials, then the Maxwell's boundary condition is valid [Gri07]. This is called Neumann boundary condition:

$$\epsilon_i^+ \vec{E}_i^+ \cdot \vec{n}_i - \epsilon_i^- \vec{E}_i^- \cdot \vec{n}_i = 0, \tag{3.11}$$

where $\epsilon^{\pm}$ is the permittivity above and below the surface of the subelement i, $\vec{E}_i^{\pm}$ is the electric field at the sub-element i and $\vec{n}_i$ is the surface normal vector of the interface. The boundary condition can be easily expressed in a matrix equation, just as we did for the scalar potential. So the electrostatic problem in presence of dielectrics is a mixture of dielectric and conducting surfaces, as long as one calculates all contributions to the electric field and electric potential when evaluating the appropriate matrix elements [FLC+11].

## 3.3. Discussion of the Input Geometry of possible Electrostatic Problems

To take advantage of the BEM we have to discretize the electrode surfaces into subelements or called primitives, that have a fixed charge density. For the DARWIN and XENON1T implementation wire segments, rectangles and triangles were used.

### 3.3.1. Wire Segments

A wire segment is defined by its endpoint $\vec{x}_1$, $\vec{x}_2$ and by its diameter $d$. The following derivation of the electric potential is performed under the assumption that $d$ is small compared to the distance between the field point and the wire segment. In addition every wire segment is assumed to have a constant charge density $\lambda$. We define the following scalars $x_1 = |\vec{x}_1 - \vec{x}_0|$ and $x_2 = |\vec{x}_2 - \vec{x}_0|$. So an infinitesimal potential is given by

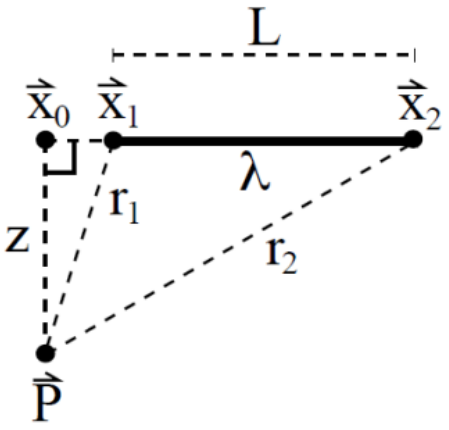


Figure 3.1.: A charged line segment with endpoints $\vec{x}_1$ and $\vec{x}_2$ and charge density $\lambda$, and a field point $P$ with distance $z$ from the line segment. Figure taken form [Cor91].

$$dV = \frac{1}{4\pi\epsilon_0} \cdot \frac{dQ}{r} = \frac{1}{4\pi\epsilon_0} \cdot \frac{\lambda \cdot dx}{\sqrt{x^2 + z^2}} \tag{3.12}$$

Integrating from $x_1$ to $x_2$ leads to.

$$V = \frac{\lambda}{4\pi\epsilon_0} \log\left(\frac{x_2 + r_2}{x_1 + r_1}\right) \tag{3.13}$$

To increase the computational time the equation will be simplified by substituting $L = |\vec{x}_1 - \vec{x}_2|$ (the length of the wire segment) we get the electric potential [Cor91]:

$$V = \frac{\lambda}{4\pi\epsilon_0} \log\left(\frac{r_1 + r_2 + L}{r_1 + r_2 - L}\right). \tag{3.14}$$

Now we have an equation for the electric potential of a wire segment in terms of the length $l$ and the distance $r_1$ and $r_2$.

### 3.3.2. Rectangular Subelements

We define a rectangle sub-element by the position of its corner $P_0$, its side lengths $a$ and $b$ and the unit vectors defining along the sides of the rectangle. Using the coordinates in Figure 3.2 and the substituting $x = u - u_p$, $y = v - v_p$ the electric potential from the rectangle with constant surface charge density $\sigma$ is given by the following equation:

$$V(\vec{P}) = \frac{\sigma}{4\pi\epsilon_0} \int_{-u_p}^{-u_p+a} \int_{-v_p}^{-v_p+b} \frac{1}{\chi} \cdot dx \cdot dy, \tag{3.15}$$

with $\chi = \sqrt{x^2 + y^2 + w_p^2}$. After integrating this equation we get the final analytic solution [Cor91]:

$$\begin{aligned} V(\vec{P}) = & \frac{\sigma}{4\pi\epsilon_0} \cdot (I_2((-u_p + a), (-v_p + b), w_p) - I_2(-u_p, (-v_p + b), w_p) \\ & - I_2((-u_p + a), -v_p, w_p) + I_2(-u_p, -v_p, w_p)), \end{aligned} \tag{3.16}$$

with $I_2(x, y, z) = z \arctan\left(\frac{x}{z}\right) - z \arctan\left(\frac{xy}{z\chi}\right) - x + y \log\left(x + \chi + x\right) \log\left(y + \chi\right)$.

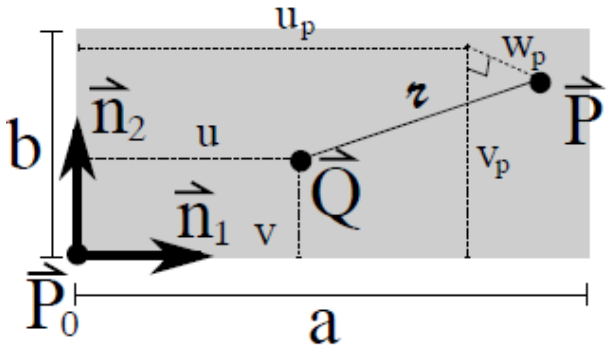


Figure 3.2.: A rectangular subelement defined by the position of a corner $P_0$, the lengths of the sides $a$ and $b$, and the unit vectors in the directions of sides a and b. The field point is defined as $P$, with local coordinates ($u_p$, $v_p$, $w_p$). A point $Q$ located on the surface of the sub-element is shown, with local coordinates (u, v, 0). The distance between $P$ and $Q$ is $\chi$. Figure taken from [Cor91].

### 3.3.3. Triangular Subelements

We define a right triangular subelement by the point $\vec{P}_0$, the lengths of its sides $a$ and $b$ and the unit vectors defining its sides. Using the coordinates in Figure 3.3 we get the integral equation for the potential of a triangle with the surface density $\sigma$.

$$V = \frac{\sigma}{4\pi\epsilon_0} \int_{y_1}^{y_2} \int_{x_1}^{c+my} \frac{1}{\sqrt{x^2+y^2+z^2}} \cdot dx \cdot dy, \tag{3.17}$$

with $c = \frac{x_2y_2+x_1y_1}{y_2-y_1}$ and $m = \frac{x_2-x_1}{y_2-y_1}$. The analytic solution of equation 3.17 is quite complex. After using a common table of integrals and pre-computed indefinite integrals we get [Cor91]:

$$V = \frac{\sigma}{4\pi\epsilon_0} \cdot z[I_3(a', b, u_2) - I_3(a', b, u_1) - I_4(x_1', u_2) + I_4(x_1', u_1)], \tag{3.18}$$

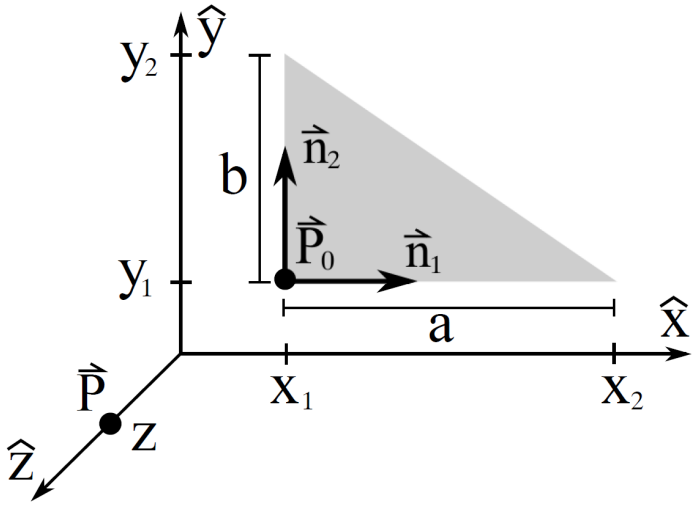


Figure 3.3.: A right triangular subelement defined by the position of the corner point $P_0$, the lengths of the sides $a$ and $b$, and the unit vectors along the sides. The field point is defined as $P$, with local coordinates (0, 0, z). Figure taken from [Cor91].

with $I_3(a,b,u) = \int arcsinh\left(\frac{a+bu}{\sqrt{u^2+1}}\right) \cdot du$ , $I_4(x,u) = \int arcsinh(\frac{x}{\sqrt{u^2+1}}) \cdot du$, $a' = \frac{a}{z}$, $u = \frac{y}{z}$, $u_1 = \frac{y_1}{z}$, $u_2 = \frac{y_2}{z}$ and $x_1' = \frac{x_1}{z}$.

For complex geometries we also need non right triangles. The calculation of the potential of a non right triangle can be found in [FLC+11]. With triangles it should be possible to create every kind of geometry but the computational time using triangles as subelements is much higher than with rectangles. All these subelements and their calculation routines have been implemented into the simulation module *KEMField* by T.J. Corona. Also the electric fields of all subelements are calculated analytically as well.

## 3.4. Solving Techniques for the Charge Densities with the BEM

There are two methods to solve equation (3.6) for $\sigma$. The most well-known is the method of Gaussian elimination. This method is slow and needs a lot of memory, because we have to solve a $N \times N$ huge equation system. N stands for the number of elements. The need of memory depends quadratically of N ($\mathcal{O}(N^2)$).
Another method to solve equation (3.6) is the Robin Hood method. It calculates $\sigma$ with a trick. We randomize the individual charge distribution for each element $i$. If there is a potential imbalance on the surface, charges we moved and swap until the proper potential on the surface is reached [LvA06]. Fiqure 3.4 shows a flow chart of the algorithm. So we get the charge distributions $\sigma$.
Consider a sphere held at a fixed potential $U_0$. We divide this sphere in smaller sub-elements and then randomize the charges on the sub-elements. Once the potential is

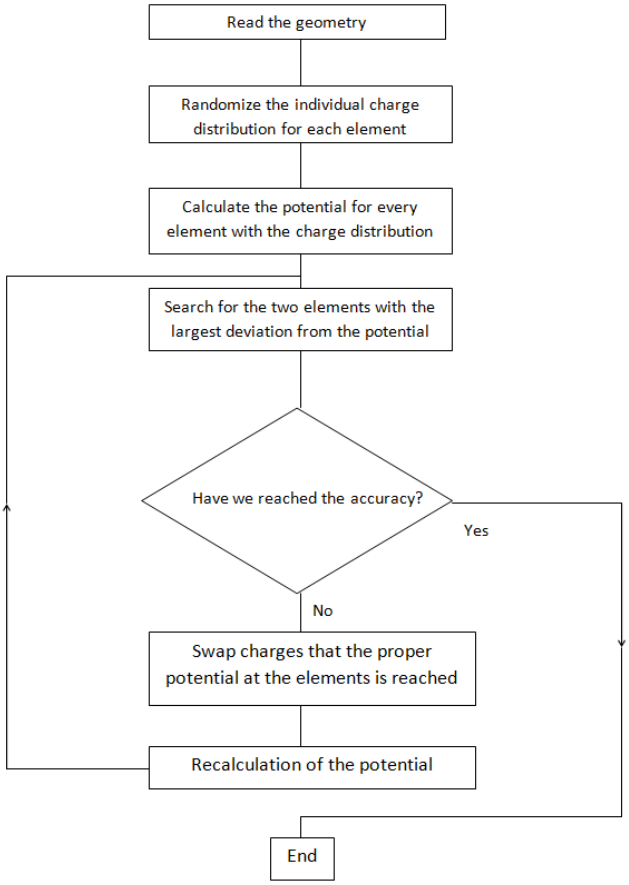


Figure 3.4.: Flow chart of the Robin Hood algorithm.

evaluated at each sub element, the algorithm then performs a search for the two elements that differ most from the equipotential surface ($m$ and $n$). The equipotential condition forces that these two elements have the same potential. So a small amount of charge has to move to these subelements to reach the equipotential surface. This case is given by the following equation.

$$U_0 = U_m + \delta\sigma_m \cdot C_{mm} + \delta\sigma_n \cdot C_{mn} \tag{3.19}$$
$$U_0 = U_n + \delta\sigma_n \cdot C_{nn} + \delta\sigma_m \cdot C_{nm}, \tag{3.20}$$

where $U_0$ is the applied potential, $U_{m,n}$ the current potential of the subelement, $\delta\sigma_{n,m}$ the exchanged charge density of the subelement and $C_{ji}$ the Coulomb-matrix-element. Because the sphere is in contact with a external source, we do not have charge conservation. Solving this equation system gives us the shift of charges between the two electrodes. It is given by the following equation:

$$\delta\sigma'_m = \frac{(U_0 - U_m)C_{nn} - (U_0 - U_n)C_{mn}}{C_{mm}C_{nn} - C_{mn}C_{nm}} \tag{3.21}$$
$$\delta\sigma'_n = \frac{(U_0 - U_n)C_{mm} - (U_0 - U_m)C_{nm}}{C_{mm}C_{nn} - C_{mn}C_{nm}}. \tag{3.22}$$

The potential for every sub-element is subsequently updated to reflect the new charge configuration. The method said to converge once the maximum and minimum values of the potential of all individual electrode is below some user-defined value [FLC+11]:

$$\eta = \frac{U_i - U_0}{U_0}, \tag{3.23}$$

where $U_i$ is the potential of a subelement and $\eta$ is set by the user. Instead of solving $N \times N$ equation system we have now to solve only $N \cdot 2 \times 2$ equation systems.
For the *KEMField* implementation only a small amount of charge has to move to one element to reach the equipotential surface. It showed that the computational time for changing the charge of one element is the best. The potential of a subelement i is given by following formula:

$$U_i = \sigma_i C_{ii} + \sum_{j \neq i} C_{ij}\sigma_j \tag{3.24}$$

This leads us to the shift of the charge of one element to get the Potential $U_0$:

$$\sigma_n = (U_0 - \sum_{j \neq i} C_{ij}\sigma_j)/C_{ii} \tag{3.25}$$

This method is very quick and does not need a large amount of memory. The need of memory depends linearly of the subelements $\mathrm{N}(\mathcal{O}(N))$. Also the iteration number increases logarithmically with the relative potential accuracy. The iteration number depends linearly with the discretization of subelements and the computational time goes quadratically with the number of subelements. [FLC+11]
In the next chapter an intensive study on our simulation package *KEMField* is presented.

# 4. Validation of the Numerical Field Computation Program

In this chapter we investigate our electrostatic simulation tool *KEMField* intensively by computing electrostatic quantities for several test models. Also an analytically solvable electrostatic problem in multiple media will be discussed. The first one is a simple plate capacitor and the second one a more complex wire capacitor. Both capacitors are installed within a box with walls hold on zero potential. The goal is to verify and to test the program *KEMField* against analytical results and commercial software (*COMSOL*). Furthermore the computation time of *KEMField* is tested on several computing platforms.

## 4.1. Geometry of the investigated Problems

The geometrical center of the box is located at the position $x = y = z = 0$. All other position vectors are given relatively to that point. We test these geometries in vacuum and within two dielectric media. For the relative permittivity we take the values for liquid ($\epsilon_l \approx 2$) and gaseous ($\epsilon_g \approx 1$) xenon. Every side of the box has a height of 40 $cm$. For the test with dielectrics we fill the the bottom half of the box with liquid xenon and the upper half with gaseous xenon. The box and the liquid gaseous boundary are discretized with rectangle-primitives, which have been discussed in subsection 3.3.2. The discretization scale for the box and the boundary has been chosen high enough to not lose some accuracy.
The first geometry inside the box is a simple plate capacitor. The plate capacitor is made of two square plates. Both square plates have a length and a width of 0.276 m without a thickness. The center of the first square plate is installed at the position $(0, 0, -0.01)$ and the center of the second square plate is installed at the position $(0, 0, 0.01)$. Hence we constructed a plate capacitor with a distance of $d = 0.02$ m. The potential of the upper plate (cathode) is $U_{\text{cath}} = 1500$ V and the potential of the bottom plate (anode) is $U_{\text{an}} = -500$ V. The plates are discretized by rectangular primitives.
The type of capacitor consists of 52 wires. Each wire has a diameter of 0.001 m and a length of 0.276 m. There are two layers (cathode and anode) and each layer consists of 26 wires with a gap of 0.01 m in x-direction. The distance between the upper layer and the bottom layer is 0.19 m. The space between the last wires and the zero potential box is 0.062 m. The length of the layer in y-direction is 0.276 m. The potential of the upper wires (anode) is 1500 V and the potential of the bottom wires (cathode) is $-500$ V. The wires are discretized with wire segments, which have been described in subsection 3.3.1.

Both geometries and the zero potential box can be found in the appendix A.
The geometries were discretized with a special for this test developed C++ program, which uses *KEMField* for the calculation of the charge densities and the electric fields and electric potentials. The region of interest can be chosen in this program to get the physical output in ROOT [BR97]. The program is available in the *Kasper* package, called "TestDielectrics.cc" and the code will be not discussed in context of this thesis.

## 4.2. Results of the Test Computations

For all simulations we calculate the electric field component $E_z$, the potential $\phi$ and the electric displacement component $D_z$ along the z-axis, at the position $y = x = 0$. The discussion focuses on the region from $z = -0.01$ to $z = 0.01$. The simulation of the charge densities were performed until the rectangles achieve a relative accuracy of $10^{-8}$, as described in subsection 3.4.

### 4.2.1. Analytical Results

For an infinitely large plate capacitor without a dielectric medium we expect following result for the electric field according to the well known analytical formula:

$$E = \frac{U}{d}. \tag{4.1}$$

The electric potential $\phi$ is given by equation:

$$\phi = \frac{U}{d} \cdot z + c_0. \tag{4.2}$$

In our case the distance between the plates is 0.2 m and the voltage -2000 V. We obtain an electric field of $E = -100000$ V/m.

To obtain an analytical formula for a two phase plate capacitor we have to consider additional boundary conditions. The parallel component of the electric field $\vec{E}_{||}$ has to be continuous through the interface. This relation comes from the conservative property of the field over a dielectric interface ($\oint \vec{E} \cdot d\vec{L} = 0$).

$$\vec{E}_{1,||} = \vec{E}_{2,||} \tag{4.3}$$

In our case, $\vec{E}_{1,||}$ is the parallel component of the electric field in liquid xenon and $\vec{E}_{2,||}$ is the parallel component of the electric field in gaseous xenon. The vertical component of the electric field $\vec{E}_{\perp}$ isn't continuous through the interface. The relation can be calculated with the Gauss' law over a closed surface centered around the interface:

$$E_{1,\perp} \cdot \epsilon_1 = E_{2,\perp} \cdot \epsilon_2, \tag{4.4}$$

where $\epsilon_1$ and $\epsilon_2$ are the permitivities of liquid and gaseous xenon. In a plate capacitor with infinitely large plates we only get an electric field in z-direction, so our total sum of the voltage is given by following equation:

$$U = E_{1,z} \cdot d_1 + E_{2,z} \cdot d_2. \tag{4.5}$$

Solving equations (4.4) and (4.5) leads to following expressions of the the electric field in liquid and gaseous xenon.

$$E_{1,z} = \frac{U}{3 \cdot d_2} \tag{4.6}$$

$$E_{2,z} = E_{1,z} \cdot \frac{\epsilon_1}{\epsilon_2} \tag{4.7}$$

By plugging in the corresponding values for $U = -2000$ V, $d_2 = 0.01$ m and the corresponding dielectric constants, we expect an electric field of $E_z^1 = -6666.\overline{6}$ V/m and $E_z^2 = -13333.\overline{3}$ V/m.
These calculations are valid for an infinitely large plate capacitor. Hence we expect differences between the analytical solution and the simulated values especially at the edges of the plate capacitor.
For complex wire capacitors it is not possible to compute an analytical solution.

### 4.2.2. Results of a numerically computed Plate Capacitor

Figure 4.1 shows a plot of the calculated electric field in vacuum and in gaseous/liquid xenon, calculated with *KEMField*. The corresponding electric potentials can be found in the appendix B. We see that the electric field of a vacuum plate capacitor in vacuum is constant. For a dual phase plate capacitor the electric field is also constant, but there is a jump in the electric field $E_z$ at the interface. The electric field is different for the gaseous phase and the liquid phase, because the value of the electric field depends on the electric permittivity. This is an expected result and has been calculated analytical in 4.2.1 .
We compared the result of *KEMField* with the analytical solution in 4.2.1 and *COMSOL Multiphysics*, a commercial simulation software. This software is based on the finite element method (FEM) described in chapter 3. We build up the same geometry in *COMSOL* and calculated the electric field $E_z$ and the potential $\phi$ at the same points. For the implementation of the geometry into *COMSOL* we need a closed computational domain,

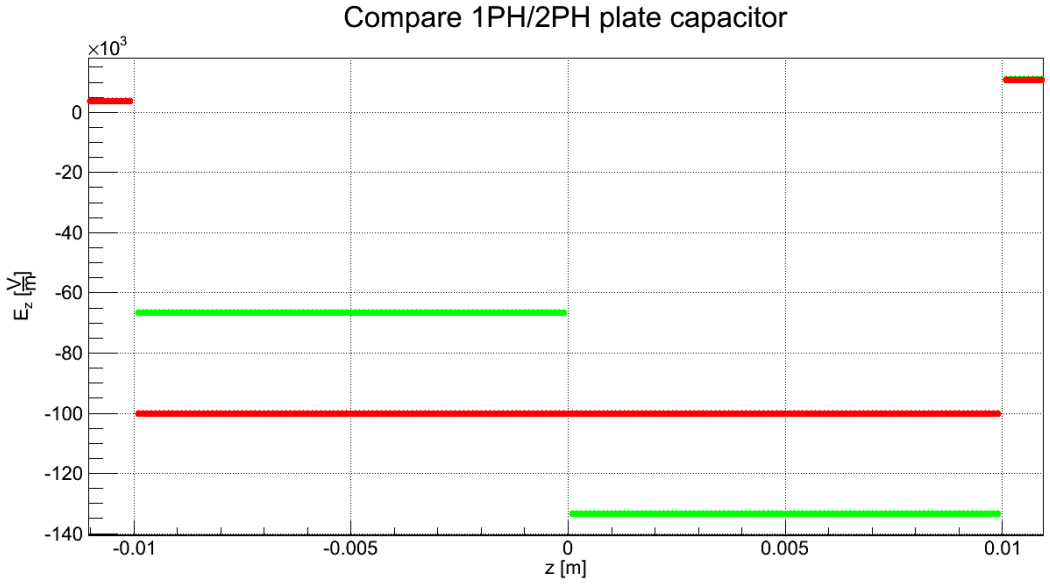


Figure 4.1.: The electric field in vacuum and in liquid/gaseous xenon. The red points indicate computed values in vacuum, and the green points in liquid/gaseous xenon.

because of the FEM. Therefore we took two boxes, set the dielectric properties for every box and installed the plate capacitor over the interface. For the simulation we discretized the domain with tetrahedrals. The meshing is performed by *COMSOL* and limited by the user.
Figure 4.2 shows the difference of the electric field $E_z$ between *COMSOL* and our field programm *KEMField* in vacuum and with dielectrics. Also the relative error for *COMSOL* and *KEMField* has been calculated. The calculated relative error for a vaccum plate capacitor and a dual phase plate capacitor can be found in the appendix B. The relative error $f$ is defined as follows:

$$f = \frac{x_s - x_a}{x_a}. \tag{4.8}$$

$x_s$ is the value from the simulation and $x_a$ is the value from the analytical solution. To get the percentage error we have only to multiply the last equation by 100%.

The absolute difference between the electric field and the potential values of *COMSOL* and*KEMField* is for this simple geometry not very huge, but the difference isn't constant and varies a lot. The variations occur for a vacuum plate capacitor and a dual phase capacitor. At some points the field values are almost the same and at some points it differs very strongly. This is an indication of a bad discretization with *COMSOL*, because with *COMSOL* we have to discretize the whole computational domain and weren't able to control the mesh at every position precisely. At all we see that for this simple geometry *KEMField* and *COMSOL* compute almost the same values.
Also the calculated relative error $f$ for $E_z$ is very small, but *KEMField* gives us a better constant error. The relative error from *COMSOL* varies a lot. The relative error in the region of the plates is slightly higher than at the center, because of our chosen discretization and the zero potential box. But the relative error of *COMSOL* is higher than the relative error of *KEMField*. A possible explanation for this behaviour is that we didn't discretize with *COMSOL* very fine. *COMSOL* uses FEM and has to discretize the whole volume. We often got out of memory with the caluclation with *COMSOL* and decided to avoid too

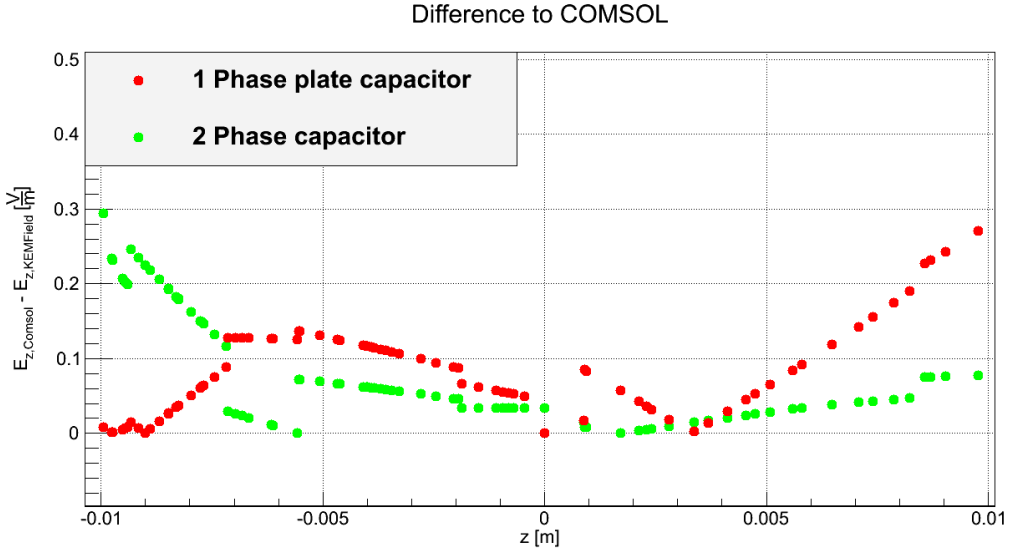


Figure 4.2.: The difference of the electric field $E_z$ between *COMSOL* and *KEMField* for the plate capacitor in vacuum (red points) and or a dual phase plate capacitor (green points). The points indicate the absolute value of the difference between the two field solvers.

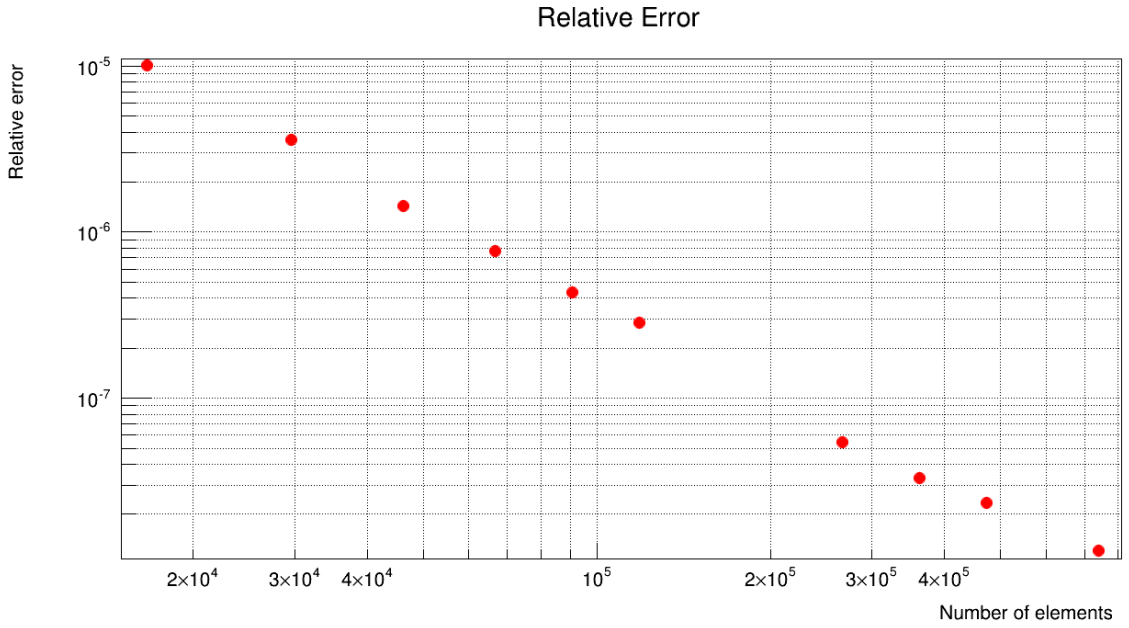


Figure 4.3.: The dependency of the relative error of the number of elements. The point $(0, 0, 0.0004)$ of the plate capacitor were investigated.

small elements, hence too high discretization parameters. N.b.: If we use small elements we have to fill our whole volume with these elements and we need a huge amount of memory. For all calculations with *KEMField* we discretized our geometry into 118800 primitive rectangles to have a short calculation time and a small relative error. Figure 4.3 shows the dependence of the relative error on the number of elements. We took as example the point $(0, 0, 0.0004)$ and calculated the relative error of the potential of a vacuum plate capacitor with different discretizations. We see in Figure 4.3 that we are able to minimize the relative error $f$ with *KEMField*, if we chose a high discretization. We have to find a compromise between the number of elements and the accuracy. If we increase the discretization, the calculation time increases as well by

$$t \approx n^2, \tag{4.9}$$

where $t$ denotes the calculation time and $n$ is the number of elements. With *COMSOL* we would also be able to minimize the relative error but due to the limited memory have not been able to study the discretization quality of *COMSOL*.

### 4.2.3. Results of a numerically computed Wire Capacitor

For the discretization of this geometry we used rectangular primitives and wire segments. Figure 4.4 shows the electric field. The electric potential can be found in the appendix B. We can see that also with the wire capacitor the electric field has a jump at the gaseous-liquid interface, because of the different dielectrics. For the wire capacitor we didn't obtain a constant electric field, inside of the capacitor. We compared this result with *COMSOL*. We build up this wire capacitor in *COMSOL* and calculated the potential and the electric field $E_z$ and the electric potential $\phi$ along the z-axis. The difference between *COMSOL* and *KEMField* of a wire capacitor can be found in the appendix B. We see in this case that the difference between *COMSOL* and *KEMField* is significant. The difference occurs in vacuum and in dual phase xenon. *COMSOL* delivers everywhere a higher electric field than *KEMField*. The difference of the dual phase wire capacitor is higher than for the vacuum

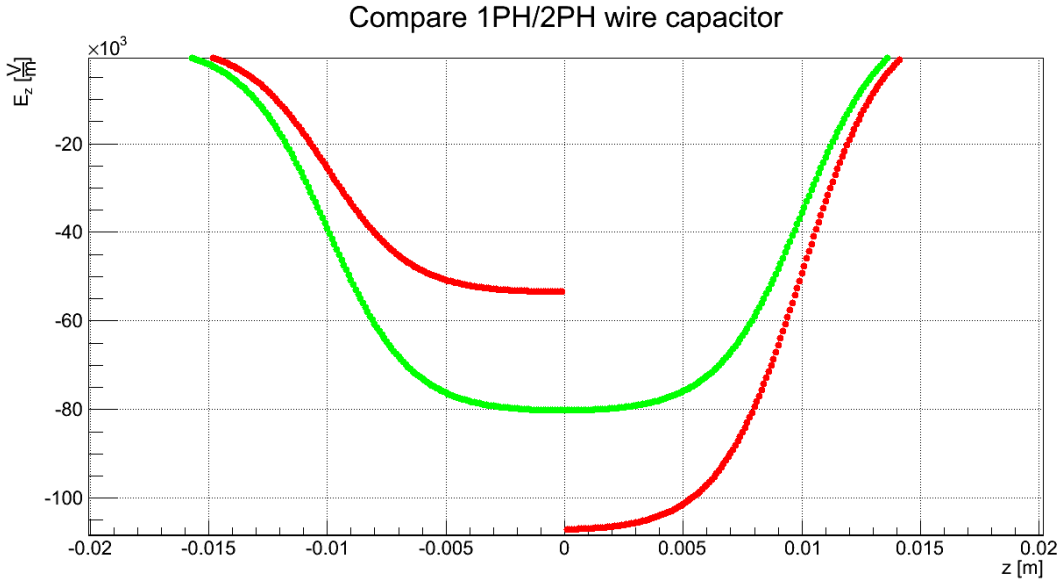


Figure 4.4.: The electric field in vacuum and in liquid/gaseous xenon. The red points are in vacuum and the green points are in liquid/gaseous xenon.

wire capacitor. A reason could be the different discretization of the boxes in *COMSOL*. In *KEMField* we discretize everything very well, we have ensured that the discretized wire elements are neither too big, too small.
There is a limit established by Dr. Ferenc Glück for the element size of the wires (F. Glück 2013, pers. comm.). The discretized element $e$ of a wire is not allowed to be bigger than the space between the wires $s$ and smaller than the wire diameter $d$.

$$d \leq e \leq s. \tag{4.10}$$

By respecting this rule, we can assume a constant charge density on one wire element as a very good approximation. With *COMSOL* we will get out of memory if we discretize the geometry very fine. So the difference between *COMSOL* and *KEMField* should come from an insufficient discretization of *COMSOL*. To ensure that fact we made a step back: We calculated the electric field of two parallel wires with *COMSOL* and *KEMField*. For this very simple geometry we know a analytical solution and for such a small geometry we can discretize with *COMSOL* a way finer.

### 4.2.4. Computation of Electrostatic Fields of two parallel Wires

We installed one wire at a position $a$ and one wire at the position $-a$. The wires had a diameter $d$. The analytical solution for the electric field $E$ of an infinitely wire can be found using the Gauss's law in cylindrical coordinates:

$$2\pi r E = \frac{\lambda}{\epsilon_0}. \tag{4.11}$$

Two infinite wires are located in the x-y plane, parallel to the x-axis. One carries a charge density of $+\lambda$ and is located at the location $y = +a$ while the other carries a charge density of $-\lambda$ and is located at the point $y = -a$. The electric potential of one wire, we obtain by using the formula [Gri07]:

$$V = -\int \vec{E} d\vec{l}. \tag{4.12}$$

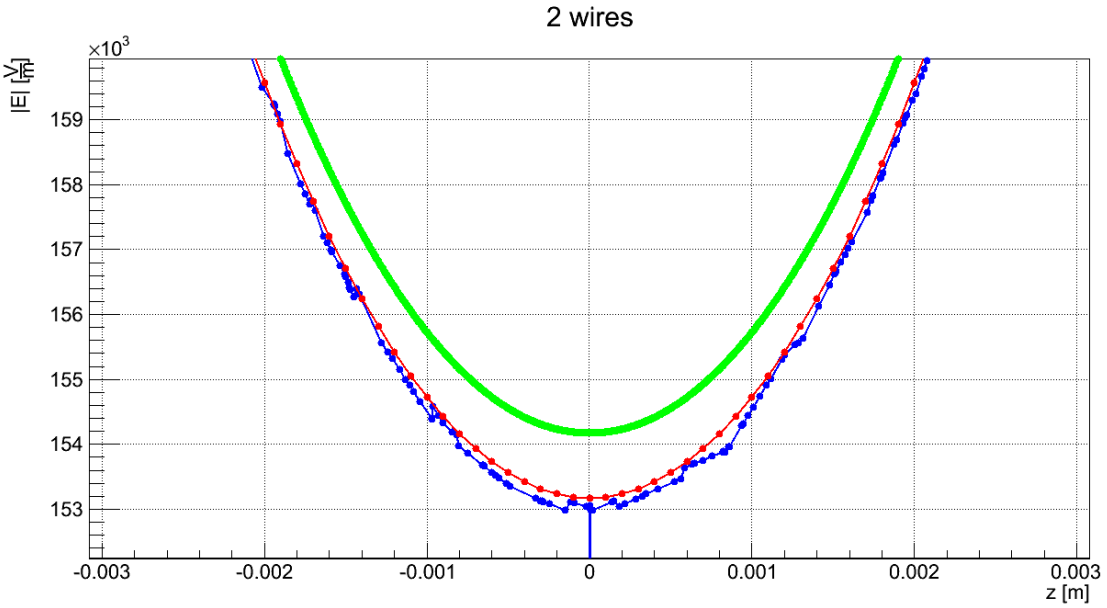


Figure 4.5.: The electric field for two parallel wires. The *COMSOL* discretization is fine. The red points indicate the analytical solution. The green points are the solution of *KEMField* and the blue points are the solution of *COMSOL*.

The potentials from the two wires we summed according to the superposition principle. So the total potential and electric field is [Gri07]:

$$V = \frac{\lambda}{2\pi\epsilon_0} \ln \frac{\sqrt{(y+a)^2+z^2}}{\sqrt{(y-a)^2+z^2}} \tag{4.13}$$

$$E = \frac{\lambda}{2\pi\epsilon_0} \left( \frac{1}{\sqrt{(y-a)^2+z^2}} - \frac{1}{\sqrt{(y+a)^2+z^2}} \right) \tag{4.14}$$

We build up this geometry in *KEMField* and *COMSOL*, with $a = 0.01$m and $d = 0.001$m For *COMSOL* we needed a zero potential box to close the domain of computation, because of the FEM. We made the wires very long to be able to use equation 4.13. Figure 4.5 shows the electric field between the wires at $x = y = 0$. We are now able to discretize this simple geometry finer in *COMSOL* without to getting out of memory. We saw that for a very coarse discretization the *COMSOL* solution deviates very strongly from the analytical solution. For a finer discretization we see that the *COMSOL* solution converges to the analytical solution. The coarse discretization result can be found in the appendix B. *COMSOL* failed to calculate the electric field at $z = 0$ m for not understood reasons. But also for this geometry we were limited in the discretization, because we got out of memory. That is the reason for the small variation of the *COMSOL* results.
In this geometry we found something interesting about *KEMField*. The *KEMField* solution differs from the analytical solution, because the wires are assumed as line segments and the field points are too close to the wire. The assumption doesn't hold longer valid. This aspect and the bad discretization of the wire capacitor with *COMSOL* is a possible solution for the difference of the *COMSOL* results and the *KEMField* results. This is an important result for analysing the electrostatic fields. If we calculate the electric fields in the region of wires, we have to think about the correctness of these results. In the future an other field computation routine for wires should be developed to reduce this particular error.

A solution is to discretize the whole wire with triangles or rectangles so that we get a cylinder. In the next section we analyse the fields and potentials of *KEMField* for another geometry.

### 4.2.5. Computation of Electrostatic Fields of a Wire Grid

We modified our wire capacitor geometry in 4.1 so that we are able to compare it with an analytical solution. Our zero potential box has now following size measure. A height of 0.08 m, weight of 1 m and a depth of 1 m. The diameter of the wire is reduced from 0.001 m to 0.00001 m. The pitch between the wires is reduced from 0.01 m to 0.001 m. The layer distance is increased from 0.02 m to 0.04 m. The total amount of wires per layer is increased from 26 to 40. The potential of both layers is now 100 V. Figure 4.6 shows the new geometry. With this geometry we are able to use equation (4.15) (Eq. 12 in [Glu07]) to calculate the potential at $(0, y, 0)$:

$$\phi = U_g + \frac{U_f - U_g}{1 + \frac{2 \cdot l \cdot \pi}{s \cdot \ln\left(\frac{s}{\pi \cdot d}\right)}}. \tag{4.15}$$

$U_f$ is the potential of the box, $U_g$ is the potential of the wires, $l$ is the distance between wire and box, $s$ is the space between the wires and $d$ is the diameter of the wires. So we should get in such a geometry a potential at $(0, y, 0)$ of 68.5575 V.
To obtain the electric field we make some approximations. With these approximations we won't find the true value of the electric field but we will find the scale of the electric field. In a short distance away from the bottom plate the electric field is nearly constant in y-direction. The electric field is given by:

$$E_p = \frac{U}{l}. \tag{4.16}$$

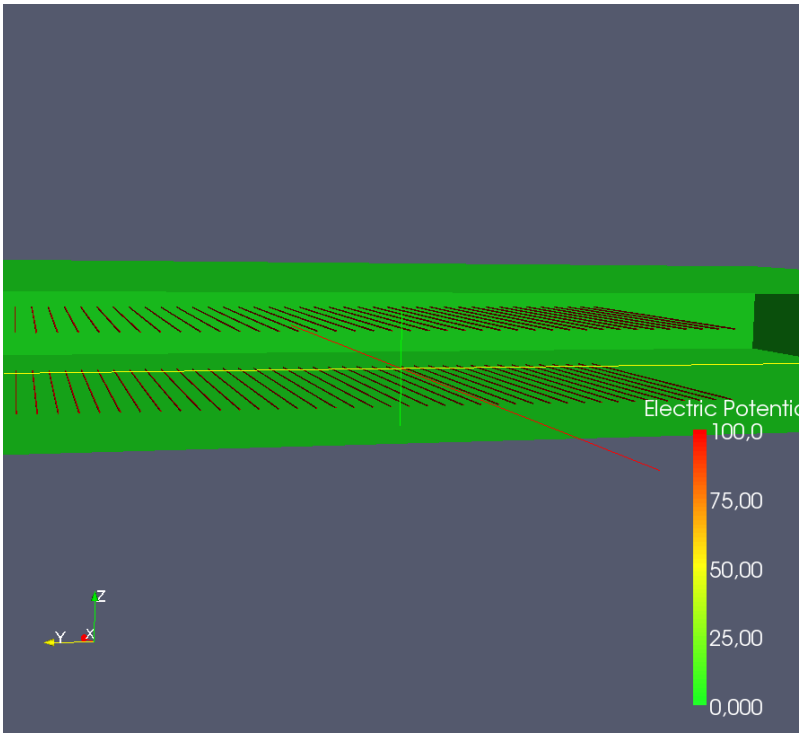


Figure 4.6.: The 3D model of the new geometry. The colors represent the value of the electric potential.

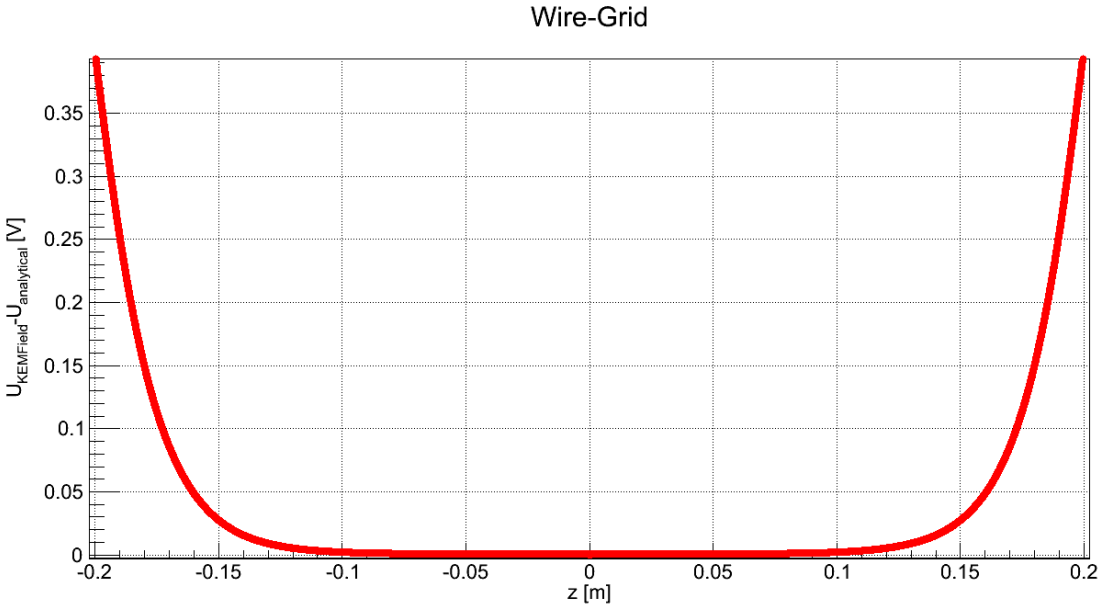


Figure 4.7.: The red points are the absolute value of the difference between *KEMField* and the analytical solution for the electrical potential.

We can compute the electric field from the electric flux by

$$E = \frac{\phi}{A}. \tag{4.17}$$

The electric flux $\phi$ close to the plate and around the wire should be the same, with the assumption that every electric field line from the plate in a size $s$, ends in the wire with the diameter $d$. So the electric field close to the wire should be given by equation (4.18):

$$E_w = \frac{U}{l} \cdot \frac{s}{\pi \cdot d}. \tag{4.18}$$

By plugging in the corresponding values for s, $\pi$, d , U and l we expect an electric field at the wire of $E_w = 1.59 \cdot 10^5$ V/m.
We build up this geometry in *KEMField*. With *COMSOL* it wasn't possible because the wires are now to thin.
In figure 4.7 we see that *KEMField* delivers a very good result for this geometry. The analytical solution for the electric potential and the solution from *KEMField* match very well in the center region. At the edge of the geometry the analytical solution and *KEMField* don't match, since the analytical solution assumes an infinitely large wire grid.
The electric field plot can be found in the appendix B. At the wires the electric field is around $E_z \approx 1.50 \cdot 10^6$ V/m. This matches very good with our expectation. The reason for the difference is that we assumed a too high electric field in front of the plate. $E = \frac{U}{l}$ gives us not exactly the correct value in front of the plate. But this technique is very good to estimate the electric field.

## 4.3. Analyze and Optimization of the numerical Computation Programs

The calculation time depends on the number of discretized elements and on the method to solve equation (3.6). The most common technique to solve this equation is the Gaussian

elimination. The matrix $W_{ij}$ grows with the number of discretized elements and the need of memory increases with number of discretized elements squared $\mathcal{O}(n^2)$. The computer runs fast out of memory and the linear equation system (3.6) cannot be solved for large geometries.
Taking advantage of the iterative Robin Hood method, the amount of used memory increases linearly with the number of elements and allows to compute charge densities for large scale geometries containing small scale structures.

### 4.3.1. Comparison of different used Technologies for the Computations

To demonstrate the power of parallelized computing platforms (n.b. graphic processing units can handle several hundreds jobs in parallel), we calculated the plate capacitor for different discretization parameter. First we calculated the charge distribution on only one GPU using the computer a NVidia graphic cards. Afterwards we implemented MPI [For93] into our code to be able to use multiple GPUs in parallel. For this purpose we had to switch to the AMD graphic cards due to technical reasons. Figure 4.8 shows the dependency of the charge distribution calculation time in relation to the number of discretized elements. Solving equation (3.6) with a direct solver is very slow and since the available computer memory is limited, it is not recommendable to use very fine discretizations in combination with this type of solver. The calculation time on a GPU with the Robin Hood method is much better than the direct solver on a CPU. With the Robin Hood method we are able to use very accurate discretizations without getting out of memory. The calculation time on a GPU with the Robin Hood method is very amazing, it is roughly of one order of magnitude lower than on a CPU. For geometry discretizations containing over 362600 elements it is useful to parallelize multiple GPUs with MPI.
Table 4.1 comprises some selected values of 4.1. The calculation time for 118400 elements

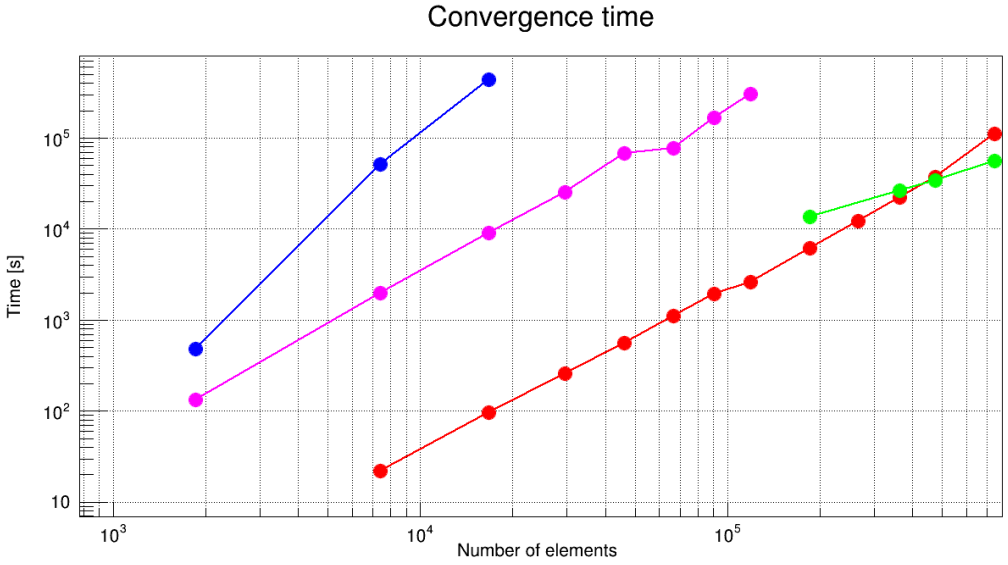


Figure 4.8.: The calculation time for different CPU- and GPU-platforms. The blue points represent the calculation time on a CPU using a direct solver. The purple points are the calculation time on a CPU using the iterative Robin Hood method. The red points indicate the calculation time on a single GPU using the Robin Hood method and the green points use four graphic units of the AMD-GPU-cluster in parallel, which is realized by an implementation of MPI within KEMField.

Table 4.1.: Excerpt of values of figure 4.8

| elements | CPU-DS | CPU-RH | GPU-RH | MPI-RH |
|---|---|---|---|---|
| 16650 | 434073 s | 9107 s | 96 s | x |
| 118400 | x | 303853 s | 2629 s | x |
| 362600 | x | x | 22276 s | 26202 s |
| 740000 | x | x | 110793 s | 55857 s |

with the Robin Hood method on a GPU is around 43 minutes. On a CPU the calculation time for the same problem is around 3.5 days!
Because of this fact, firstly we used for our simulations a single GPU (NVidia), but after increasing the number of discretized elements over the limit of 362600, it is worth while parallelizing multiple GPUs. The question is why single GPUs deliver faster results for smaller discretization than multiple GPUs?
The reason is the following: The GPUs have to communicate to each other and have to access the memory. If more GPUs are active, the memory of the computer has to be accessed more frequently. For small discretizations more time is spent on the transfer of data between memory and the GPUs, it would be better to use only one GPU and avoid this data transfer. In case of computing more elements, the advantage of splitting the job and using multiple GPUs dominates.
The computational time dependence also on the type of used sub-elements (triangle, rectangles and wires) and on the boundary condition (Neumann or Dirichlet). If our surface belongs to a Neumann condition then we have to solve more complex integrals which increases our computational time.
The calculation time for the charge densities depends also on the different platforms. For the field calcuation on a CPU we used the CPU-Cluster *Tesla* of the KIT Institute of Nuclear Physics (IKP). It is a cluster with 776 nodes controlled by a Sun Grid Engine. Every CPU is a Intel Xenon 5550 2.67 GHz. For one simulation up to 8 GB of memory can be used.
At the Karlsruhe Institute of Technology we have access to two GPU-Clusters. Both computers are located and administrated at the KIT Institute for Data Processing and Electronics (IPE) and have been used for calculations on GPUs. The two clusters have following technical specifications:

- 2x Intel Xeon E5-2640 CPUs (2.5 GHz and 12 Threads each), 24 GB RAM, 2x Tesla XM and 4 NVidia GTX TITAN.
- 2x Intel Xeon E5540 CPUs (2.53 GHz and 8 Threads each), 96 GB RAM, 4x NVidia GTX 590 Dual-Core GPUs and 1x NVidia GTX 680.

# 5. Realization of Electrostatic Field Computations for the XENON1T Detector

For the next generation dual phase dark matter detectors, highly efficient techniques and fast simulation software is needed, since detailed electrostatic simulations of large detector geometries need a large amount of computing power.
As we have seen in the previous chapter, only the boundary element method (BEM) is able to handle large scale problems efficiently, resulting in a minimal need of memory and computation time.
For next generation dual phase dark matter detectors, like DARWIN and XENON1T, the simulation package *Kasper* from the KATRIN experiment has been successfully adapted. In order to use this software for dual phase detectors, new modules have been developed. With this module it is now possible to build up complex dual phase geometries, using the boundary element method as field solver and perform so electrostatic field simulations and particle tracking.
For the test of the new submodules, the XENON1T geometry has been implemented and simulated and will be discussed in detail. The following chapter is not a line per line program documentation but a basic description of the classes and explains how they work. The source code is fully available from the KATRIN GIT repository.

## 5.1. Presentation of the newly developed Computer Programs

The DARWIN module consists of two submodules, which depend on core modules of the *Kasper* package.
One submodule is DGeoBag (DARWIN Geometry Bag). For a simulation, the geometry has to be discretized by using well defined basic shapes. DGeoBag is the container for these shapes and also responsible for the discretization of every shape. It has in principle the same structure as KGeoBag (KATRIN Geometry Bag). Several new shapes and their discretization have been created and added to DGeoBag. Also some test applications are implemented into DGeoBag in order to investigate the quality of the discretization of the shapes. With these new implemented shapes it is possible to build up an arbitrary TPC geometry with dielectrics.
The other submodule is the existing KEMField (KATRIN electro magnetic field). It consists of two new programs. The first program builds up the geometry with the shapes

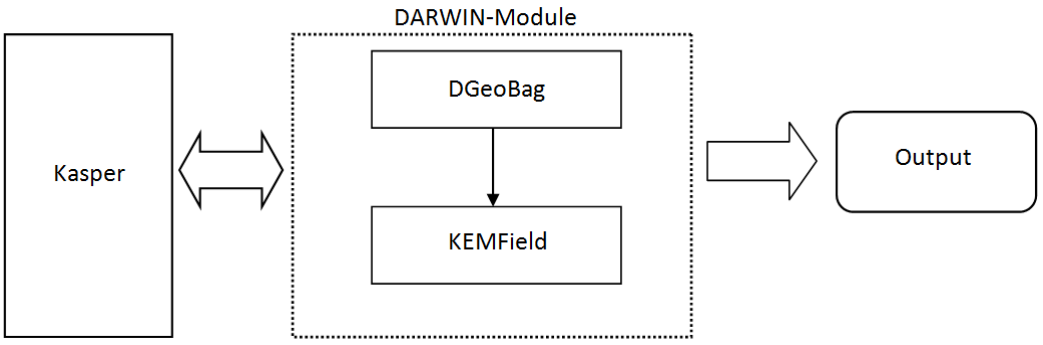


Figure 5.1.: The DARWIN module consists of two independent sub-modules (*DGeoBag* and *KEMField*). These sub-modules uses some other modules of the *Kasper* package to perform the simulations.

of DGeoBag and calculates the charge densities of the subelements with *KEMField*. The second program calculates the electric field and electric potential in the region of interest with pre-computed charge densities.
Figure 5.1 shows the implementation of the DARWIN module into the Kasper framework. The next subsections describe the implementation of the shapes into *DGeoBag* and the implementation of the field calculation programs into *KEMField*.

### 5.1.1. DGeoBag

For every new shape, which are implemented into the submodule *DGeoBag*, two new classes are needed. The first class holds all important parameters and constructs the shape. Some important parameters are e.g the discretization parameter, size and voltage of the shape. The second class discretizes the shape with the primitives described in section 3.3. The primitives are triangles, rectangles and wires. Figure 5.2 shows a schematic of the *DGeoBag* sub-module.
For the class names of the shapes and their discretizers prefixes 'DG' (DARWIN Geometry) or 'XG' (XENON Geometry) for a better distinction is chosen. For a basic shape like a disc, 'KG' (KATRIN Geometry) is used as the prefix.
For the XENON1T geometry eight new shapes and their discretizers have been implemented into *DGeoBag*. The following list shows the parts which have been developed especially for the XENON1T geometry.

- **Vessel** Creates the vessel of the XENON1T geometry.

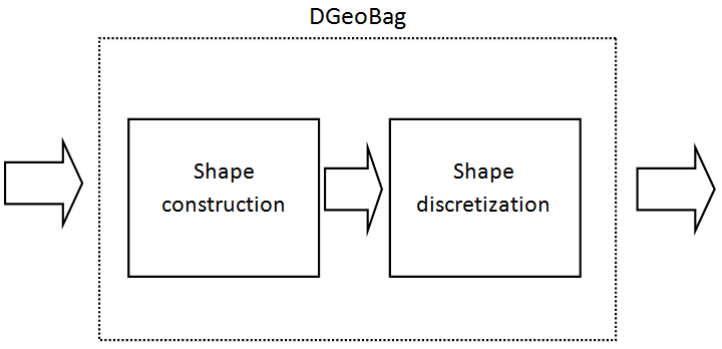


Figure 5.2.: The two classes, which are needed to implement one shape into the *DGeoBag* sub-module. The name of the class describes the shape.

- **RingElectrode** Creates one field shaping ring.
- **CAD** Imports CAD drawings into the geometry.
- **WireMesh** Creates a wire mesh, which is needed e.g. for the cathode.
- **PMT** Creates a PMT array.
- **Cathode-holder** Holder for the cathode.
- **Anode-holder** Holder for the anode.
- **Gate-holder** Holder for the Gate.

In context of this work, discretization routines of other standard shapes have been completed to be able to use them for dual phase detector geometries as well as for the KATRIN geometry. The following list shows the completed standard shapes.

- **Disk** Creates a disk.
- **Annulus** Creates a annulus.
- **Cone** Creates a cone.
- **Cut-Cone** Creates a complete cute-cone.
- **Cut-Cone-shell** Creates the shell of a cut-cone.
- **Torus** Creates a torus.

The discretization principle of the CAD imported elements, disks, annulus, wire meshes and cylinder shapes will be discussed more in detail in section 5.2, because these shapes use all different kinds of primitives. Their implementation code can be found in the appendix C.
The implementation of the other new very complex shapes will not be discussed, because their discretization technique is similar. The geometries of the complex XENON1T shapes are shown in the appendix E but not their implementation. This code can be found with the whole DARWIN module on the KATRIN GIT repository.

### 5.1.2. KEMField

To calculate the charge densities and to analyse the geometry, two new programs have been developed and implemented into the DARWIN module. The submodule uses *KEMField* for the calculation of the charge densities, electric fields and electric potentials.
The first program builds up the geometry and computes the charge densities with the Robin Hood algorithm. The geometry will be build up with the discretized shapes from *DGeoBag*. Therefore an object of the shape has to be created. The output of this program is an ASCII or a binary file, which contains the calculated charge densities and the geometrical positions of the subelements. This calculation can be performed either on a CPU or on a GPU. Also MPI has been implemented into the code to be able to use multiple GPUs or multiple CPUs in parallel.
The second program calculates the electric field and electric potential in the region of interest. The region of interests of a TPC can be found in [BH12] and has been insert into the code. As input, the ASCII file or the binary file of the previous simulation is needed. The output is a ROOT file, which contains plots of the computed electric fields and potentials. Also a real time plotter has been developed, which gives the user the opportunity to control the calculated field points. This calculation can also be performed on CPUs or GPUs but not in parallel. The programs are also available on the KATRIN GIT repository.

## 5.2. Geometrical Description of the Electrostatic Problem

This section describes the discretization principle of the shapes with wires, triangles and rectangles. Therefore the discretization of the wire mesh, the cylinder and disk/annulus is discussed more in detail. Another very powerful shape is the CAD import shape. With this shape it is possible to import CAD drawings or meshes from an external software. This is an easy way to build up geometries with existing CAD drawings. The usage of this shape and their implementation will also be discussed.

### 5.2.1. CAD Import into KEMField

The implemented CAD import shape uses STL files. STL is known as Standard Tessellation Language. STL files describe only the surface of the CAD drawing. A STL file describes a raw unstructured triangulated surface by the unit normal and vertices of the triangles using a three-dimensional Cartesian coordinate system. The STL file consists of a huge number of triangles. The triangle is described by the unit normal vector ($n_i$, $n_j$ and $n_k$) pointing outwards from the triangle and by its three points ($\vec{v_1}$, $\vec{v_2}$ and $\vec{v_3}$). The CAD import shape opens and reads in these STL files. The program looks for the vertices and the normal unit vectors of the triangle inside the STL file and creates a triangle primitive. The program also checks if the normal unit vector has been calculated correctly. The triangle primitive is created in DGeoBag over the following command:

```
1 KGMeshTriangle* triangle = new KGMeshTriangle(t1, t2, t3);
2 AddElement(triangle);
```

Listing 5.1: The creation of an triangle primitive in DGeoBag.

$t1$, $t2$ and $t3$ are the corner points of the triangle. The normal unit vector is determined over $v1 \times v2$.
The big advantage of using STL files is that we don't have to take care about discretization parameter, because a STL file contains already the discretized surface information. CAD softwares like *CATIA* or *SOLIDWORK* are able to safe their CAD drawings into a STL file. Figure 5.3 shows a three-dimensional CAD drawing of the DARWIN logo before and after import into the DARWIN module. For the visualization we used VTK [ea13]. The Visualization Toolkit (VTK) is an open-source, freely available software system for 3D computer graphics. Using the STL mesh from software like CATIA or SOLIDWORK have a disadvantage. The mesh is quite coarse and cannot be controlled precisely, but a good discretization is needed for some imported CAD drawings. Hence for the XENON1T geometry didn't import the STL files directly from the CAD software. We used *NetGen* [SGG03] where could precisely change the STL mesh of our CAD drawings. *NetGen*


(a) CAD-DARWIN logo in CATIA (b) CAD-DARWIN logo in the DARWIN module

Figure 5.3.: (a) The CAD DARWIN logo visualized with CATIA. (b) The imported discretized DARWIN logo visualized with VTK.

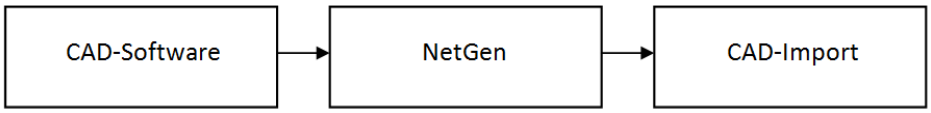


Figure 5.4.: The mesh for the CAD drawing will be created with *NetGen*. The output from *NetGen* can be imported into the DARWIN module.

is an open source software, which uses the Delaunay triangulation. With the Delaunay triangulation can create for a set of points $P$ a polygon mesh. The output of *NetGen* is a qualitatively good mesh in STL format. This STL file can import over the CAD import shape into our DARWIN module. The source code of the Delaunay triangulation could also be implemented directly in the *Kasper* package in the future. Figure 5.4 shows the schematic of the CAD import for XENON1T.
In principle, the whole XENON1T geometry could be imported via CAD drawings, but this is not recommended, because of the limited precision in setting the mesh of a CAD drawings and the huge need of subelements of a detailed CAD drawing. Using a mix between standard shapes, complex shapes and CAD imports is the best solution. CAD imports are good for shapes, which would take a lot of time to implement, e.g for an electrode with a lot of holes and a non-smooth surface.

### 5.2.2. Disk and Annulus Discretizer

This section gives an introduction into the common discretization technique of complex shapes. The discretization of a disc and an annulus is quiet similar, therefore both will be shown. For the discretization triangular subelements are used. It is also possible to discretize these shapes with rectangles, but this would need a lot of more elements.
For the disc and annulus discretization we create first a single trapezoid, which consists of two triangles. The complete disc and annulus is then created with these trapezoids. Figure 5.5 shows a trapezoid divided into two triangles. For the discretization of the disc, first the radius $R$ will be discretized into $N$ elements with a discretization power of $P$. Then the disc will be discretized into $M$ arcs. Every arc will be build up with $N-1$ trapezoids and one triangle at the center. The total amount of triangular subelements is given by $(2N-1)\cdot M$.
For the annulus we only have to discretize the radius from $R_1$ to $R_2$ and leave the first triangle. Figure 5.6 shows the discretized disc and annulus visualized with VTK. The user has the opportunity to control the meshing of these two shapes. It can be chosen the

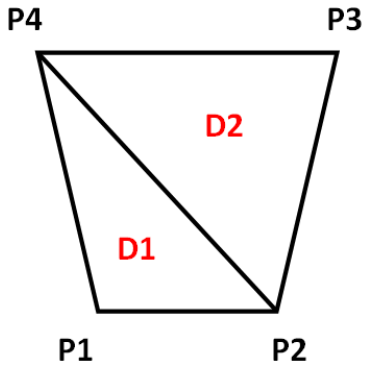


Figure 5.5.: The trapezoid gets divided into two triangles (D1 and D2). The first triangle D1 is described by the points P1, P2 and P4. The second triangle D2 is described by the points P2, P3 and P4.

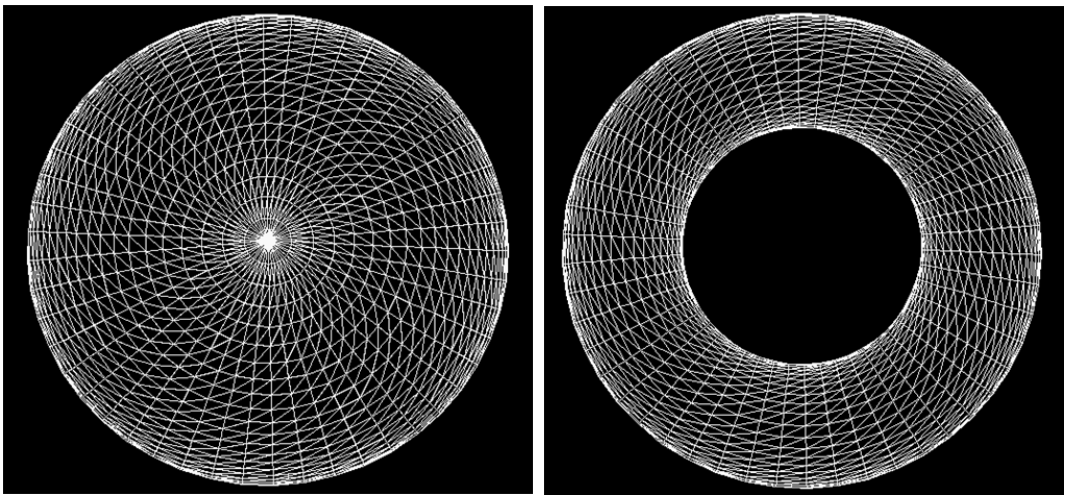

(a) Discretized disc (b) Discretized annulus

Figure 5.6.: (a) The discrezized disc with triangles. (b) The discrezized annulus with triangles.

discretization in radial direction, the power of the radial meshing and the number of arcs. With this method also curvatures and complex shapes can be created. Almost all complex shapes of the XENON1T model have been implemented using this technique. Therefore the discretization of these shapes will be not discussed. The principle to discretize with rectangles and wires will be shown in the next subsections.

### 5.2.3. Cylinder Shell Discretizer

Another shape is the cylinder shell. This shape is chosen for explaining how to discretize a surface with rectangles.
For the discretization the cylinder shell is subdivided into several stripes $M$. Every stripe is discretized into $N$ rectangular primitives with a power of $P$. The following command shows, how to create a rectangular primitive in DGeoBag:

```
1 KGMeshRectangle* rec = new KGMeshRectangle(r0, r1, r2, r3);
2 AddElement( rec );
```

Listing 5.2: The creation of an rectangle primitive in DGeoBag.

where r0, r1, r2 and r3 are the corner points of the rectangle. The total amount of subelements is then given by $N \cdot M$. It is a very simple technique to discretize rotational surfaces and doesn't need too much elements. Huge quadratical surfaces should always been discretized into rectangles in order to minimize the total count of subelements.

### 5.2.4. Wire Mesh Discretizer

The wire mesh, e.g. for the cathode of XENON1T, consists of several parallel wires and has the shape of a disk. The coordinate origin is in the center of the wire mesh. The x-coordinates of the start and end point for each wire is given by: $x_{start} = \sqrt{(d)^2 - p^2}$ and $x_{end} = -xstart$, where $d$ denotes the diameter of the disc, $p$ the distance between the first wire and the current wire, $x_{start}$ the start point of the wire and $x_{end}$ the end point of the wire. The y-coordinates is given by $p$ and the z-coordinates are fix. Each wire gets discretized into several wire primitives. N. b. in principle it is also possible to use

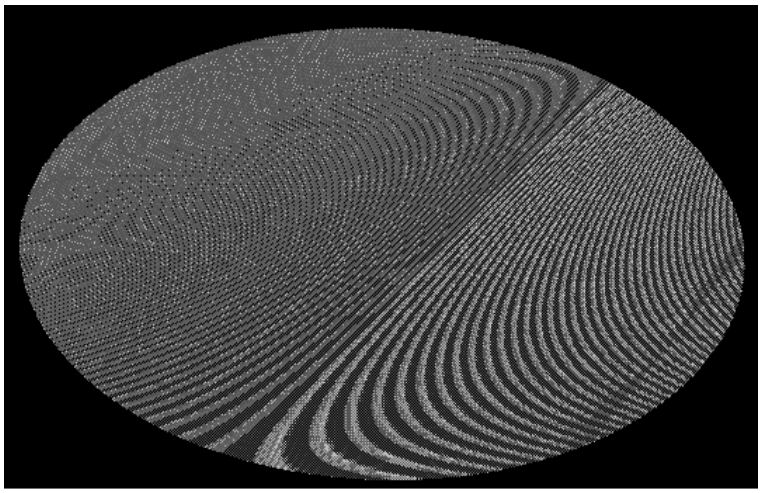

Figure 5.7.: The wire mesh discretized with wires inside DGeoBag. It has been designed to fit in several geometries, which uses a wire mesh. This wire mesh consists of about 190 parallel wires, which got discretized in smaller sub-elements. Due to VTK there are some reflections on the wires surfaces.

only one long wire primitive, but then the assumption of a constant charge density of the primitive doesn't hold valid. The following command shows how to create a wire primitive in DGeoBag:

```
1 KGMeshWire* wire = new KGMeshWire(w0,w1,d);
2 AddElement( r );
```

Listing 5.3: The creation of an rectangle primitive in DGeoBag.

w0 is the start point of a wire, w1 is the end point of a wire and d is the diameter of the wire. Figure 5.7 shows the discretized wire mesh visualized with VTK. We can see that this shapes consists of several parallel wires. This wire mesh is designed for the cathode, anode, gate and the protection grid of XENON1T. It is also possible to change the pitch and diameter of the wires and the diameter of the wire mesh. Because this shape needs a lot of subelements, the discretization has investigated more in detail in order to decrease the number of subelements.
A common discretization rule for the wire segments established by Dr. Ferenc Glück is that the size of an subelement should be one magnitude smaller or equal than the distance to the next subelement (F. Glück 2013, pers. comm.). This rule is needed to maintain the assumption of a constant charge density along the primitives and to guarantee precise results for the fields and potentials calculations:

$$e \leq d, \tag{5.1}$$

where $e$ is the subelement size and $d$ the distance to the next subelement. With a small wire pitch of $d = 0.005$ m and a wire mesh diameter of 0.90 m, the wire mesh consists then of about 360000 subelements. To save some subelements and to accelerate the computation, the discretization of the wire mesh has been investigated in more detail.
Therefore two parallel wire grids with a distance of 0.005 m have been build up. The wire grids consist also of several parallel wires with a pitch of 0.005 m. The wires have a length of 20 cm. The discretization of the wires has been changed and the charge densities have been calculated with the Robin Hood algorithm. Figure 5.8 shows the charge density for

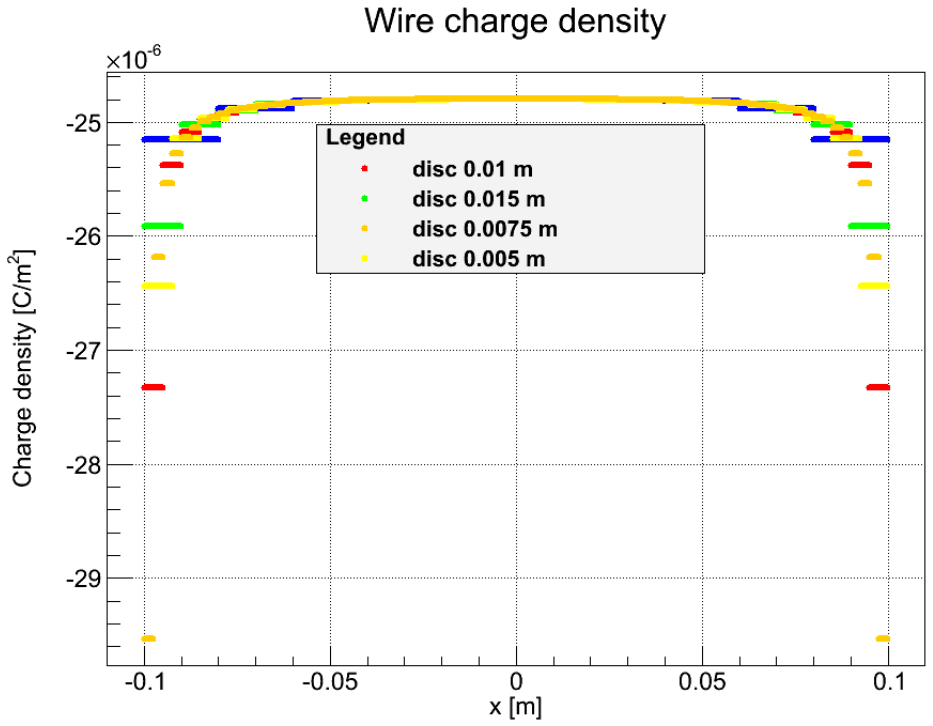


Figure 5.8.: The charge density for different discretizations. The points show the charge density along the wire in the middle of the grid. For the yellow line the wire has been discretized in 0.005 m big sub-elements. The other lines show the charge density for a more coarse discretization.

different discretizations along one wire in the middle of the grid.

We can see that at the end points of the wire, the charge density changes a lot for different discretization parameters. Therefore we have to discretize the edges of the wire array very fine in order not get a bad accuracy. In the center of the wire, the charge density is almost constant, hence we can discretize the center of our wire mesh more coarse to save some subelements. The wire mesh in the DARWIN routines have been implemented by taking these results into account. In this way it was possible to save some subelements and to speed up the simulation.

## 5.3. Electrostatic Simulation of a realistic XENON1T Model

With the new implemented shapes into the DARWIN module, it is possible to build up an exact model of the XENON1T detector. Till now it doesn't exist an exact model of XENON1T. Only axially symmetrical simulations have been performed with *COMSOL*. An exact simulation of XENON1T is necessary to analyse the later data properly.

XENON100 and also XENON1T uses the primary scintillation light to establish the energy scale for nuclear recoils. This scintillation light depends on the electric field and is taken into account by the field quenching factor $S_{ee}$. This field quenching factor has to be chosen properly for the current electric field [A+14]. Therefore an exact electrostatic simulation has to be performed for XENON1T.

For the simulation, several CAD drawings of XENON1T have been used and some assumptions have been made, e.g. the PMT arrays have been taken as a charged cylinder. The reason of this assumption was to save some subelements and to save computation time. The CAD drawings have been used for the power supply of the cathode, the Teflon reflectors of the PMT arrays and the high voltage isolation. The discretization of all shapes

has been chosen carefully in order to avoid imprecise results. A sketch of XENON1T and the drawings of the implemented shapes in the DARWIN module can be found in the appendix D E. All shapes were discretized with wires, triangles and rectangles.
For the calculation of the charge densities, the electric potentials and electric fields *KEMField* was used. To visualize the results we used ROOT.
The data output of the simulation of the charge densities is a binary file and a VTK file. The binary file contains the coordinates, charge densities, potentials etc. of the sub-elements, which are generated by *KEMField*. With the VTK file we are able to construct a three dimensional model of the geometry with *Paraview* [Hen07]. The binary file takes our field calculator as input and calculates the electric fields and electric potentials in the region of interest.
The calculations were performed with the Robin Hood algorithm using a NVDIA GTX690 graphics card. Some details of the graphic card: NVIDIA GTX680 with 1536 shader units and a memory of 2048 MB. It is not possible to allocate more than 1/4 memory on a NVIDIA graphic card for an object (array etc), because of the manufacture. So it is not able to calculate geometries which contain more than 3.2 M elements. At the end of this master thesis new graphic cards were installed (NVIDIA GeForce GTX TITAN: Shader units: 2688, Memory: 6144 MB), with this card simulations of bigger geometries are possible.

### 5.3.1. Details of the Simulation of the XENON1T Model

The XENON1T geometry was build up with 23 different shapes of DGeoBag. The geometry consists of several electrodes and dielectrics. The code for the geometry implementation can be found in the appendix C. The different applied potentials are shown in the following table:

Table 5.1.: The applied potential for the implemented geometry. The homogeneous electric field is generated by applying a potential difference across the field shaping rings.

| | PMT | Protection grid | Cathode | Gate | Anode | Vessel |
|---|---|---|---|---|---|---|
| Potential | -1.5kV | 0V | -100kV | 0V | 4kV | 0V |

Because of the long calculation time it was only possible to simulate one potential configuration. To create a homogeneous electric field along the TPC, a potential difference across the field shaping rings is applied. For the dielectrics we have to set the correct dielectric constants. The used dielectric constants are shown in the following table:

Table 5.2.: The used dielectric constants for liquid- xenon, gaseous xenon, Teflon and vacuum. The difference between the dielectric constants of liquid xenon and Teflon is not huge.

| | liquid Xenon | gaseous Xenon | Teflon | vacuum |
|---|---|---|---|---|
| $\epsilon_r$ | 2 | 1 | 2.1 | 1 |

We can see that the dielectric constant for liquid xenon and Teflon are almost the same. In this simulation we implemented the Teflon parts into the liquid xenon phase. Another simulation should be performed without Teflon in the liquid phase if an implementation of TEFLON parts is needed. If these Teflon parts are not needed, then we can speed up our

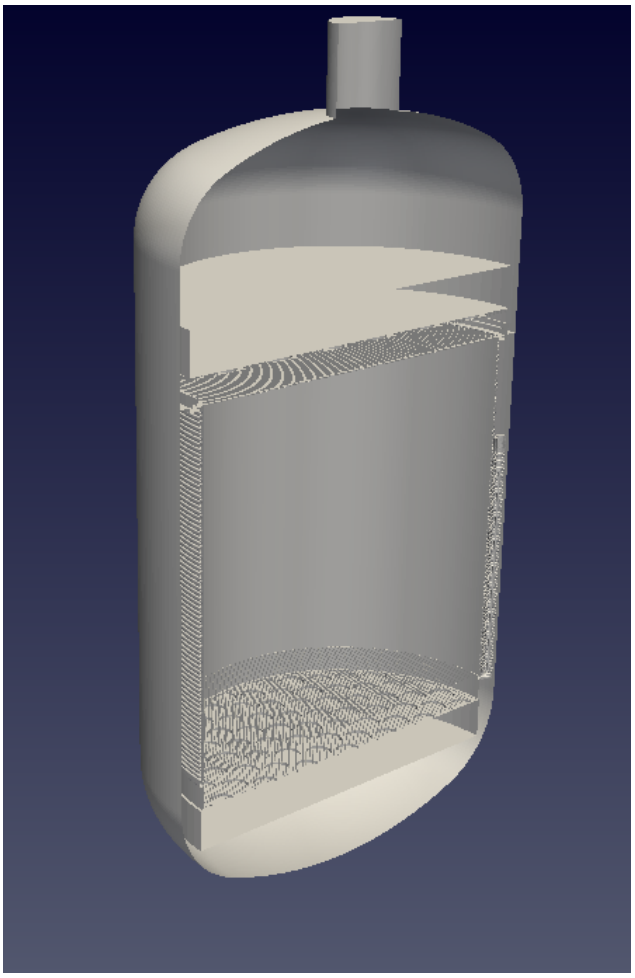

Figure 5.9.: The assembled XENON1T geometry. It consists of electrodes and dielectrics. Detailed drawings of the different shapes can be found in the appendix. The geometry consists of 3.1 million elements. The most elements are triangles.

simulation significantly. Figure 5.9 shows the implemented XENON1T geometry into the DARWIN module. The VTK file has been visualized with Paraview. The calculation time of the charge densities took $\approx$ 16 days. The calculation time was time consuming because the geometry consists of $\approx$ 3.1M sub-elements, a lot of dielectrics are used and the most subelements are triangles $\approx$ 2M. It would be possible to speed up the simulation by using more then one GPU but they had been in use at this time. The calculation time of the electric potentials and electric fields in the region of interest took $\approx$ 24h. The reason for such a long computation time for the electric fields and electric potentials is quiet simple. *KEMField* calculates the electric field and electric potentials for every subelement at a given field point $P$ analytically and sums up the potentials and electric fields of every subelement. So 30 ROOT plots have been created. In the next section the results of this simulation will be discussed.

### 5.3.2. Results of the Electrostatic Simulation of XENON1T

In this section we will investigate the results of the XENON1T simulation. This was the first simulated dual phase detector with *Kasper*, so we have to ensure the correctness of these results. Therefore we created field maps, potential maps and calculated the electric field and electric potential at different regions inside the TPC. For e.g figure 5.10 shows the electric field along the z-axis 5mm in front of the Teflon reflector from the field shaping

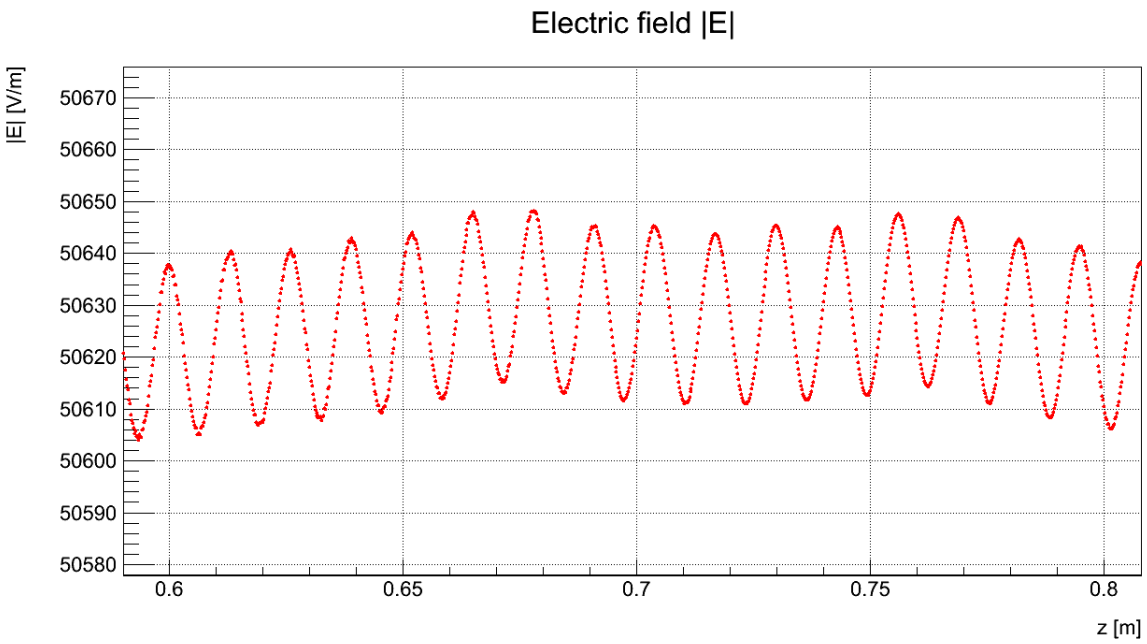


Figure 5.10.: The electric field in front of the field shaping rings. The electric field varies because of the small gap between the different field shaping rings.

rings. The electric field varies here, because of the field shaping rings. The field shaping ring structure was optimized to minimize these variation in the near of the field shaping rings. It can be seen that the optimization of the field shaping rings delivers a relative stable electric field.
Also the other generated plots were investigated in advance for anomalies in the electric field and electric potentials. In this study we discovered something important about our simulation package. In the most plots we saw strange behaviour of the electric fields. E.g. figure 5.11 shows the radial electric field in radial direction in the middle of the TPC $z = 0.5$. We see that the electric field varies a lot. The multiple-valued function is due to fluctuations of the field values between close field points. The question is, where are these fluctuations coming from and do we have the same issues in the KATRIN experiment?
Till now nobody had a closer look at the simulated electric fields of the KATRIN experiment. Therefore the electric fields and the electric potentials of the KATRIN experiment has been calculated and they also showed a fluctuation. The plots can be found in the appendix F.
This strange behaviour of the potential and the field results indicate for some kind of numerical error in the calculation of the electric field and electric potential or a discretization error.

#### 5.3.2.1. Numerical Error of the Simulation

The numerical error could come from different sources:

- For the calculation of the electric field and electric potential a few million of numbers have to be summed up. In this step we can lose some accuracy.
- The calculation of the electric field and electric potential of every subelement could have some round-off errors.

To avoid the first point a special algorithm is already implemented into *KEMField* to control the summing up of the numbers. The Kahan summation algorithm [Kah65], which significantly reduces the numerical error by adding a sequence of finite precision floating

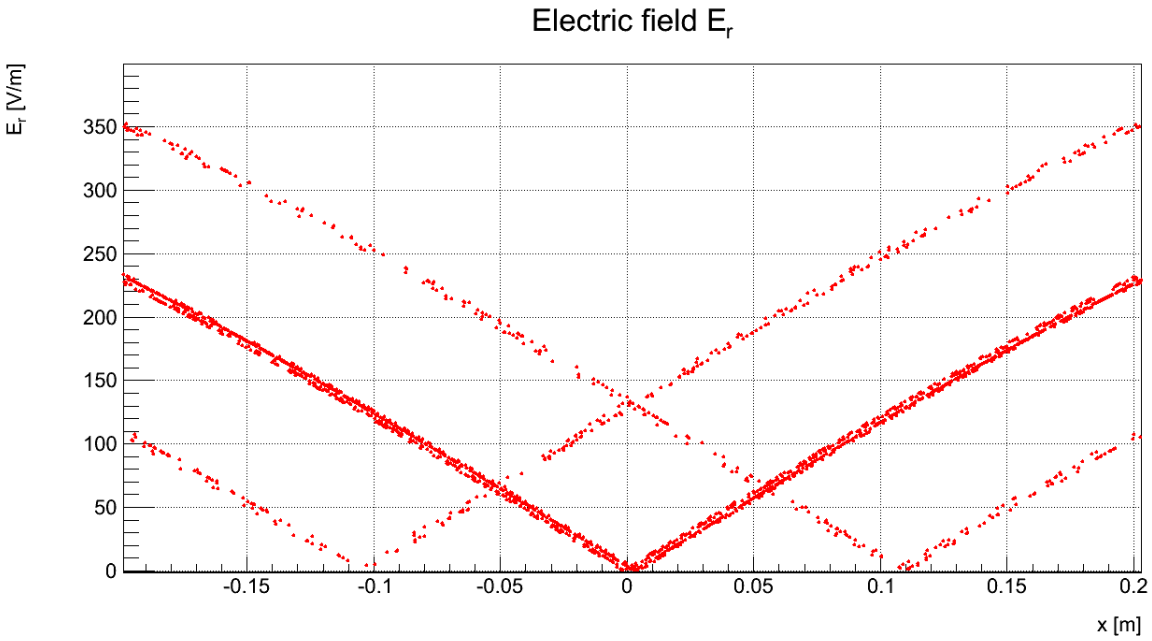


Figure 5.11.: The radial electric field in radial direction at $z = 0.5$. We got a multiple-valued function due to fluctuations of the field values.

point numbers, is already implemented into *KEMField*.
To avoid the second point new field calculation methods are needed. It seems that the overall numerical errors are more sensitive to the triangles than to the rectangles and wires. One suggestion from Dr. Ferenc Glück was to develop a numerical cubature method for triangles. We saw in subsection 3.3.3 that for the calculation of the electric potential and electric field of a triangle an integral of the following form has to be calculated:

$$\int_A f(\alpha, \beta, \gamma) dA. \tag{5.2}$$

$\alpha$, $\beta$ and $\gamma$ are new defined natural co-ordinates for a point $Q$ of the triangle. These coordinates are defined as follows:

$$\alpha = \frac{A_1}{A}, \beta = \frac{A_2}{A}, \gamma = \frac{A_3}{A}. \tag{5.3}$$

where $A$ is the area of the triangle and $A_1$, $A_2$, $A_3$ are the the created areas by a point $Q$ on the surface of the triangle. Figure 5.12 shows the used coordinate system for a triangle. The integration of 5.2 for a triangle is now performed with the Gaussian quadrature rule instead of using the Newton-Leibniz method [Dun85].

$$\int_A f(\alpha, \beta, \gamma) dA = A \sum_{i=1}^{ng} w_i \cdot f(\alpha, \beta, \gamma) \tag{5.4}$$

Where $w_i$ is the Gaussian weight for the i-th sampling point and $ng$ the number of sampling points. So we can see from equation 5.4 that with the numerical cubature method, the complex integral for the electric potential and electric fields of a triangle can easily been calculated by approximation the area of the triangle with weighted point charges. This new field calculation routine has been developed and implemented into *KEMField*. The new field calculation routine can be found in the appendix F. We computed the triangle

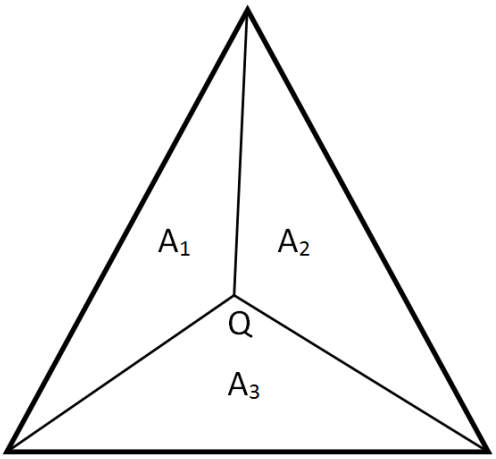


Figure 5.12.: A point $Q$ in the triangle creates three different areas $A_1$, $A_2$ and $A_3$. The coordinates of the point Q is given by $\alpha = \frac{A_1}{A}$, $\beta = \frac{A_2}{A}$ and $\gamma = \frac{A_3}{A}$.

in our implementation with seven point charges ($ng = 7$). The corresponding Gaussian weight $w_i$ and the coordinates $\alpha$, $\beta$ and $\gamma$ can be found for this configuration in [Dun85]. This assumption of course only holds valid for field points far away from the triangles and has been considered in the implementation. If the distance from the triangle to the field point divided by the averaged side lengths of the triangle is bigger than 60, then the new calculation routine will be used otherwise the old routines will be used. The electric potential and electric field of a point charge $Q$ is given by the following formula [Gri07]

$$\phi = \frac{q}{4\pi\epsilon_0} \cdot \frac{1}{r} \tag{5.5}$$

$$\vec{E} = \frac{q}{4\pi\epsilon_0} \cdot \frac{\vec{r}}{r^3}. \tag{5.6}$$

A first test with the new implemented 7-point numerical cubature method have been performed with the KATRIN geometry. The plots can be found in the appendix F. Also the radial electric field in figure 5.11 has been recalculated. Figure 5.13 shows the radial electric field calculated with the new developed 7-point numercial cubature field routine. We see that the fluctuation of the radial electric field disappeared in the simulation with the 7-point numerical cubature method. The implementation into *KEMField* was successful. Only a implementation for calculation on CPUs has been performed a GPU implementation is necessary as well to speed up the calculation and to check the whole XENON1T geometry.

#### 5.3.2.2. Discussion of the Discretization Error

Another source of this behaviour could be the discretization scale. It could be that the discretization rule wasn't set precise enough at sensitive points of the geometry, so we get at some points a good discretization and at other points we lose accuracy because of the bad discretization. Another source could be that some subelements of the geometry overlap and leaps to these result. Therefore the geometry has to investigate more in detail in the future. Overall we saw that is now possible to simulated different types of dual-phase detectors. The problems with the numerical error of the electric field has been solved by implementing a new field calculation routine into *KEMField*. In the next chapter the hardware work for the XENON1T detector will be discussed. In the next chapter the hardware work for the XENON1T detector will be discussed.

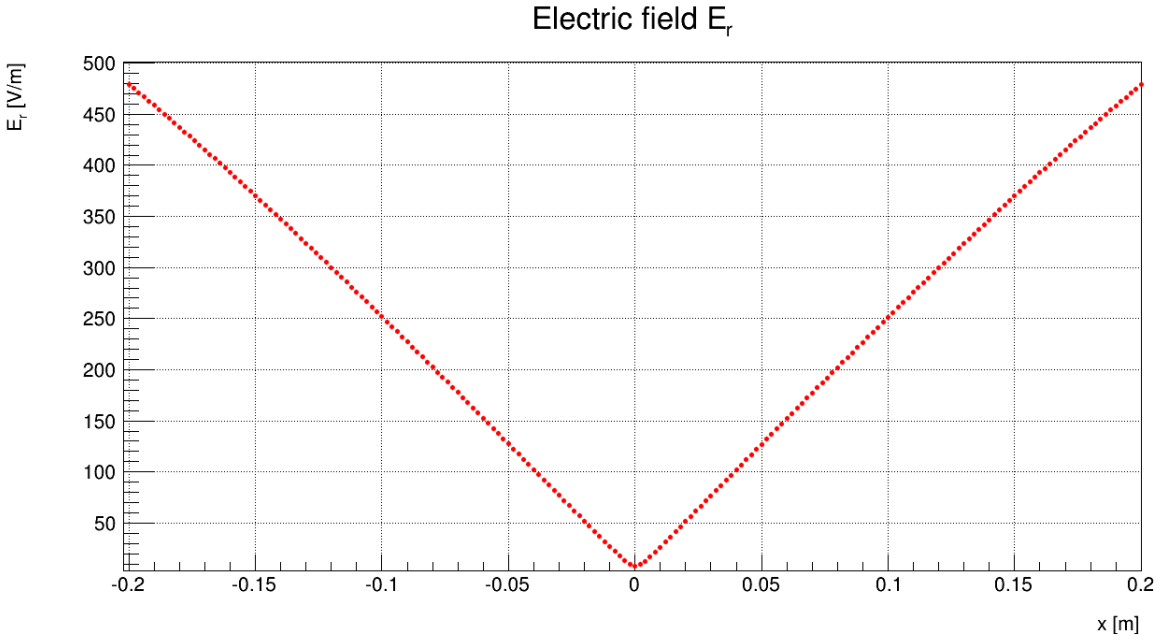


Figure 5.13.: The radial electric field in radial direction at $z = 0.5$ calculated with the implemented 7-point numerical cubature. The fluctuations of the electric field disappeared.

# 6. Low-Temperature Hardware Tests for the XENON1T Experiment

In this chapter the results of two different low temperature tests will be discussed. The main design for XENON1T is fixed but several smaller questions are still open and have to be investigated by the XENON groups. At the XENON group in Zürich, several low temperature measurements in liquid and gaseous xenon are performed with focus on low-temperature PMT tests. In context of these measurements, an amplifier PMT test and a bell test have been performed.
The goal of the amplifier PMT test was to test two different kinds of amplifiers for PMTs. The amplification of the PMT signals results in higher gains at lower voltages, which would allow for higher linearity, lower power consumption and a better usage of the dynamic range. The goal of the bell test was to find a new solution to stabilize the liquid-gaseous-xenon interface for dual-phase detectors. For the amplifier test and the bell test a special setup has been developed and installed inside the MarmotXL setup. The setup and the results of these tests will be shown in the following chapter.

## 6.1. Presentation of the experimental Setup for Low-Temperature Tests

The MarmotXL setup, which is installed at the laboratory of the XENON group at the university Zürich, is the second generation setup from the XENON group in Zürich. The MarmotXL setup consists of an enclosed in the vacuum insulated cryostat, a gas system, a DAQ-System, a PTR (Pulse tube refrigerator Iwatani PDC08 [GAC+11]) and several feedthroughs. All the structures are made of stainless steel, aluminum and cooper. Several kilos of xenon are able to pump into the cryostat. The PTR is used to cool down the xenon and to hold this temperature over a long time. The gas system is quite complex. It consists of one storage cylinder for the xenon filling and one storage cylinder for recuperation, a high pressure line, a regulator, a low pressure line, a getter for purification and a recirculation line containing buffer volume and a pump. In the main recirculation loop, the liquid is extracted trough a siphon tube from the detector chamber to a buffer volume to guarantee that the xenon is in gas phase. Afterwards a recirculation pump pushes the gas through the purification module (a heated getter) and from there, the gas enters the detector again. The flow is manually controlled with a needle valve and the recirculation rate is given by the reading of the calibrated flow-meter. [Gro14]

All relevant parameters as temperature, pressure, heater output, gas flow, compressor status and SMS/e-mail alarming in case of anomalous data of the MarmotXL setup are controlled by the MarmotXL slow control. The data is collected and stored by C-applications and several plots that can be seen on a slow control web page are created using ROOT.

## 6.2. The Amplifier PMT Test at Low-Temperatures

The main goal of the Amplifier-PMT-Test was to make a detailed study about the Hamamatsu R11410R11410-21 PMTs in connection with different amplifiers. Two different types of amplifiers were investigated in this experiment. The Philips PS776 [Sci14] amplifier, which is already in use in the XENON100 experiment, and a new selfmade amplifier from the electronic workshop in Zürich, called UZH amplifier. The UZH amplifier is based on microelectronics. Five PMTs in connection with the two different amplifiers were tested (KB055, KB127, KB138, KB145 and KB150). The reason to use five PMTs was simply to get more statistics. First the PMTs were connected with the ADC (analog digital converter) module and the signals were acquired. Afterwards, the PMTs cables were connected to a Phillips-Amplifier (x10) and the UZH-Amplifier (x10) and the measurements were repeated. All measurements were performed in dark, in use of a fiber optic setup and with different high voltage settings. The following sections describe the results of each measurement phase.

### 6.2.1. The Experimental Setup of the Amplifier PMT Test

For the amplifier test, five of Hamamatsu R11410R11410-21 PMTs are installed inside the MarmotXL cryostat. To read out the PMTs, a special electronic circuit, called base, was used. The same base will be used for XENON1T. The base has the task to supply the cathode and every dynode with high voltage and transports the signal to the DAQ. Every dynode of the PMT will be supplied by a different voltage to accelerate the electrons from dynode to dynode. For the last four dynodes a capacitor is needed to recharge the dynodes. To complete the base a 50 Ohm input impedance is used to avoid signal reflections. Every base is connected with a capton cable through the feedthrough to the high voltage. The capton cables were used to test their behaviour and handling in a low temperature environment. Also has capton a low intrinsic radioactivity. The output signal of the base is transported via a capton coaxial cable through an other feedthrough to the DAQ. A coaxial cable is used to achieve a better shielding and to minimize crosstalk. Figure 6.1 shows the circuit diagram of the PMT bases.
The PMTs inside the cryostat are facing down to a Teflon plate. To safe more liquid

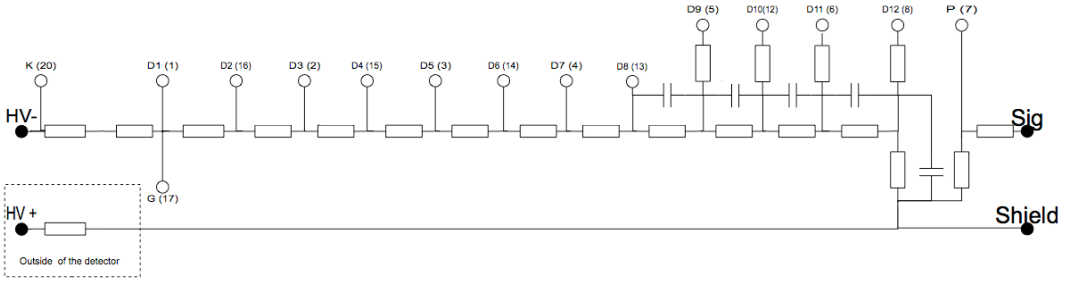


Figure 6.1.: The circuit diagram of the PMT base. The base has to supply 12 dynods (D) and one cathode (K). This special base has been developed after several PMT tests. Figure modified from [Jam14].

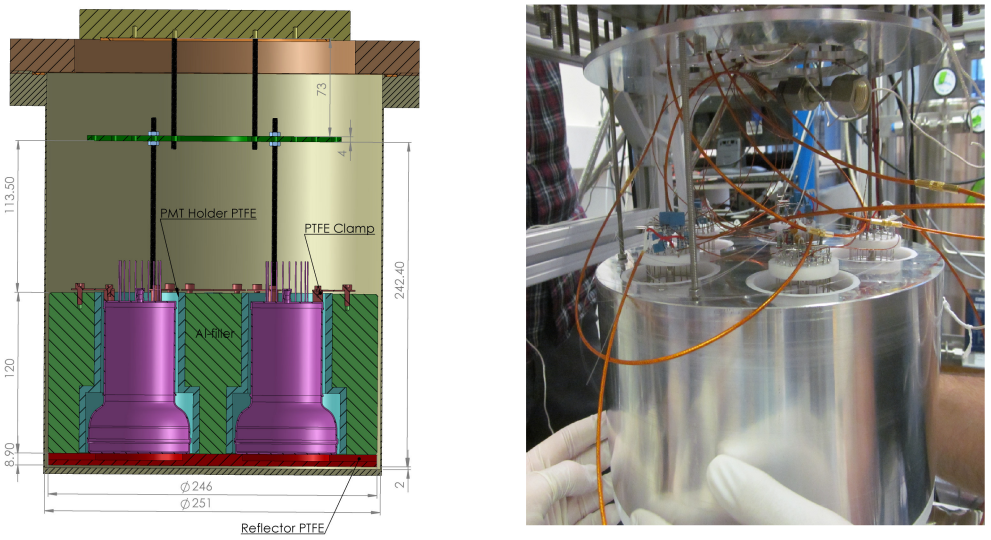


Figure 6.2.: Left: The setup inside the cryostat as CAD drawing. CAD drawing taken from [Jam14]. Right: The installed Filler, PMTs and fiber optics before closing the cryostat.

xenon all the empty space was filled up with a aluminium block. The filler/PMT holder is fixed to the aluminium plate on top by threaded rods. To create a signal for the PMTs, a fibre optic setup was installed inside the cryostat. The fibre optics setup was controlled and triggered with an external pulser. The holders and filler were constructed by the workshop of the UZH after creating the CAD drawings. Fig 6.2 shows the setup inside the MarmotXL cryostat.
The handling of the coaxial capton cables were very difficult, because they were very stiff and often the soldering to the base or to the feedthrough broke. Also to crimp the cables was a difficult task. It is not recommended to use them in XENON1T. It is recommended to use the more flexible Teflon coaxial cables. But for these cables the outgassing of the Teflon has to be studied more in detail.
For the amplifier PMT test the cryostat was filled up with gaseous xenon and cooled down. The amount of xenon was chosen to be low, because in parallel other xenon measurements had to be performed.

### 6.2.2. Electronics and Data Acquisition

The PMT signals are amplified by a factor 10 with two different kind of amplifiers and digitized are with CAEN V1724 as ADCs with 100 MHz sampling rate, 14 bit resolution, and 40 MHz bandwidth. The CAEN ADC digitizes the full waveform of the 5 PMTs, where the time window for an event is 550 $\mu s$. One sample is equal to a time window of 10 $ns$. Using circular buffers in flash ADCs, with 512 kB memory per channel, the DAQ samples continuously, and stores the data if a trigger occurs. The trigger is generated by the external pulser of the optical fibres. The measurements and data storage are performed with the XENON Data Acquisition software program (DAX). The settings for the data acquisition are defined in XML-files. For each acquired data set, it generates an ASCII log file that contains information on the measurement (file name, timing, settings) and scalar values. DAX can be also run in oscilloscope mode, which provides real time access to the digitized waveforms. All samples of an event were stored into a ROOT tree. Figure 6.3 shows the schematics of the MarmotXL-Amplifier-Test data acquisition system.
The raw data is converted into physical parameters using an self programmed Raw Data

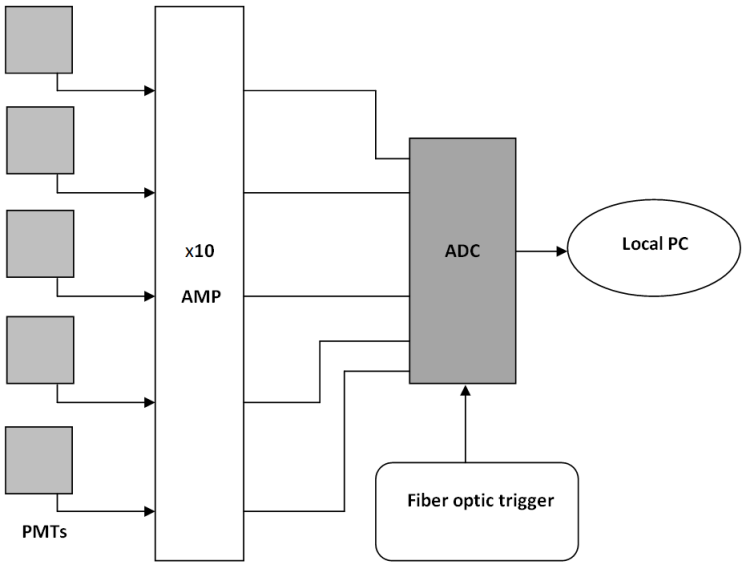


Figure 6.3.: Schematic of the MarmotXL-Amplifier-Test data acquisition system.

Processor, a ROOT based C++ program, specially developed for the amplifier PMT test data analysis called miniProcess (MP). All programs can be found on the ATP wiki of the University Zürich. In the pre-processing stage, the baseline and its derivation of each waveform is computed on the first 50 samples, and the raw waveforms get subtracted by this baseline. Afterwards the signal search in the waveform starts. Therefore the integral of the first peak after the trigger is calculated and stored. Also the integral of every peak has been stored. The integral of a peak has been calculated as follows.
The algorithm looks for the peaks in the waveform above a user defined threshold and calculates the integral of two samples before the peak to two samples after the peak to ensure to process the signal. The program also stores the position of the peaks in a waveform. In the end, a fast Fourier transformation will be calculated to obtain the frequency content. Therefore the fast Fourier transformation the FFTW C++ subroutine library were used.

### 6.2.3. Determination of the Amplification Factor for different Amplifiers

The UZH amplifier and the Philips amplifier should give an amplification factor of ten (x10), but they have an error of ±10% (A. Vollhardt 2013, pers. comm. ). So the first step was to estimate the real amplification factor for the amplifiers. The amplification factor is calculated as follows.
With the pulser, a square signal is generated. This square signal is taken as input for the ADC instead of the PMT signal. The signal is measured with and without the the amplifiers. The ratio of the amplified signal to the unamplified signal is defined as the amplification factor ($X = \frac{S_a}{S_u}$). Where $S_a$ is the signal height with and $S_u$ without an amplifier connected. Because of the electronic noise the square signal is not perfect. To calculate the amplification factor, the height of the square signal was averaged over the width of the signal. With this technique the amplification factor for the Philips amplifier was calculated to $X = 10.3$.
Figure 6.4 shows the measurement with the UZH-amplifier. A closer look at the circuit diagram of the UZH amplifier shows us that the transistors, resistors and capacitors inside the amplifier creates a RC-circuit! As a consequence, for a long constant signal the capacitor $C$ of this RC-circuit gets charged over the resistor $R$. The voltage at the resistor during the charging of the capacitor can be calculated over the following formula [Gri07]:

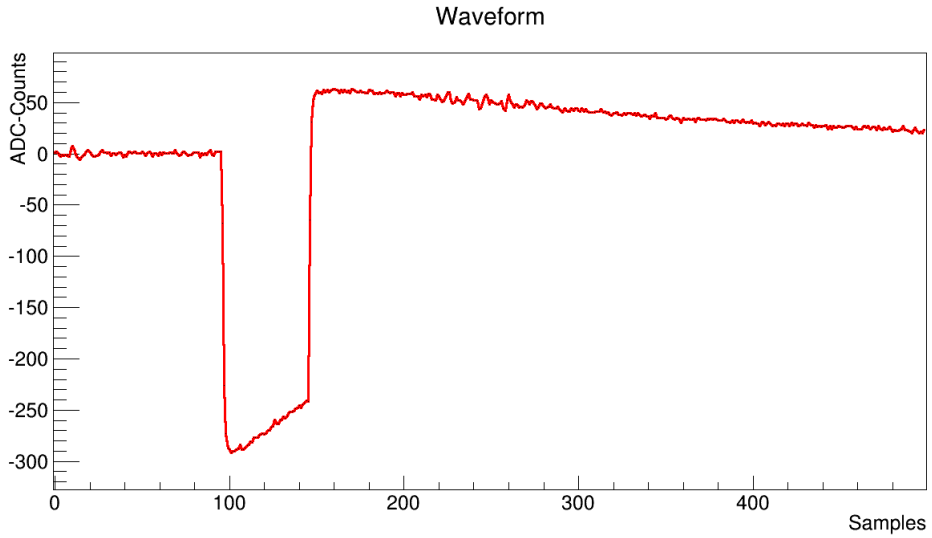


Figure 6.4.: The square signal after the amplification with the UZH-Amplifier. The square signal isn't constant and falls exponential after the amplification. This behaviour can be explained with the RC-circuit.

$$U_R = U_s \exp^{\frac{-t}{R \cdot C}}, \tag{6.1}$$

where $U_R$ is the voltage at the resistor $R$, $U_s$ is the voltage of the square signal and $t$ the time. This explains the exponential decay of the constant square signal. The tail of the waveform can be explained by discharging of the charged capacitor over the resistor.

$$U_R = U_c \cdot \left(1 - \exp^{\frac{-t}{R \cdot C}}\right). \tag{6.2}$$

Where $U_c$ is the voltage at the capacitor. This explanation has been also confirmed with a simulation of the RC-circuit.
This particular behaviour of the UZH amplifier described above didn't take any effect on the amplifier PMT test, because the signals of the PMTs are very short and so the amplifier doesn't affect our measurements. The determination of the right amplification factor was more difficult. The amplification factor was calculated with the highest peak of the square signal and was determined to $X = 10.6$.

### 6.2.4. Discussion of Electronic Noise

In the first measurement phase the signals of the PMTs were acquired without a light source. This measurement was performed without an amplifier, with the Philips amplifier and with the UZH amplifier. Because of the darkness inside the chamber this measurement gives us the electronic noise of the PMTs with and without the two amplifiers.
200000 events, were measured with a sampling frequency of 100 MHz to create the noise spectrum. For a finer frequency resolution another measurement has been started with a sampling frequency of 35 MHz and a waveform length of 135000 samples. The data has been reprocessed with miniProcess and visualized with a ROOT program. The first measurement showed that there is a lot of noise in the waveforms with both amplifiers. Figure 6.5 shows the reprocessed waveform of PMT1 (KB055) and the frequency content of the waveform with the UZH amplifier. The noise appears in the waveforms of all PMTs and with both amplifiers.
The frequency content of PMT1 shows this in more detail. The frequency range of the

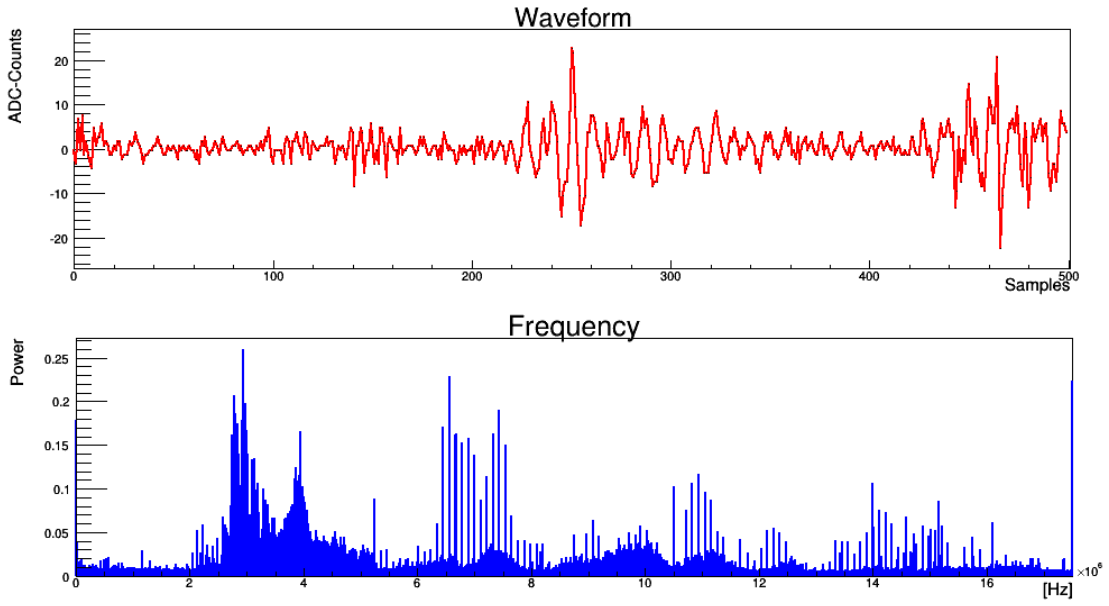


Figure 6.5.: Upper Plot: The Reprocessed waveform of PMT1. There are big noise burst inside the waveform. Bottom Plot: The calculated frequency content of PMT1.

noise is very wide and so it is very complicated to find the source of the noise.
To determine the source of noise in such a complex setup is very complicated. Several things have been tested to find the source. At the first step the coaxial cables have been checked and renewed with shorter double shielded coaxial cables. This had the effect that the cables are better shielded versus electromagnetic radiation from other experiments inside the laboratory. The effect was measurable, but there were still some smaller noise bursts in the waveforms.
The next step was to use another power supply module, which delivers a better constant voltage. After replacing the old external power supply module with a NIM (Nuclear Instrumentation Standard) power supply module the burst peaks disappeared. So the old power supply didn't deliver a constant voltage. The high voltage cables inducted a signal into the signal cables, because the high voltage cables inside the cryostat and at the feedthrough are nearby to the signal cables. After reducing the noise, it was possible to make a comparison between the two amplifiers.
There was no significant difference in the noise spectra. With the Philips amplifier we saw that the baseline of the waveform varies with a frequency of 50 $Hz$, which is the frequency of the power supply. This effect was not very high but measurable. Figure 6.6 shows the low frequency content of the waveform with the Philips amplifier and the UZH amplifier. Any frequencies over 500000 Hz haven't been seen for both amplifiers. Only electronic noise has been detected. We can see that the low frequency spectrum of PMT1 with the two different amplifiers is very similar. The low frequencies with the Philips amplifier are slightly higher than with the UZH amplifier. The Philips amplifier is not very resistant against any kind of noise source compared to the UZH amplifier. Till now for the UZH amplifier doesn't exist any type of shielding. It is a open circuit board, which has been shielded with aluminium foil. If we shielded our UZH amplifier with a metal box, we would probably get lower noise.

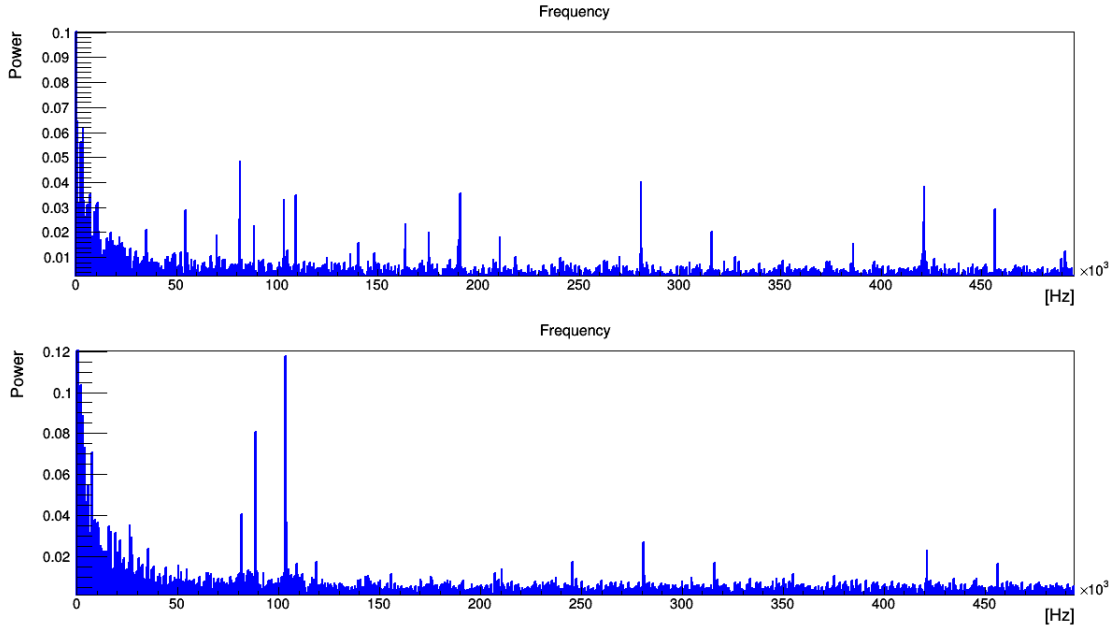


Figure 6.6.: Upper plot: The noise spectrum of PMT1 in connection with the UZH-Amplifier. Bottom Plot: The noise spectrum of PMT1 in connection with the Philips-Amplifier.

### 6.2.5. Determination of the PMT Gain with different Amplifiers

A very important parameter for the XENON100 and XENON1T experiment is the gain of the PMTs. The PMT gain is determined as the mean number of electrons produced by a phototube in response to one photoelectron (PE). The energy deposit for nuclear recoils $E_{NR}$ in XENON100 and XENON1T is calculated over the scintillation light. Hence it is necessary to measure the gain very precisely. The gain can be measured by using a very weak light source, which produces one photoelecton at the PMT cathode.
For this test the optical fibre setup is used to create weak light pulses. The hardware system for the PMT measurements with LEDs has been set up as shown in 6.7. The pulse generator provides two output channels. The first output channel is connected to a light-tight box with a InGaN ('blue') LED (Light-emitting diode), which emits blue light with an average wavelength of 470 nm. The second output channel is connected to the ADC. The light from the LEDs is transferred by one standard coated optical fibre (1 mm core) to the optical feedthroughs of the detector. In order to diffuse the light and to achieve an uniform illumination of all PMTs, the quartz fibres are connected inside the cryostat to a bundle of polymethylmethacrylate (PMMA-PFA) fibers with 180 $\mu m$ core [Kis11]. The total amount of light produced by a LED depends on the amplitude of the pulse and on its time width. In order to achieve a single PE level for PMT illumination, the

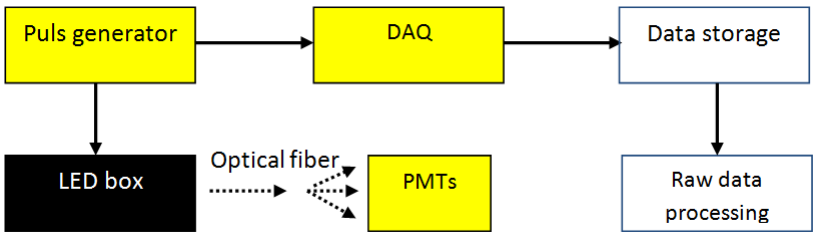


Figure 6.7.: Schematic of the optical setup for the PMT amplifier test.

amplitude of the pulse has been set to the minimum required to turn on the LED. The light pulse was set to a period of 1.5 $\mu s$ and a pulse width of 0.5 $\mu s$. The voltage for the light intensity was set as low as possible to create a single photo electron. Therefore the DAX has been running in oscilloscope mode to have a closer look when the PMT starts to response. Figure 6.8 shows a raw waveform of PMT1 in the oscilloscope mode. Ideally, all PMTs should be uniformly illuminated, so that each phototube detects light on the level of single PE. Since the optical fibers for illumination of PMTs inside the cryostat are very disorganized, the amount of light is not the same for every PMT. So for every PMT the light pulse intensity has be varied. The first measurement has been performed without an amplifier.
100.000 events have been measured in 5 min. The raw data was reprocessed with the miniProcess, where also the pulse area is calculated. The spectrum of PMT1 induced by the LED light is shown as integrated ADC counts in Figure 6.9. The response of the PMT is described by a sum of two functions, describing the noise peak and the single PE peak. The noise peak is usually fitted by a Gaussian function as well as the single PE peak. If two photoelectrons have been created at the cathode, then a second single photon electron peak appears. This peak is also described by a Gaussian function. These have the following form:

$$F(x) = h \cdot \exp^{\frac{-(x-\mu)^2}{2\cdot\sigma}}, \tag{6.3}$$

where $h$, $\mu$ and $\sigma$ are the fit parameters. The integrated ADC counts are converted to PMT gain as following [Kis11]:

$$g = \frac{\mu \cdot r}{f \cdot A \cdot Z \cdot e}, \tag{6.4}$$

where $g$ is the gain, $\mu$ the mean of the single PE peak , $r$ the ADC resolution ($2.25/2^{14}[V/Bit]$), $f$ the sampling frequency, $X$ the amplification factor, $Z$ =50 Ω and $e$ the electron charge. We have to fit the whole spectrum to get the correct value for the PE peak. The fit and the visualization is performed by a self programmed C++, ROOT based program. Several

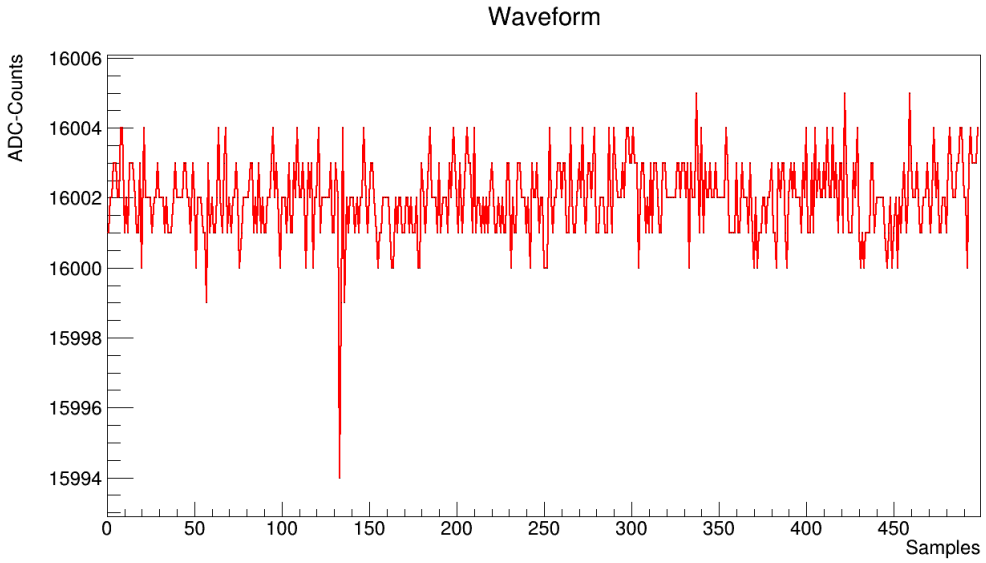


Figure 6.8.: A raw waveform of PMT1 without an amplifier. The signal was created with the optical fibre setup. The intensity of the optical fibre setup was set to a very low value ($\propto mV$). The light pulse is created between the 100th and the 150th sample.

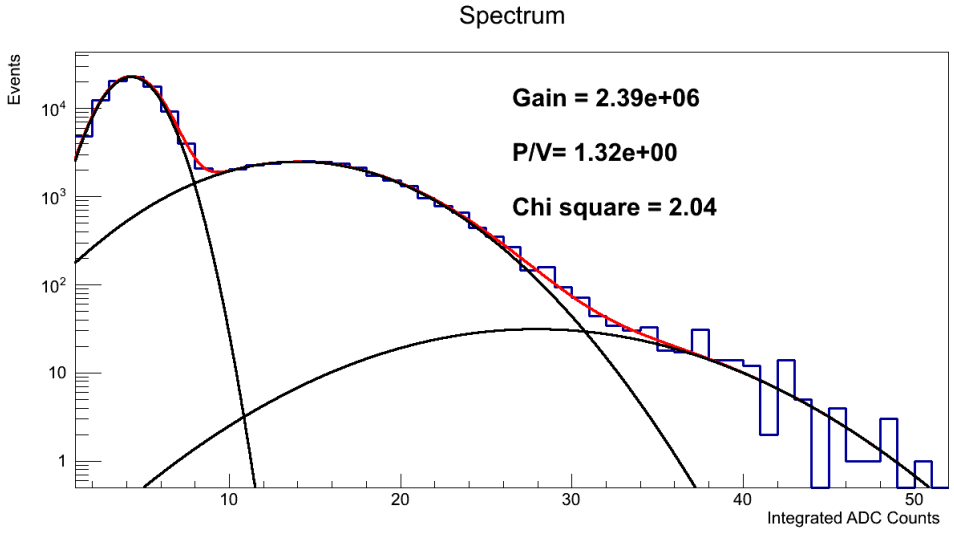


Figure 6.9.: The PMT spectrum of PMT1 without an amplifier. The noise peak, single-photo-electron-Peak (SPE) and the second SPE peak are fitted with Gaussian functions. The red curve is the whole fit of the spectrum.

additional parameters are also determined, such as the single photoelectron resolution, peak-to-valley, and signal-to-noise ratio. Figure 6.9 shows the spectrum of PMT1 without using an amplifier.
We see that without an amplifier the SPE-peak is very close to the noise peak. For most of the PMTs, a Gaussian function is a good approximation of the noise distribution. It is complicated to fit the SPE correct. The second SPE-peak is very small, because we configured the intensity of the LED very low, but high enough to see the SPE peak. The 'peak-to-valley' ratio is calculated as the ratio of the height of the single PE peak and the valley after the pedestal, and thus quantifies the separation of the noise and signal. The gain was measured to: $g = 2.39 \cdot 10^6$. And the peak-to-valley ratio is 1.32. The peak-to-valley ratio is low because of the near noise peak. The other four PMTs showed the same behaviour and will be not shown. The next measurements were performed with the two different amplifiers. The created spectra can be found in the appendix G.
We see that the noise peak is very far away from the SPE peak with the two different amplifiers. This also confirms the 'peak-to-valley' ratio. Table 6.1 shows the comparison of all relevant parameters of PMT1.

Table 6.1.: The values peak-to-valley and gain of PMT1 without an amplifier, with the Philips amplifier and the UZH amplifier.

| | NO AMP | Philips AMP | UZH AMP |
|---|---|---|---|
| Gain | $2.39 \cdot 10^6$ | $2.4 \cdot 10^6$ | $2.47 \cdot 10^6$ |
| Peak-to-valley | 1.32 | 4.00 | 4.13 |

The best peak-to-valley value delivers the measurement with the UZH amplifier. The results for the gain are slightly different between the Philips amplifier and the UZH amplifier. This difference could result from a wrong determined value of the amplification factor of the UZH amplifier (see subsection 6.2.3). Another explanation could be a too low voltage for the UZH amplifier. The UZH amplifier is till now an experimental one and its

power supply must be configured by hand. The Philips amplifier instead has the Nuclear Instrumentation Module (NIM) Standard.
We can also see in the spectrum a plateau between the noise peak and the SPE peak with both amplifiers. In principle there should be a very deep valley. It could be noise, but normally the noise rises only till 20 integrated ADC counts and the number of events is much higher than expected. Another explanation could be that this plateau comes from the photoelectrons, which were created at the first dynode. This is a new observed effect with the Hamamatsu R11410R11410-21 and from now on under investigation. To be able to fit the spectrum we fit a gaussian between the noise peak and the SPE. This Gaussian should describe the electrons from the first dynode. We saw this behaviour also for the other four PMTs.

### 6.2.6. Results

This experiment showed us some interesting facts about the Hamamatsu R11410R11410-21 PMTs in connection with an amplifier. Using an amplifier has the advantage to determine the SPE peak very well. With this measurement it is possible to calculate the gain of a PMT very precisely. We also saw that using an amplifier showed us a not well understood spectrum for the Hamamatsu R11410R11410-21 PMTs. The plateau between the noise peak and the SPE peak has to be investigated. To confirm that this plateau comes from the first dynode, a new experiment is needed but not discussed in this thesis.
The suggestion is to design a new base, which delivers no high voltage to the cathode. So only light which hits the first dynode creates a photon-electron. If the spectrum gets shifted to the value of the plateau, the theory is confirmed.
With this experiment we also compared a new selfmade amplifier with the old Philips amplifier. The experiment showed us no big difference between the Philips amplifier and the UZH amplifier. The UZH amplifier is slightly better and should be used for the XENON1T experiment, because of its microelectronics. The Laboratori Nazionali del Gran Sasso is housing a lot of experiments and therefore a good electromagnetic shielding is needed. Shielding the small component of the UZH amplifier is easy and the microelectronics is more resistance against electromagnetic radiation.

## 6.3. Test of a new Technique to stabilize the liquid-gaseous Level in XENON1T

Also a bell test has been performed at the MarmotXL setup. As a possible way to control the level of the liquid xenon inside a TPC is using a 'bell' (diving-bell). This method is used in the XENON100 experiment and should be also used for XENON1T experiment [Col10]. To control the xenon level, xenon gas is pushed inside the bell. The xenon level is measured by capacitive level meters. This technique was very complicated to handle in the XENON100 experiment. The main purpose of this bell test is to check the feasibility of using a heater to control the liquid level and to test the stability and control ability of this method. Using a heater increases the pressure inside the bell. Adjusting the heating power will adjust the liquid level inside the bell.

### 6.3.1. Experimental Setup of the Bell Test

For this test a diving bell, which consists of a cylinder with a cover plate welded on top of it, was installed into the MarmotXL cryostat. The empty space around the bell was filled up with aluminium fillers to safe xenon. For the heater a special Teflon holder was designed. The heater is placed in the center of the Teflon holder. If the heater is turned on it will vaporize the xenon. This gaseous xenon will go through the holes of the Teflon

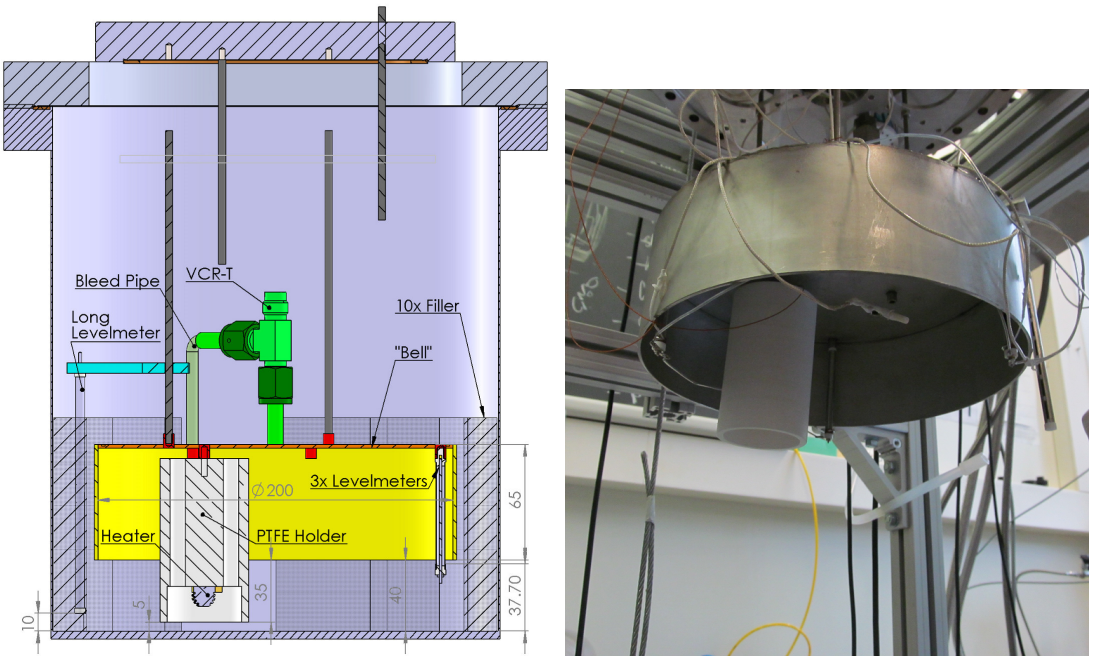


(a) The CAD drawing

(b) The installation

Figure 6.10.: (a) The CAD drawing of the bell test. To safe xenon alumium fillers were used. CAD drawing taken from [Jam14] (b) The setup of the bell test before closing the cryostat. The level meters are connected with coaxial cables, which go to the feedthrough.

holder inside the bell. This should avoid bubbles at the liquid-gasous xenon interface and adjust the xenon level.
The heater were controlled simply by hand with a power supply module. During operation, the bell is submerged in liquid xenon and has gaseous xenon inside. To monitor the level of the liquid xenon inside the bell, three capacitive level-meters are mounted inside the bell. The level meters are cylindrical capacitors, which change their capacitive with the xenon level. This behaviour can be described by the following formula [Gri07]:

$$C = 2\pi\epsilon_0\epsilon_r \frac{l}{ln\left(\frac{R_2}{R_1}\right)}, \tag{6.5}$$

where l is the length of the capacitor, $R_1$ is the inner radius, $R_2$ is the outer radius and $\epsilon$ is the electric permittivity of liquid xenon ($\epsilon_r = 2$). Figure 6.10 shows the CAD-Drawing of the setup and the installation into the MarmotXL cryostat. The bell, the level meters and the fillers were made by the machine shop of the UZH. The special Teflon holder was made by hand.
To calibrate the level meters several Teflon spacers were installed inside the capacitor in a distance of 1 cm. So if the xenon reaches this Teflon spacers, the readout should be constant. The capacitors were read out with *Labview* via an universal transducer interface (UTI). With this calibration we can translate the arbitrary units of *LabView* in a height. Figure 6.11 shows the calibration curve of level meter 3. Therefore a total mass of 9.96 kg xenon was pumped into the MarmotXL cryostat and cooled down. The producer for the two other level meters were the same and their calibration curve can be found in the appendix H.
The filling curve of level meter 3 (Figure 6.11) shows a step-wise increase of capacitance up to its maximum. Measurements points from the first increase indicate that the LXe level rises above the bottom copper ring of the level meter and the step up to the first

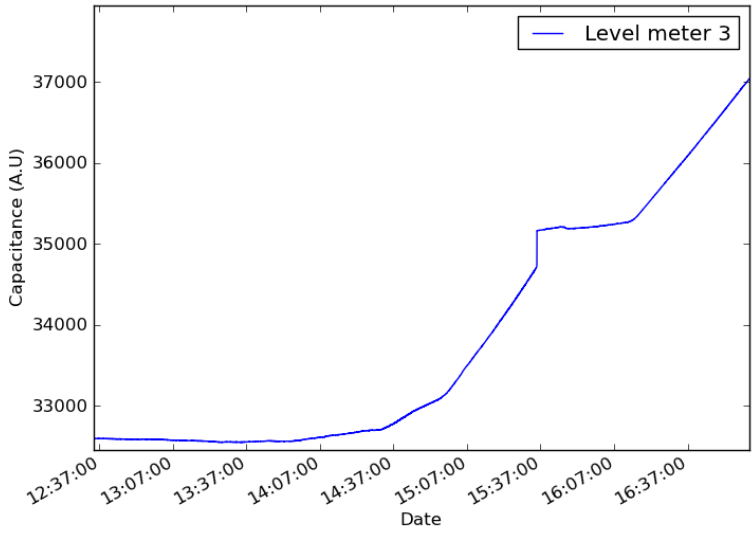


Figure 6.11.: The filling curve of the level meter 3. This curve is used to calibrate level meter 3. The step comes from the installed Teflon spacer inside the capacitor.

Table 6.2.: The calibration values for the three level meters. The change in Capacitance is measured from the calibration curves.

| Level Meter | change in Capacitance (A.U) | Capacitance change/cm height (A.U/cm) |
|---|---|---|
| \|LM1\| | 33900-32350=1550 | 1550 |
| \|LM2\| | 35700-33650=2050 | 2050 |
| \|LM3\| | 34700-33150=1550 | 1550 |

spacer be the distance between the copper ring and the first Teflon spacer. The horizontal step is the little Teflon spacer around the inner conductor which is 2.5 mm high. Table 6.2 shows the calibration result of all level meters.

### 6.3.2. Results

After the calibration we control the heater by hand and tried to get a stable liquid-gaseous xenon level. Stable operation was extremely difficult. Too much power for the heater leads to an empty bell, too less power leads to an full bell. We did manage to find a stable configuration to estimate the accuracy of the heater control. With 300 mW of power through the heater resistor over a period of about 1 hour, the liquid level stays within 1 cm. Figure 6.12 shows the readout of the three level meters with the turned on heater resistor.
The combination of the level meter design and UTI readout proved to be very unreliable. Sometimes the readout showed us useless data. The level meter got often in contact with the bell and a short circuit has been produced. This happened because it wasn't able to mount the level meters probably. This first design of the level meters were too unstable. A simpler plate capacitor and a readout using an LRC circuit analyser were designed in cooperation with the technical assistant to improve significantly the robustness and readout. The newly developed level meters can be found in the appendix.

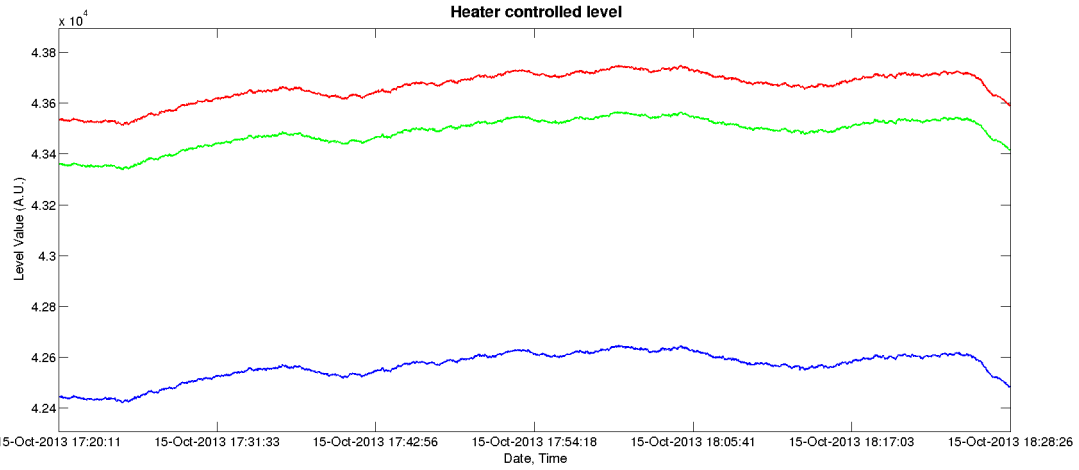


Figure 6.12.: The readout of the three level metes (green, blue and red) with the turned on heater resistor. The liquid level almost stayed constant.

# 7. Conclusion

The XENON1T experiment aims to detect directly dark matter via WIMP-nucleon scattering. The incoming WIMP leads to a nuclear recoil of the target material and produces an electronic and a nuclear recoil of the target material. The experiment uses a time projection chamber (TPC) to separate the ionization signal from the scintillation signal. The XENON1T experiment aims to reach a sensitivity of down to $2 \cdot 10^{-47} cm^2$ with 2 years of operation. The DARWIN project has the aim to build up a facility housing two multi-ton dual phase detectors to reach a sensitivity of down to $2 \cdot 10^{-48} cm^2$. An electrostatic simulation of the TPC is indispensable for the optimization of the electrostatic design and for the data analysis.

This thesis demonstrates that the simulation module *KEMField* (written by T.J Corona) is a very powerful tool to simulate large geometries as the DARWIN geometry.
We are able to calculate very big and complex geometries on fast parallelized computing platforms like GPUs or CPUs. Due to usage of the iterative Robin Hood methods as charge density solver, the memory consumption has been highly reduced. We saw that the commercial simulation software *COMSOL* Multiphysics needs a huge amount of memory, because of intrinsic properties of the finite element method. It will not be possible to simulate a detailed three dimensional model of DARWIN with *COMSOL*. With *KEMField* this will not be a problem. To be able to simulate the next generation of dual phase noble gas WIMP detector a new DARWIN module had been implemented into the *Kasper* simulation package within this thesis.

Also new shapes have been developed and implemented into the DARWIN module. The simulation module *KEMField* and the new DARWIN module were tested intensively. Therefore the XENON1T detector has been implemented into the DARWIN module. With this simulation we got the first non-axial symmetrical simulation of the XENON1T experiment, so that today exists a stable and reliable tool for electric field simulation for the DARWIN experiment or other dark matter experiments.

We also saw that the calculated electric field and electric potential in such a huge geometry, as the XENON1T geometry, has a measurable high numerical error. This was also observed in the simulations of the KATRIN experiment. Therefore new field calculations routines have been implemented into *KEMField*. This routines have a very low numerical error and are 5 times quicker than the old routines. A GPU implementation of this routines is necessary to speed up the calculation time and will be performed in the future.

Another focus in context of this master thesis was the hardware work for XENON1T. The

aim was to test a new kind of amplifier in connection with the XENON1T photomultiplier and to develop a new technique to stabilize the liquid-gaseous xenon interface in the XENON1T experiment. To control the liquid-gaseous-xenon interface with a heater was successful and should be investigated in the future with the newly developed level meters. The intensive amplifier PMT test showed that the new UZH amplifier is ready-to-use for the XENON1T experiment. The spectrum of this amplifier will be investigated in future.

The goal of the next measurement phase of the MarmotXL detector in Zürich is to build up a small TPC. With this TPC, the S2 signal extraction efficiency will be measured for several electric field configurations in order to determine the best extraction field for XENON1T. Also the possibility to use Avalanche-Photodiodes instead of photomultipliers will be investigated in future.

# Bibliography


[A+11a] J. Aleksic *et al.*, "Detection of very high energy gamma-ray emission from NGC 1275 by the MAGIC telescopes," 2011.

[A+11b] E. Aprile *et al.*, "Study of the electromagnetic background in the XENON100 experiment," *Phys.Rev.*, vol. D83, p. 082001, 2011.

[A+12a] R. Abbasi *et al.*, "Multi-year search for dark matter annihilations in the Sun with the AMANDA-II and IceCube detectors," *Phys.Rev.*, vol. D85, p. 042002, 2012.

[A+12b] M. Ackermann *et al.*, "The Fermi Large Area Telescope On Orbit: Event Classification, Instrument Response Functions, and Calibration," *Astrophys.J.Suppl.*, vol. 203, p. 4, 2012.

[A+12c] E. Aprile *et al.*, "Dark Matter Results from 225 Live Days of XENON100 Data," *Phys.Rev.Lett.*, vol. 109, p. 181301, 2012.

[A+13a] P. Ade *et al.*, "Planck 2013 results. XVI. Cosmological parameters," 2013.

[A+13b] O. Adriani *et al.*, "Cosmic-Ray Positron Energy Spectrum Measured by PAMELA," *Phys.Rev.Lett.*, vol. 111, no. 8, p. 081102, 2013.

[A+13c] D. Akerib *et al.*, "The Large Underground Xenon (LUX) Experiment," *Nucl.Instrum.Meth.*, vol. A704, pp. 111–126, 2013.

[A+13d] G. Ambrosi *et al.*, "The Cherenkov Telescope Array Large Size Telescope," 2013.

[A+14] E. Aprile *et al.*, "Analysis of the XENON100 Dark Matter Search Data," *Astropart.Phys.*, vol. 54, pp. 11–24, 2014.

[AGM+04] E. Aprile, K. L. Giboni, P. Majewski, K. X. Ni, and M. Yamashita, "Proportional light in a dual-phase XENON chamber," *Ieee Transactions On Nuclear Science*, vol. 51, pp. 1986–1990, 2004. [Online]. Available: http://dx.doi.org/10.1109/TNS.2004.832690

[Apr12] E. Aprile, "The XENON1T Dark Matter Search Experiment," 2012.

[B+05] R. Brunetti *et al.*, "Warp liquid argon detector for dark matter survey," *New Astron.Rev.*, vol. 49, pp. 265–269, 2005.

[B+13] C. Bennett *et al.*, "Nine-Year Wilkinson Microwave Anisotropy Probe (WMAP) Observations: Final Maps and Results," *Astrophys.J.Suppl.*, vol. 208, p. 20, 2013.

[Bar10] M. Bartelmann, "Gravitational Lensing," *Class.Quant.Grav.*, vol. 27, p. 233001, 2010.

[Bar13] A. Barnacka, "Detection techniques for the H.E.S.S. II telescope, data modeling of gravitational lensing and emission of blazars in HE-VHE astronomy," 2013.

[Bau12] L. Baudis, "DARWIN: dark matter WIMP search with noble liquids," *J.Phys.Conf.Ser.*, vol. 375, p. 012028, 2012.

[BBC+13] R. Bernabei, P. Belli, F. Cappella, V. Caracciolo, S. Castellano *et al.*, "Final model independent result of DAMA/LIBRA-phase1," *Eur.Phys.J.*, vol. C73, p. 2648, 2013.

[BBF+13] L. Baudis, A. Behrens, A. Ferella, A. Kish, T. Marrodan Undagoitia *et al.*, "Performance of the Hamamatsu R11410 Photomultiplier Tube in cryogenic Xenon Environments," *JINST*, vol. 8, p. P04026, 2013.

[BBS91] K. G. Begeman, A. H. Broeils, and R. H. Sanders, "Extended rotation curves of spiral galaxies - Dark haloes and modified dynamics," *mnras*, vol. 249, pp. 523–537, Apr. 1991.

[BCP+13] J. Buckley, D. Cowen, S. Profumo, A. Archer, M. Cahill-Rowley *et al.*, "Cosmic Frontier Indirect Dark Matter Detection Working Group Summary," 2013.

[Ber00] L. Bergstrom, "Nonbaryonic dark matter: Observational evidence and detection methods," *Rept.Prog.Phys.*, vol. 63, p. 793, 2000.

[BFA+11] L. Baudis, A. Ferella, A. Askin, J. Angle, E. Aprile *et al.*, "Gator: a low-background counting facility at the Gran Sasso Underground Laboratory," *JINST*, vol. 6, p. P08010, 2011.

[BFH10] Y. Bai, P. J. Fox, and R. Harnik, "The Tevatron at the Frontier of Dark Matter Direct Detection," *JHEP*, vol. 1012, p. 048, 2010.

[BH12] P. Barrow and D. Hilk, "Benchmark lines for electrostatic analysis of dual phase tpcs," 2012, internal Document.

[BHS05] G. Bertone, D. Hooper, and J. Silk, "Particle dark matter: Evidence, candidates and constraints," *Phys.Rept.*, vol. 405, pp. 279–390, 2005.

[Bil01] A. Bilal, "Introduction to Supersymmetry," *ArXiv High Energy Physics - Theory e-prints*, Jan. 2001.

[BR97] R. Brun and F. Rademakers, "{ROOT} — an object oriented data analysis framework," *Nuclear Instruments and Methods in Physics Research Section A: Accelerators, Spectrometers, Detectors and Associated Equipment*, vol. 389, no. 1–2, pp. 81 – 86, 1997, new Computing Techniques in Physics Research V. [Online]. Available: http://www.sciencedirect.com/science/article/pii/S016890029700048X

[BUB98] L. Bergström, P. Ullio, and J. H. Buckley, "Observability of $\gamma$ rays from dark matter neutralino annihilations in the milky way halo," *Astroparticle Physics*, vol. 9, no. 2, pp. 137–162, 1998.

[CBG+06] D. Clowe, M. Bradac, A. H. Gonzalez, M. Markevitch, S. W. Randall *et al.*, "A direct empirical proof of the existence of dark matter," *Astrophys.J.*, vol. 648, pp. L109–L113, 2006.

[cL07] T. X. collaboration/Rafael Lang, "2007 Hamamatsu Photonics K. K." 2007. [Online]. Available: http://www.hamamatsu.com/resources/pdf/etd/PMT_handbook_v3aE-Chapter2.pdf

[Col04] K. Collaboration, " KATRIN Design Report 2004," 2004. [Online]. Available: http://www-ik.fzk.de/~katrin/publications/documents/DesignReport2004-12Jan2005.pdf

[Col10] X. Collaboration, " XENON1T at LNGS Technical Design Report," 2010. [Online]. Available: http://www.bo.infn.it/xenon/docs/tdr2010.pdf

[col14] T. X. collaboration, "The XENON Detection Principle," 2014. [Online]. Available: http://www.physics.purdue.edu/darkmatters/xenon1t/

[COM14] L. COMPONENTS, "Photomultiplier – pmt," 2014. [Online]. Available: http://www.lasercomponents.com/de/news/einzelphotonenzaehlung-zwei-technologien-im-vergleich/

[Cor91] T. Corona, "Tools for electromagnetic field simulation in the katrin experiment," Master Thesis, Massachsetts institute of technology, 20091. [Online]. Available: http://opac.nebis.ch/ediss/20121322.pdf

[D+13] A. D.S. *et al.*, "First results from the LUX dark matter experiment at the Sanford Underground Research Facility," 2013.

[DHK+02] T. Doke, A. Hitachi, J. Kikuchi, K. Masuda, H. Okada, and E. Shibamura, "Absolute scintillation yields in liquid argon and xenon for various particles," *Japanese Journal of Applied Physics*, vol. 41, no. Part 1, No. 3A, pp. 1538–1545, 2002. [Online]. Available: http://jjap.jsap.jp/link?JJAP/41/1538/

[dS14] A. de Snaijer, "Conteptional illustration," 2014, internal wiki. [Online]. Available: http://www.physik.uzh.ch/groups/groupbaudis/xenon/atpwiki/doku.php

[Dun85] D. A. Dunavant, "High degree efficient symmetrical gaussian quadrature rules for the triangle," *International Journal for Numerical Methods in Engineering*, vol. 21, no. 6, pp. 1129–1148, 1985. [Online]. Available: http://dx.doi.org/10.1002/nme.1620210612

[Dur11] R. Durrer, "What do we really know about Dark Energy?" *Phil.Trans.Roy.Soc.Lond.*, vol. A369, pp. 5102–5114, 2011.

[E+12] A. E. *et al.*, "The XENON100 Dark Matter Experiment," *Astropart.Phys.*, vol. 35, pp. 573–590, 2012.

[ea13] W. S. et al., "The visualization toolkit," 2013, 3rd Edition Kitware.

[F+98] Y. Fukuda *et al.*, "Evidence for oscillation of atmospheric neutrinos," *Phys.Rev.Lett.*, vol. 81, pp. 1562–1567, 1998.

[FAL93] J. Fetzer, S. Abele, and G. Lehner, "Die kopplung der randelementmethode und der methode der finiten elemente zur lösung dreidimensionaler elektromagnetischer feldprobleme auf unendlichem grundgebiet," *Archiv für Elektrotechnik*, vol. 76, no. 5, pp. 361–368, 1993.

[FHKT12] P. J. Fox, R. Harnik, J. Kopp, and Y. Tsai, "Missing Energy Signatures of Dark Matter at the LHC," *Phys.Rev.*, vol. D85, p. 056011, 2012.

[FLC+11] J. Formaggio, P. Lazic, T. Corona, H. Stefancic, H. Abraham *et al.*, "Solving for Micro- and Macro- Scale Electrostatic Configurations Using the Robin Hood Algorithm," 2011.

[For93] T. M. Forum, "Mpi: A message passing interface," 1993. [Online]. Available: http://www.mpi-forum.org/

[GAC+11] K. L. Giboni, E. Aprile, B. Choi, T. Haruyama, R. F. Lang, K. E. Lim, A. J. Melgarejo, and G. Plante, "Xenon recirculation-purification with a heat exchanger," *Journal of Instrumentation*, vol. 6, p. 3002, Mar. 2011.

[GBG+00] M. Girardi, S. Borgani, G. Giuricin, F. Mardirossian, and M. Mezzetti, "Optical luminosities and mass-to-light ratios of nearby galaxy clusters," *Astrophys.J.*, vol. 530, p. 62, 2000.

[Glu07] F. Glueck, "The electric shielding factor of the wire electrode," 2007, internal KATRIN paper.

[Gri07] D. Griffiths, *Introduction to Electrodynamics*. Pearson Education, 2007.

[Gro] K. S. Group, "Kassiopeia: A modern extensible c++ particle tracking package," paper in preparation.

[Gro14] T. L. B. Group, "Marmotxl wiki," 2014, internal wiki. [Online]. Available: http://www.physik.uzh.ch/groups/groupbaudis/xenon/atpwiki/doku.php?id=marmotx

[GW85] M. W. Goodman and E. Witten, "Detectability of certain dark-matter candidates," *Phys. Rev. D*, vol. 31, pp. 3059–3063, Jun 1985. [Online]. Available: http://link.aps.org/doi/10.1103/PhysRevD.31.3059

[H.14] M. H., "The Virial Theorem," 2014. [Online]. Available: http://www.astro.cornell.edu/academics/courses/astro201/vt.htm

[Hen07] A. Henderson, "The visualization toolkit - a parallel visualization application," 2007, kitware Inc.

[Hit05] A. Hitachi, "Properties of liquid xenon scintillation for dark matter searches," *Astropart.Phys.*, vol. 24, pp. 247–256, 2005.

[HTF+83] A. Hitachi, T. Takahashi, N. Funayama, K. Masuda, J. Kikuchi, and T. Doke, "Effect of ionization density on the time dependence of luminescence from liquid argon and xenon," *Phys. Rev. B*, vol. 27, pp. 5279–5285, May 1983. [Online]. Available: http://link.aps.org/doi/10.1103/PhysRevB.27.5279

[ILS14] A. Ibarra, A. S. Lamperstorfer, and J. Silk, "Dark matter annihilations and decays after the AMS-02 positron measurements," *Phys.Rev.*, vol. D89, p. 063539, 2014.

[Jam14] A. James, "Xenon1t illustration, pictures and photos of marmotxl," 2014, internal wiki. [Online]. Available: http://www.physik.uzh.ch/groups/groupbaudis/xenon/atpwiki/

[JKG96] G. Jungman, M. Kamionkowski, and K. Griest, "Supersymmetric dark matter," *Phys.Rept.*, vol. 267, pp. 195–373, 1996.

[Kah65] W. Kahan, "Pracniques: Further remarks on reducing truncation errors," *Commun. ACM*, vol. 8, no. 1, pp. 40–, Jan. 1965. [Online]. Available: http://doi.acm.org/10.1145/363707.363723

[Kis11] A. Kish, "Dark matter search with the xenon100 experiment," Dissertation, University of Zurich, 2011. [Online]. Available: http://opac.nebis.ch/ediss/20121322.pdf

[KW11] R. Kappl and M. W. Winkler, "New Limits on Dark Matter from Super-Kamiokande," *Nucl.Phys.*, vol. B850, pp. 505–521, 2011.

[LAB+12] K. Lung, K. Arisaka, A. Bargetzi, P. Beltrame, A. Cahill *et al.*, "Characterization of the Hamamatsu R11410-10 3-Inch Photomultiplier Tube for Liquid Xenon Dark Matter Direct Detection Experiments," *Nucl.Instrum.Meth.*, vol. A696, pp. 32–39, 2012.

[Lah07] A. Lahanas, "LSP as a Candidate for Dark Matter," *Lect.Notes Phys.*, vol. 720, pp. 35–68, 2007.

[Lei09] B. Leiber, "Non-axially symmetric field and trajectory calculations for the KATRIN-experiment ," 2009. [Online]. Available: https://www.katrin.kit.edu/publikationen/dth-leiber.pdf

[LvA06] P. Lazić, H. Štefančić, and H. Abraham, "The Robin Hood method – A novel numerical method for electrostatic problems based on a non-local charge transfer," *Journal of Computational Physics*, vol. 213, no. 1, pp. 117–140, Mar. 2006. [Online]. Available: http://dx.doi.org/10.1016/j.jcp.2005.08.006

[M+11] A. Marchionni *et al.*, "ArDM: a ton-scale LAr detector for direct Dark Matter searches," *J.Phys.Conf.Ser.*, vol. 308, p. 012006, 2011.

[NAS13] NASA, "NASA Images," 2013. [Online]. Available: http://www.nasa.gov/multimedia/imagegallery/

[Oli03] K. A. Olive, "TASI lectures on dark matter," pp. 797–851, 2003.

[OW08] E. Otten and C. Weinheimer, "Neutrino mass limit from tritium beta decay," *Rept.Prog.Phys.*, vol. 71, p. 086201, 2008.

[PRSZ09] B. Povh, K. Rith, C. Scholz, and F. Zetsche, "Teilchen und kerne," *Teilchen und Kerne: Eine Einführung in die physikalischen Konzepte, Springer-Lehrbuch. ISBN 978-3-540-68075-8. Springer Berlin Heidelberg, 2009*, vol. 1, 2009.

[RF70] V. C. Rubin and W. K. Ford, Jr., "Rotation of the Andromeda Nebula from a Spectroscopic Survey of Emission Regions," *apj*, vol. 159, p. 379, Feb. 1970.

[RM14] G. R and Mandic, "Dark Matter Limit Plot Generator," 2014. [Online]. Available: http://dendera.berkeley.edu/plotter/entryform.html

[Sci14] P. Scientific, "16 channel photomultiplier preamplifier," 2014. [Online]. Available: http://www.phillipsscientific.com/pdf/776ds.pdf

[SGG03] J. Schöberl, J. Gerstmayr, and R. Gaisbauer, "NETGEN - automatic 3d tetrahedral mesh generator." http://www.hpfem.jku.at/netgen/, Austrian Science Fund FWF ( Special Research Project "Numerical and Symbolic Scientific Computing", Start Project "hp-FEM"), May 2003. [Online]. Available: http://www.hpfem.jku.at/netgen/

[Smo99] G. F. Smoot, "COBE observations and results," *AIP Conf.Proc.*, vol. 476, pp. 1–10, 1999.

[Sta14] J. Stammen, "Numerische feldberechnung mit der finite-elemente-methode," 2014, presentation. [Online]. Available: http://www.ets.uni-duisburg-essen.de/stammen/Einfuehrung-FEM.pps

[YDK+04] M. Yamashita, T. Doke, K. Kawasaki, J. Kikuchi, and S. Suzuki, "Scintillation response of liquid xe surrounded by {PTFE} reflector for gamma rays," *Nuclear Instruments and Methods in Physics Research Section A: Accelerators, Spectrometers, Detectors and Associated Equipment*, vol. 535, no. 3, pp. 692 – 698, 2004. [Online]. Available: http://www.sciencedirect.com/science/article/pii/S0168900204016638

[Zwi33] F. Zwicky, "Die Rotverschiebung von extragalaktischen Nebeln," *Helv.Phys.Acta*, vol. 6, pp. 110–127, 1933.

# Appendix

## A. Geometry Test Model

Figure A.1 shows a sketch of the geometry used for calculations in section 4.2.2. Figure A.2 shows the implemented 3D model of the sketch.

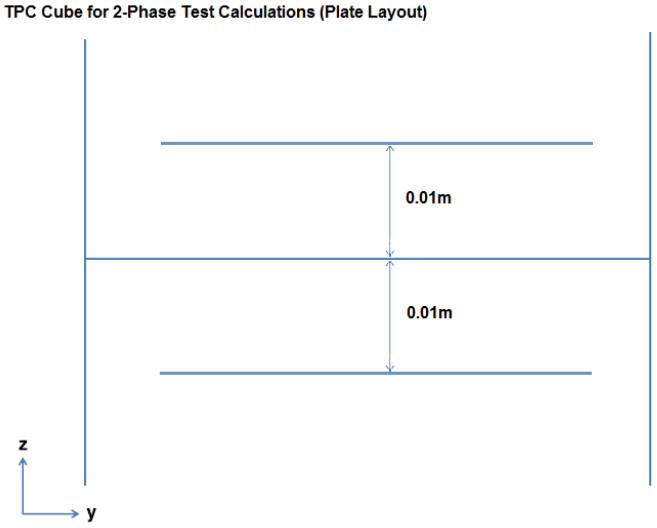


Figure A.1.: 2-D cross section of the plate capacitor.

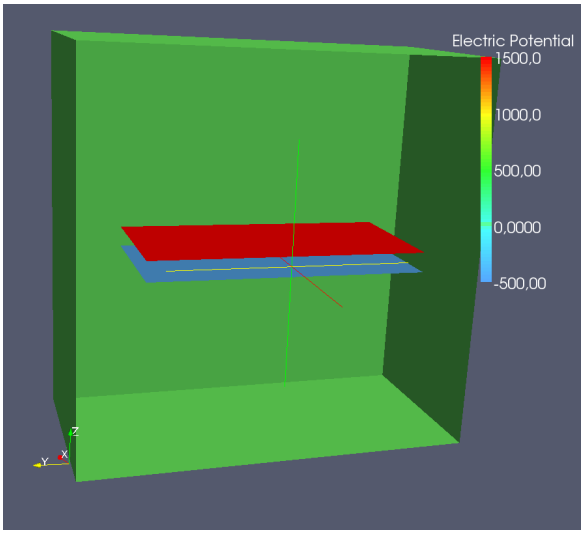


Figure A.2.: The 3D model of the zero potential box and the plate capacitor. The colors represent the value of the potential. The red coloured area represents a high potential and the green/blue coloured area represents a low potential.

Figure A.3 shows a sketch of the geometry used for calculations in section 4.2.3. Figure A.4 shows the implemented 3D model of the sketch.

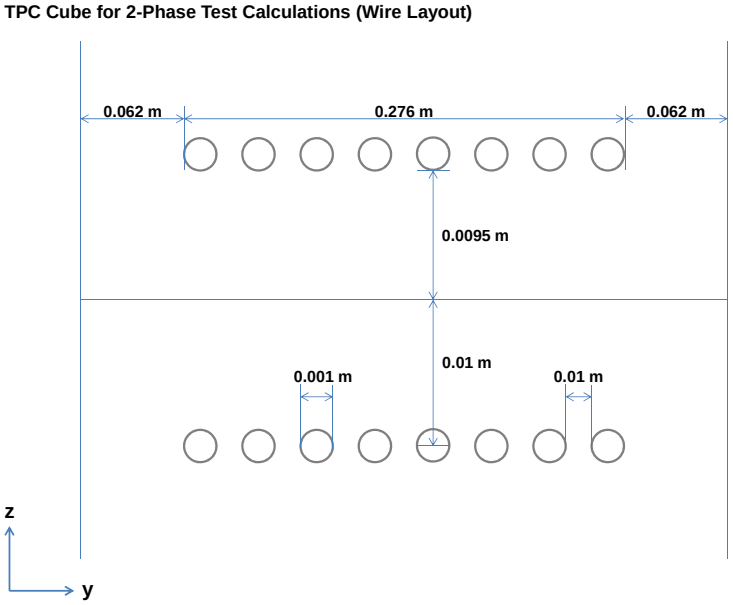


Figure A.3.: 2-D cross section of the wire capacitor. Not all wires are drawn.

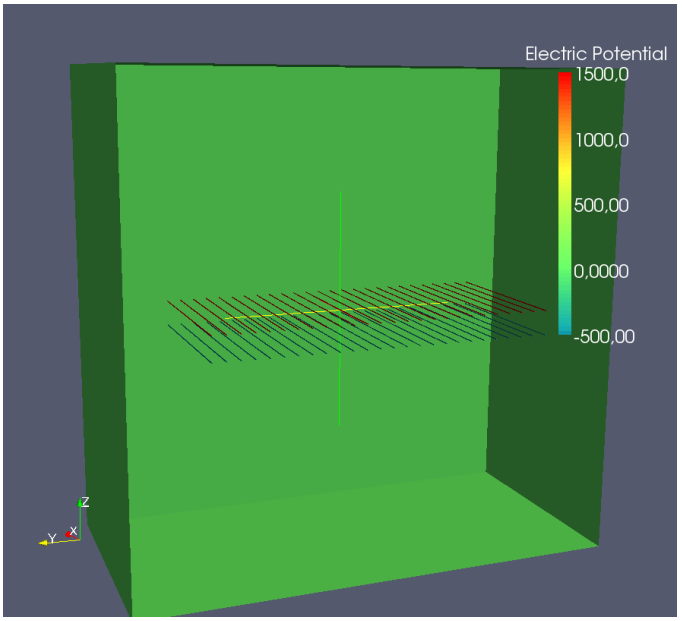


Figure A.4.: The three dimensional model of the zero potential box and the wire capacitor. The box was cut through the yz-plane. The wire capacitor is placed in the center of the box. The colors represent the value of the potential

# B. Results Test Model

Figure B.5 shows the electric potential of the calculated plate capacitor in section 4.2.2. Figure A.2 shows the electric potential of the calculated wire capacitor in section 4.2.3.

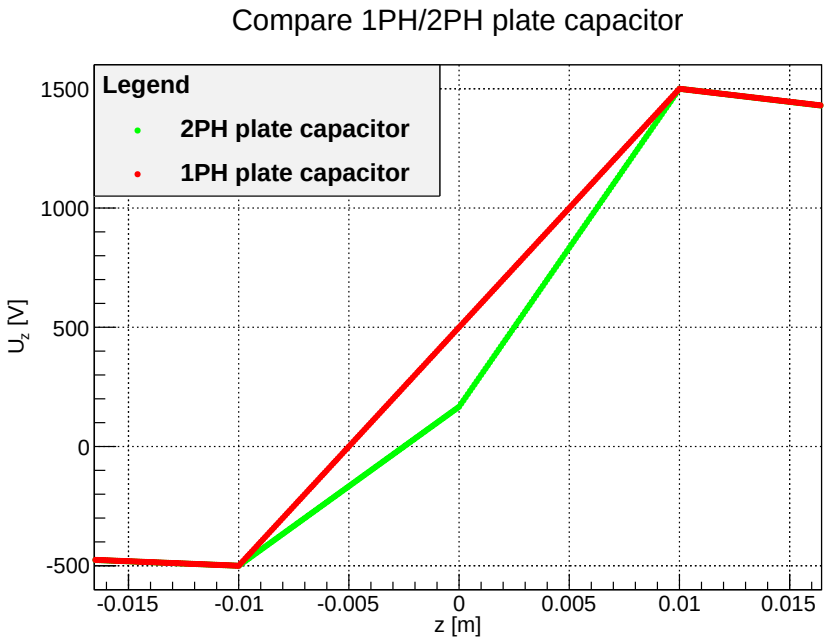


Figure B.5.: The electric potential in vacuum and in liquid/gaseous xenon. The red points are in vacuum and the green points are in liquid/gaseous xenon.

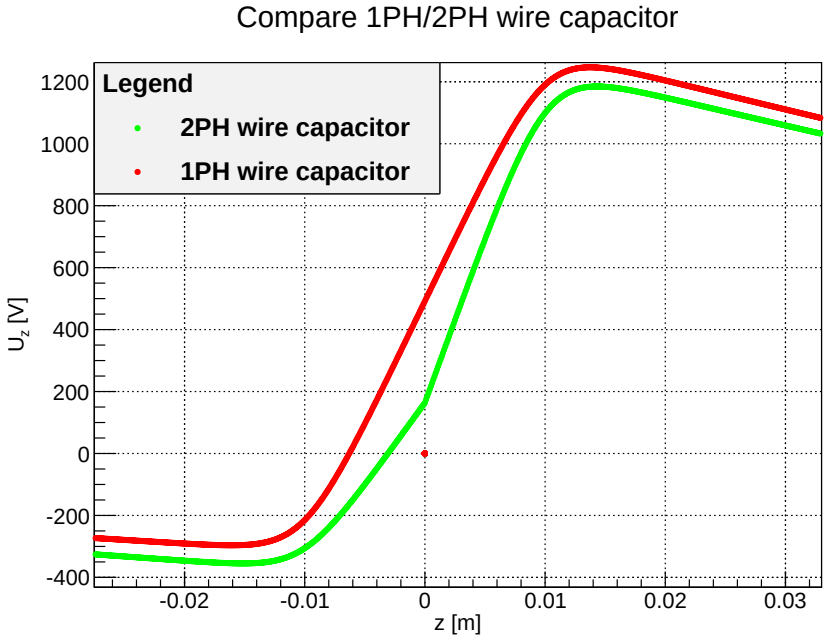


Figure B.6.: The electric potential in vacuum and in liquid/gaseous xenon for a wire capacitor. The red points are in vacuum and the green points are in liquid/gaseous xenon.

Figure B.7 shows the relative error of the simulated plate capacitor in vaccum and figure B.8 shows the relative error of the simulated plate capacitor with dielectrics. For the simulation *KEMField* and *COMSOL* is used.

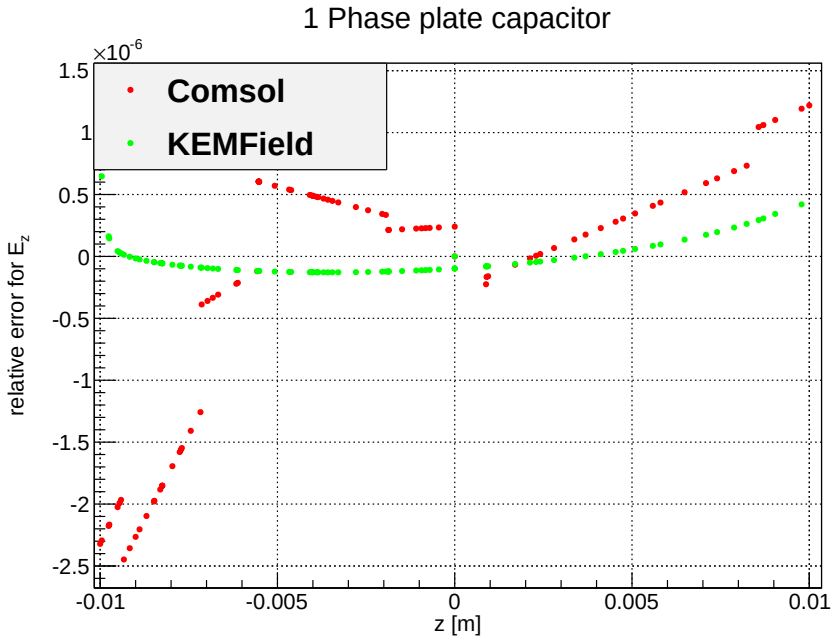


Figure B.7.: The relative error $f$ for the vacuum plate capacitor. The red points are the relative error for *COMSOL*. The green points are the relative error for *KEMField*.

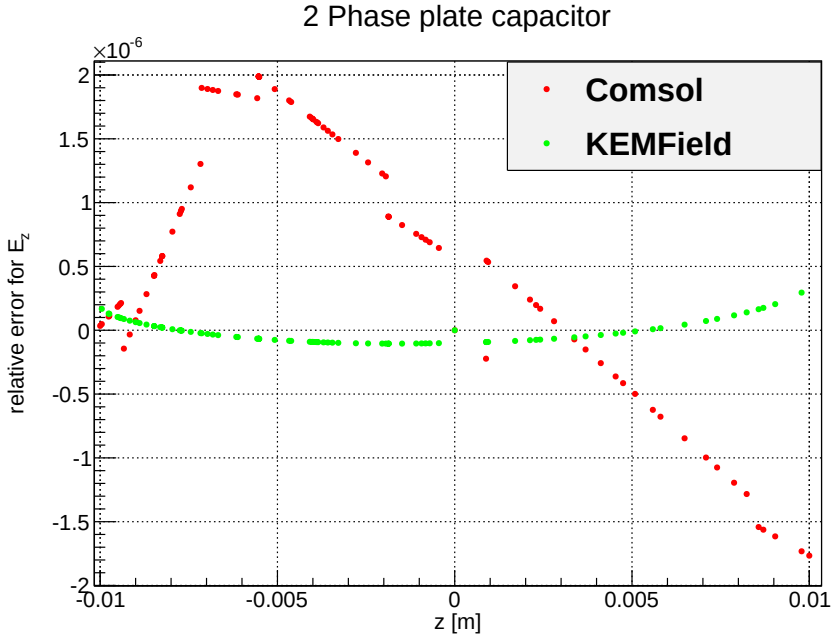


Figure B.8.: The relative error $f$ for the dual phase plate capacitor. The red points are the relative error for *COMSOL*. The green points are the relative error for *KEMField*.

Figure B.9 shows the difference between *COMSOL* and *KEMField* of the simulated wire capacitor in vaccum and figure B.10 shows the difference between *COMSOL* and *KEMField* of the simulated wire capacitor in dielectrics.

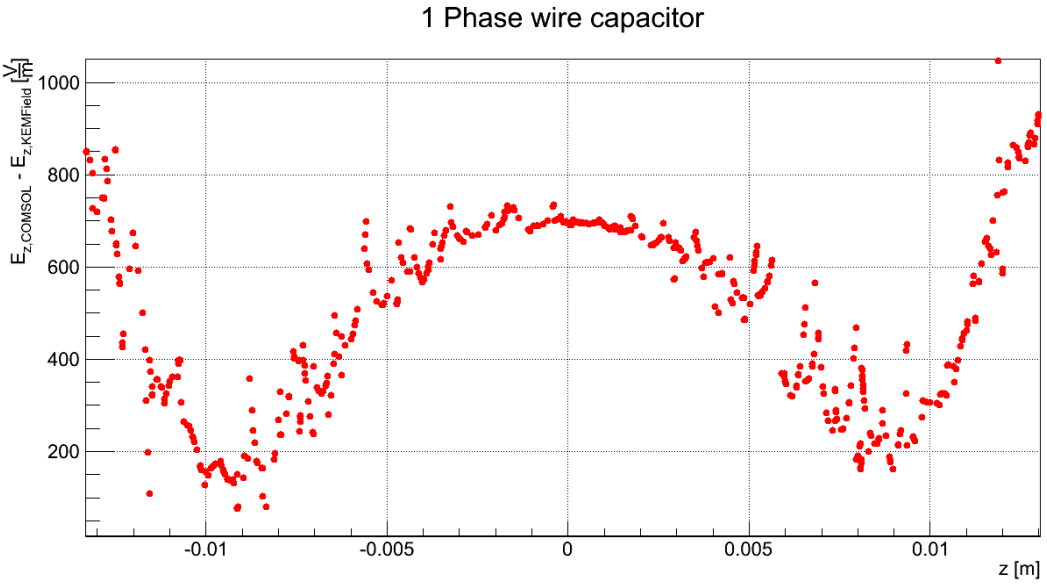


Figure B.9.: The difference between *COMSOL* and *KEMField* for a wire capacitor in vacuum. The red points are the absolute value of the difference between *COMSOL* and *KEMField*.

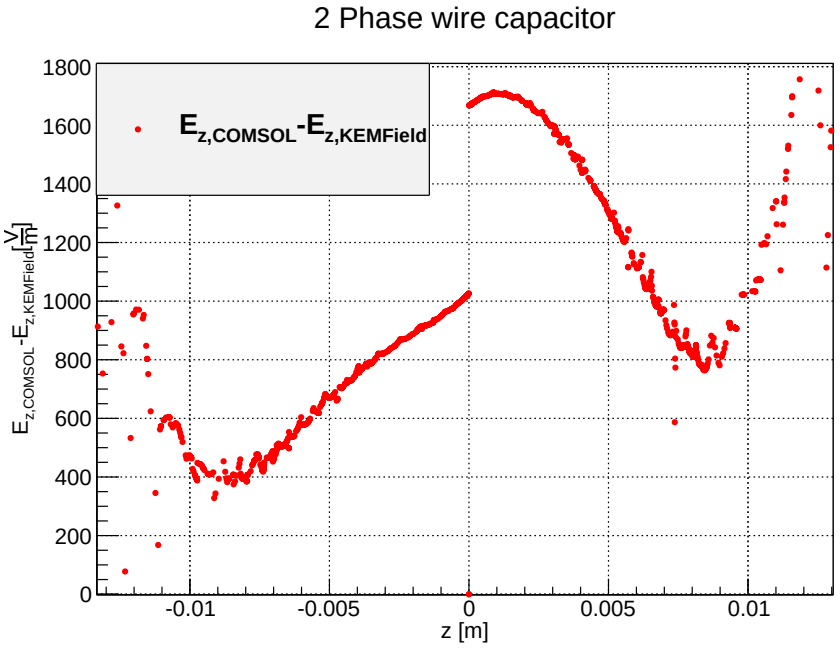


Figure B.10.: The difference between *COMSOL* and *KEMField* for a dual phase wire capacitor. The red points are the absolute value of the difference between *COMSOL* and *KEMField*.

Figure B.11 shows the electric field between two parallel wires simulated in section 4.2.4. Figure B shows the electric field between a zero potential plate and a wire grid simulated in 4.2.5.

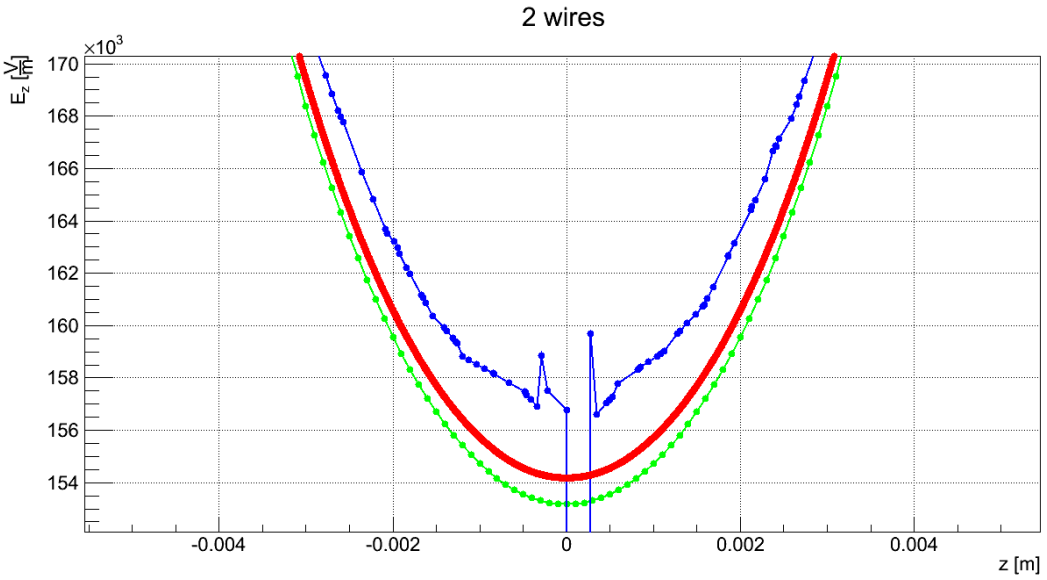


Figure B.11.: The electric field for 2 parallel wires. The *COMSOL* discretization is coarse. The red points are the analytical solution. The green points are the solution of *KEMField* and the blue points are the solution of *COMSOL*.

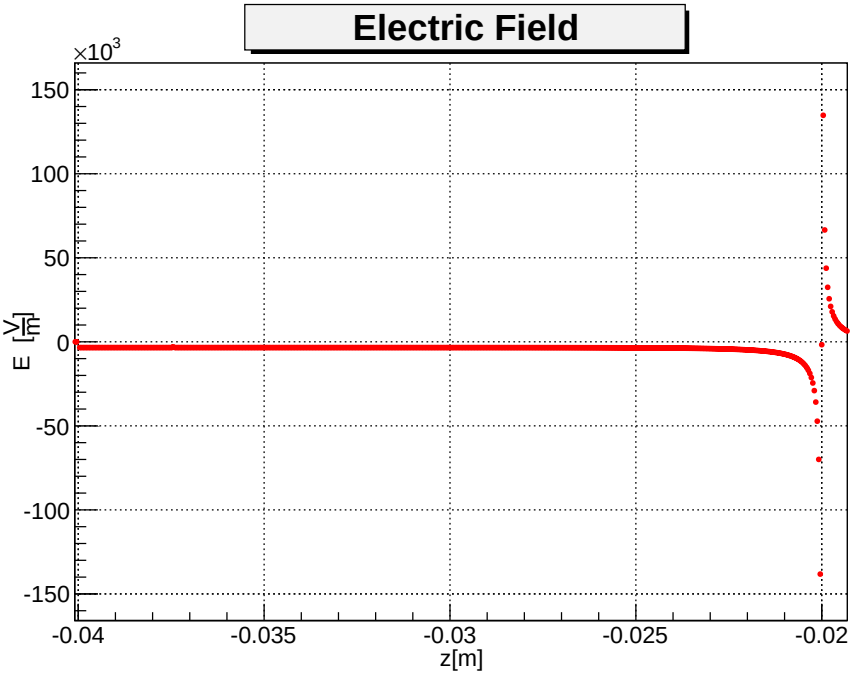


Figure B.12.: The electric field along the z-Axis from the plate to the wire grid.

# C. DGeobag Code

Listing 7.1 shows the code for modelling the XENON1T geometry, the simulation results are shown in chapter 5.3.

```
...
DGTank* vessel = new DGTank();
vessel->SetName("vessel");

//Bot-PMT-Array
DGPMT* BotPMT = new DGPMT();
BotPMT->SetName("BotPMT");
BotPMT->SetZ1(-0.124);
BotPMT->SetZ2(-0.010);
BotPMT->SetR(0.49085);

//Teflon reflector of the bot PMT array
KGCADImport* CADImportPMTReflectorBot = new KGCADImport();
CADImportPMTReflector->SetName("CADImportPMTReflector");
CADImportPMTReflector->SetInputFile("PMT_Reflector_Bot.stl");
CADImportPMTReflector->SetVerbose(0);

//Bot-PMT-ProtectionGrid-holder
DGHolderProtection* ProtectionGridHolderBot = new DGHolderProtection();
ProtectionGridHolderBot->SetName("ProtectionGridHolderBot");
ProtectionGridHolderBot->SetZ1(-0.006);
ProtectionGridHolderBot->SetZ2(-0.001);
ProtectionGridHolderBot->SetR1(0.472);
ProtectionGridHolderBot->SetR2(0.480);

//Bot-PMT-ProtectionGrid
KGWireMesh* BotPMTprotectionGrid = new KGWireMesh();
BotPMTprotectionGrid->SetName("BotPMTprotectionGrid");
BotPMTprotectionGrid->SetZ(-0.0005);
BotPMTprotectionGrid->SetWiresDiameter(0.000125);
BotPMTprotectionGrid->SetCylinderDiameter(0.944);
BotPMTprotectionGrid->SetPitch(0.00475);

//Teflon reflector bot
DGTeflonWallBot* Teflon_Boundary_Rings_Bot_PMT= new DGTeflonWallBot();
Teflon_Boundary_Rings_Bot_PMT->SetName("Teflon_Boundary_Rings_Bot_PMT");

//Cathode-holder
DGCathodeHolder* BotCathodeHolder = new DGCathodeHolder();
BotHolder->SetName("BotHolder");

//Cathode
KGWireMesh* cathode = new KGWireMesh();
cathode->SetName("cathode");
cathode->SetZ(0.0705);
cathode->SetWiresDiameter(0.000125);
cathode->SetPitch(0.00485);
cathode->SetCylinderDiameter(0.974);

//Import of the cathode power supply
KGCADImport* CADImportCathode = new KGCADImport();
CADImportCathode->SetName("CADImportCathode");
CADImportCathode->SetInputFile("Power_supply.stl");
CADImportCathode->SetVerbose(0);

//Import of the cathode isolation
KGCADImport* CADImportPMTTeflon= new KGCADImport();
CADImportPMTTeflon->SetName("CADImportPMTTeflon");
CADImportPMTTeflon->SetInputFile("Cathode_isolation.stl");
CADImportPMTTeflon->SetVerbose(0);

//76-Ring_electrodes
std::vector<DGRingElectrode*> fRingElectrode;
Double_t Z1(0.0839);
Double_t Z2(0.0889);
Double_t R1(0.4875);
Double_t R2(0.4925);
Double_t space(0.013);
Int_t Number = 76;
for(int i=0;i<Number;i++){
stringstream ss;
ss << i;
string str = ss.str();
fRingElectrode.push_back( new DGRingElectrode() );
fRingElectrode[i]->SetName("Ringelectrode_number: "+str);
fRingElectrode[i]->SetZ1(Z1);
fRingElectrode[i]->SetZ2(Z2);
fRingElectrode[i]->SetR1(R1);
fRingElectrode[i]->SetR2(R2);
Z1= Z1+space;
Z2= Z2+space;
}
//Teflon reflector of the field shaping rings
DGTeflonWall* Teflon_Boundary_Rings = new DGTeflonWall();
Teflon_Boundary_Rings->SetName("Teflon_Boundary_Rings");

//Gate
KGWireMesh* Gate = new KGWireMesh();
Gate->SetName("cathode");
Gate->SetZ(1.05345);
Gate->SetWiresDiameter(0.000125);
Gate->SetPitch(0.0023);
Gate->SetCylinderDiameter(0.973);

```

```
95  //Gate-Holder
96  DGLRingGate* GateHolder = new DGLRingGate();
97  GateHolder ->SetName( "GateHolder" );
98
99  //Boundary liquid-gaseous xenon
100 KGDisk* xenon_boundary_1 = new KGDisk();
101 xenon_boundary ->SetName( "xenon_boundary" );
102 xenon_boundary ->SetZ(1.05595);
103 xenon_boundary ->SetR(0.5155);
104 xenon_boundary -> SetAxialMeshCount(200);
105 xenon_boundary -> SetRadialMeshCount(300);
106 xenon_boundary -> SetRadialMeshPower(1);
107
108 //Boundary liquid-gaseous xenon
109 KGAnnulus* xenon_boundary_2 = new KGAnnulus();
110 xenon_boundary_2 ->SetName( "Top_PMT" );
111 xenon_boundary_2 ->SetZ(1.05595);
112 xenon_boundary_2 ->SetR1( 0.5215);
113 xenon_boundary_2 ->SetR2( 0.550 );
114 xenon_boundary_2  ->SetAxialMeshCount(200);
115 xenon_boundary_2  ->SetRadialMeshCount(50);
116 xenon_boundary_2  ->SetRadialMeshPower(2);
117
118 //Anode-Holder
119 DGLRingAnode* AnodeHolder = new DGLRingAnode();
120 AnodeHolder ->SetName( "AnodeHolder " );
121
122 //Anode
123 KGWireMesh* Anode= new KGWireMesh();
124 Anode->SetName( "cathode " );
125 Anode->SetZ(1.05845);
126 Anode->SetWiresDiameter( 0.000125 );
127 Anode->SetPitch(0.0023);
128 Anode->SetCylinderDiameter(0.961);
129
130 //Teflon reflector of the top PMT array
131 KGCADImport* CADImportPMTReflectorTop = new KGCADImport();
132 CADImportPMTReflectorTop ->SetName("CADImportPMTReflectorTop ");
133 CADImportPMTReflectorTop ->SetInputFile("PMT_Reflector_Top.stl");
134 CADImportPMTReflectorTop ->SetVerbose(0);
135
136 //Top-PMT-Array
137 DGPMT* TopPMT = new DGPMT();
138 TopPMT ->SetName( "TopPMT " );
139 TopPMT ->SetZ1(1.1274);
140 TopPMT ->SetZ2(1.2414);
141 TopPMT ->SetR(0.522);
142
143 //Top PMT Protection grid
144 KGWireMesh* PMTProtectionGridTop = new KGWireMesh();
145 PMTProtectionGridTop ->SetName( "PMTProtectionGridTop " );
146 PMTProtectionGridTop ->SetZ(1.118 );
147 PMTProtectionGridTop ->SetWiresDiameter( 0.000125 );
148 PMTProtectionGridTop ->SetPitch(0.00485);
149 PMTProtectionGridTop ->SetCylinderDiameter(1.044);
150
151 ...
```

Listing 7.1: The implemented code for modelling the Xenon1T geometry. All the objects of the different parts will be created.

Listing 7.2 shows the code for DGeoBag to discretize a disc with triangles.

```
...
  for(int j=1; j<=AxialMeshCount ; j++){

    //First triangle of one arc
    th = ((double)(j  % AxialMeshCount))/AxialMeshCount *2.*M_PI;

    p0[0]=(tRadii[1])*sin(th_last);
    p0[1]=(tRadii[1])*cos(th_last);

    p1[0]=(tRadii[1])*sin(th);
    p1[1]=(tRadii[1])*cos(th);

    p2[0]=0;
    p2[1]=0;
    p2[2]=p1[2]=p0[2]=z;

    AddElement(CreatTriangle(p2,p1,p0));

  //rest of the arc. Every trapezoid gets divided into two triangles
    for(int i=0; i<(RadialMeshCount-1); i++){

        p0[0]= sin(th_last)*(tRadii[i+1]);
        p0[1]= cos(th_last)*(tRadii[i+1]);

        p3[0]= sin(th_last)*(tRadii[i+2]);
        p3[1]= cos(th_last)*(tRadii[i+2]);

        p1[0]= sin(th)*(tRadii[i+1]);
        p1[1]= cos(th)*(tRadii[i+1]);

        p2[0]= sin(th)*(tRadii[i+2]);
        p2[1]= cos(th)*(tRadii[i+2]);

        p2[2]=p1[2]=p0[2]=p3[2]=z;

        AddElement(CreatTriangle(p0,p1,p3));
        AddElement(CreatTriangle(p1,p2,p3));

     }
     th_last = th;

  }
...
```

Listing 7.2: Discretization code for a disc in DGeoBag.

Listing 7.3 shows the code in DGeoBag to discretize a annulus with triangles.

```
for(int j=0; j<AxialMeshCount; j++){

//every trapez get divided into 2 triangles
  for(int i=0; i<RadialMeshCount; i++){


    //first triangles of the trapez
    double first_point_x = sin((j*disc_angel)*PI/180)*(tRadii[i]);
    double first_point_y = cos((j*disc_angel)*PI/180)*(tRadii[i]);

    double second_point_x = sin(((j+1)*disc_angel)*PI/180)*(tRadii[i]);
    double second_point_y = cos(((j+1)*disc_angel)*PI/180)*(tRadii[i]);

    double third_point_x = sin(((j+1)*disc_angel)*PI/180)*(tRadii[i+1]);
    double third_point_y = cos(((j+1)*disc_angel)*PI/180)*(tRadii[i+1]);

    KThreeVector v1(first_point_x,first_point_y, first_point_z);
    KThreeVector v2(second_point_x,second_point_y,second_point_z);
    KThreeVector v3(third_point_x,third_point_y,third_point_z);

    KThreeVector fN1 = v2-v1;
    KThreeVector fN2 = v3-v1;
    double fA = fN1.Magnitude();
    double fB = fN2.Magnitude();
    fN1 = fN1.Unit();
    fN2 = fN2.Unit();
    double fN3 = fN1.GetX()*fN2.GetY()- fN1.GetY()*fN2.GetX();
    if(fN3>0){
      KGMeshTriangle* r =  new KGMeshTriangle(v1, v2, v3);
      AddElement(r);

    }
    else{
      KGMeshTriangle* r =  new KGMeshTriangle(v1, v3, v2);
      AddElement(r);
    }
  }

  for(int i=0; i<RadialMeshCount; i++){
    //second triangles of the trapez
    double first_point_x = sin((j*disc_angel)*PI/180)*(tRadii[i]);
    double first_point_y = cos((j*disc_angel)*PI/180)*(tRadii[i]);

    double second_point_x = sin((j*disc_angel)*PI/180)*(tRadii[i+1]);
    double second_point_y = cos((j*disc_angel)*PI/180)*(tRadii[i+1]);

    double third_point_x = sin((j+1)*disc_angel*PI/180)*(tRadii[i+1]);
    double third_point_y = cos((j+1)*disc_angel*PI/180)*(tRadii[i+1]);


    KThreeVector v1(first_point_x,first_point_y, first_point_z);
    KThreeVector v2(second_point_x,second_point_y,second_point_z);
    KThreeVector v3(third_point_x,third_point_y,third_point_z);
      KThreeVector fN1 = v2-v1;
    KThreeVector fN2 = v3-v1;
    double fA = fN1.Magnitude();
    double fB = fN2.Magnitude();
    fN1 = fN1.Unit();
    fN2 = fN2.Unit();
    double fN3 = fN1.GetX()*fN2.GetY()- fN1.GetY()*fN2.GetX();
    if(fN3>0){
      KGMeshTriangle* r =  new KGMeshTriangle(v1, v2, v3);
      AddElement(r);

    }
    else{
      KGMeshTriangle* r =  new KGMeshTriangle(v1, v3, v2);
      AddElement(r);
    }

   }
  }
```

Listing 7.3: Discretization code for an annulus in DGeoBag

Listing 7.4 shows the code in DGeoBag to discretize a wire mesh with wires.

```
...
      double first_x = sqrt((realr*realr)-(pitch_half*pitch_half));
      double first_test = sqrt(((realr-0.1)*(realr-0.1))-(pitch_half*pitch_half));

      KThreeVector tmp_e(-first_x,pitch_half,z);
      KThreeVector tmp_z(-first_test,pitch_half,z);
      KThreeVector tmp_y(first_test,pitch_half,z);
      KThreeVector tmp_f(first_x,pitch_half,z);

      KThreeVector tmp_g(-first_x,-pitch_half,z);
      KThreeVector tmp_x(-first_test,-pitch_half,z);
      KThreeVector tmp_w(first_test,-pitch_half,z);
      KThreeVector tmp_h(first_x,-pitch_half,z);

    //one wire gets divided into 3 wires to change the discretization along the wire
      KGMeshWire* meshwire_first_plus = new KGMeshWire(tmp_e,tmp_z,wire->GetWiresDiameter());
      KGMeshWire* meshwire_first_plus2 = new KGMeshWire(tmp_z,tmp_y,wire->GetWiresDiameter());
      KGMeshWire* meshwire_first_plus3 = new KGMeshWire(tmp_y,tmp_f,wire->GetWiresDiameter());

      KGMeshWire* meshwire_first_minus1 = new KGMeshWire(tmp_g,tmp_x,wire->GetWiresDiameter());
    KGMeshWire* meshwire_first_minus2 = new KGMeshWire(tmp_x,tmp_w,wire->GetWiresDiameter());
    KGMeshWire* meshwire_first_minus3 = new KGMeshWire(tmp_w,tmp_h,wire->GetWiresDiameter());

    meshcount_ends    =(0.1)/(0.00475);  //Discretization at the edges of the wire
    meshcount_middle =int(((first_x+first_x)-0.2)/(0.01));
    meshcount_middle =int(meshcount_middle);

    RefineAndAddElement(meshwire_first_plus,meshcount_ends,1);
      RefineAndAddElement(meshwire_first_plus2,meshcount_middle,1);
      RefineAndAddElement(meshwire_first_plus3,meshcount_ends,1);

      RefineAndAddElement(meshwire_first_minus1,meshcount_ends,1);
      RefineAndAddElement(meshwire_first_minus2,meshcount_middle,1);
      RefineAndAddElement(meshwire_first_minus3,meshcount_ends,1);


      double tmp(0);
      tmp= pitch_half+pitch;
      for(int i=0; i<Number-1;i++){
        double tmp1(0);
        tmp1 = sqrt((realr*realr)-(tmp*tmp));
        double test= sqrt((realr-0.1)*(realr-0.1)-(tmp*tmp));


        if(tmp<(realr-0.1)){
             int meshcount_ends=(0.1)/(0.00475);
        int meshcount_middle=((tmp1+tmp1)-0.2)/((0.01));

        KThreeVector tmp_a(tmp1,tmp,z);
        KThreeVector tmp_b(test,tmp,z);
        KThreeVector tmp_x(-test,tmp,z);
        KThreeVector tmp_y(-tmp1,tmp,z);
        KGMeshWire* meshwire1 = new KGMeshWire(tmp_a,tmp_b,wire->GetWiresDiameter());
        KGMeshWire* meshwire2 = new KGMeshWire(tmp_b,tmp_x,wire->GetWiresDiameter());
        KGMeshWire* meshwire3 = new KGMeshWire(tmp_x,tmp_y,wire->GetWiresDiameter());
        RefineAndAddElement(meshwire1,meshcount_ends,1);
        RefineAndAddElement(meshwire2,meshcount_middle,1);
        RefineAndAddElement(meshwire3,meshcount_ends,1);


        KThreeVector tmp_r(tmp1,-tmp,z);
        KThreeVector tmp_t(test,-tmp,z);
        KThreeVector tmp_z(-test,-tmp,z);
        KThreeVector tmp_u(-tmp1,-tmp,z);
        KGMeshWire* meshwire4 = new KGMeshWire(tmp_r,tmp_t,wire->GetWiresDiameter());
        KGMeshWire* meshwire5 = new KGMeshWire(tmp_t,tmp_z,wire->GetWiresDiameter());
        KGMeshWire* meshwire6 = new KGMeshWire(tmp_z,tmp_u,wire->GetWiresDiameter());
        RefineAndAddElement(meshwire4,meshcount_ends,1);
        RefineAndAddElement(meshwire5,meshcount_middle,1);
        RefineAndAddElement(meshwire6,meshcount_ends,1);

        }
        else{
        int meshcount_ends=(tmp1+tmp1)/(0.005);

          KThreeVector tmp_a(tmp1,tmp,z);
          KThreeVector tmp_b(-tmp1,tmp,z);
          KThreeVector tmp_h(tmp1,-tmp,z);
          KThreeVector tmp_j(-tmp1,-tmp,z);
          KGMeshWire* meshwire2 = new KGMeshWire(tmp_h,tmp_j,wire->GetWiresDiameter());
          KGMeshWire* meshwire3 = new KGMeshWire(tmp_a,tmp_b,wire->GetWiresDiameter());

          RefineAndAddElement(meshwire2,meshcount_ends,1);
          RefineAndAddElement(meshwire3,meshcount_ends,1);

    }
        tmp=tmp+pitch;
    }
...
```

Listing 7.4: Discretization code for a wire mesh in DGeoBag

Listing 7.5 shows the code in DGeoBag to discretize a cylinder with rectangles.

```
...
    KThreeVector p0;
        KThreeVector p1;
        KThreeVector p2;
        KThreeVector p3;

        double th = 0;
        double th_last = 0;

        std::vector< double > dz( cylinder->GetLongitudinalMeshCount(), 0 );

        for( unsigned int i = 1; i <= cylinder->GetAxialMeshCount(); i++ )
        {
            th = ((double) (i % cylinder->GetAxialMeshCount())) / cylinder->GetAxialMeshCount()
                * 2. * M_PI;

            p0[ 0 ] = p3[ 0 ] = cylinder->GetRadius() * cos( th_last );
            p0[ 1 ] = p3[ 1 ] = -cylinder->GetRadius() * sin( th_last );
            p1[ 0 ] = p2[ 0 ] = cylinder->GetRadius() * cos( th );
            p1[ 1 ] = p2[ 1 ] = -cylinder->GetRadius() * sin( th );

            DiscretizeInterval( (cylinder->GetP1()[ 2 ] - cylinder->GetP0()[ 2 ]), cylinder->
                GetLongitudinalMeshCount(), cylinder->GetLongitudinalMeshPower(), dz );

            p0[ 2 ] = p1[ 2 ] = cylinder->GetP0()[ 2 ];
            for( unsigned int k = 0; k < cylinder->GetLongitudinalMeshCount(); k++ )
            {
                p2[ 2 ] = p3[ 2 ] = p0[ 2 ] + dz[ k ];

                KGMeshRectangle* r = new KGMeshRectangle( p0, p1, p2, p3 );
                AddElement( r );

                p0[ 2 ] = p1[ 2 ] = p2[ 2 ];
            }
            th_last = th;
        }
...
```

Listing 7.5: Discretization code for a cylinder.

# D. XENON1T Sketch

Figure D.13 shows the geometrical parameters of the XENON1T for the simulation.

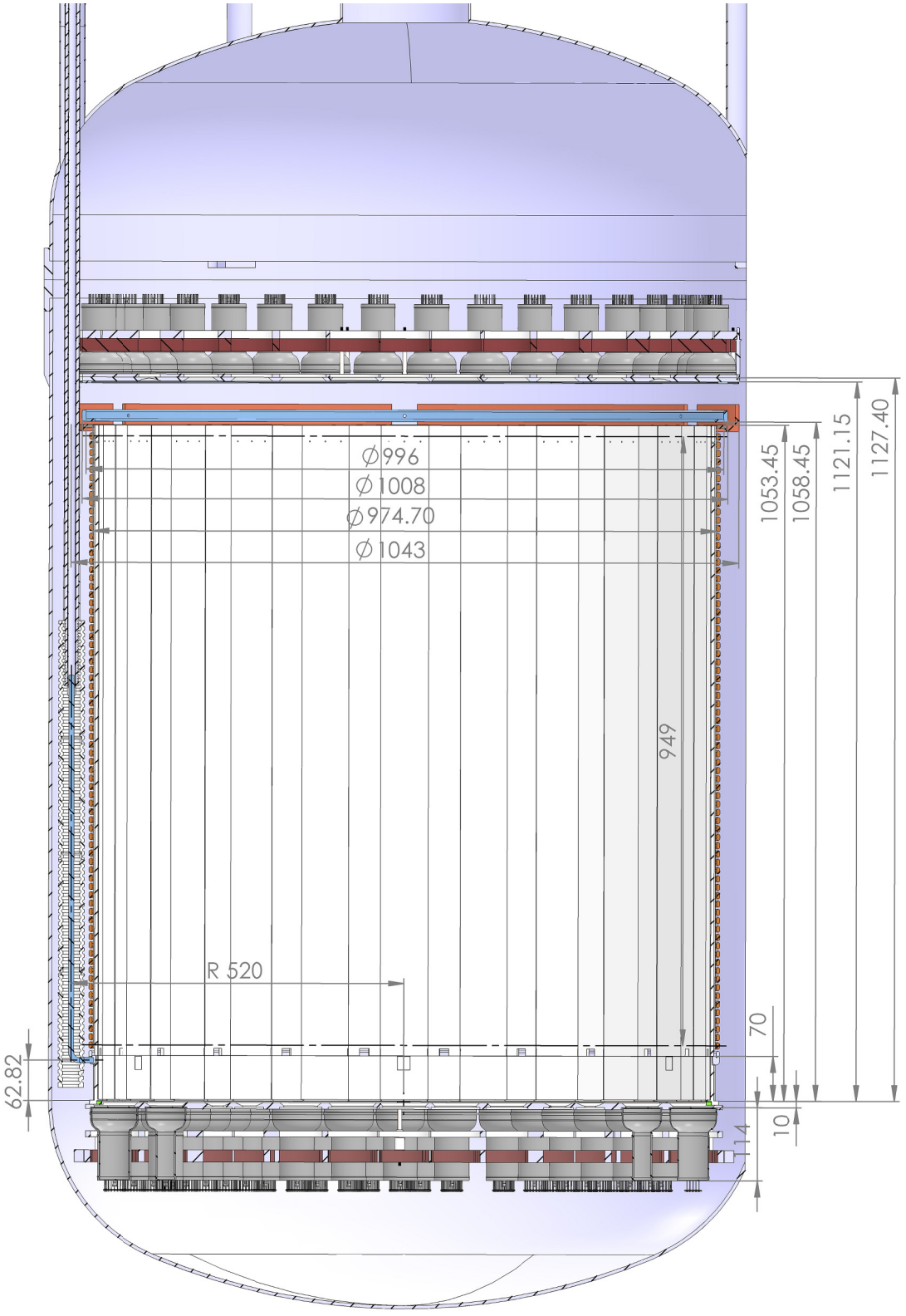


Figure D.13.: The XENON1T sketch for the implementation into the DARWIN module.

# E. Geometrical Parameters of the implemented Xenon1T Shapes

All the complex shapes of the XENON1T geometry, which have been impemented in DGeoBag are shown here. The CAD drawings are created in cooperation with the CAD workshop of the UZH.

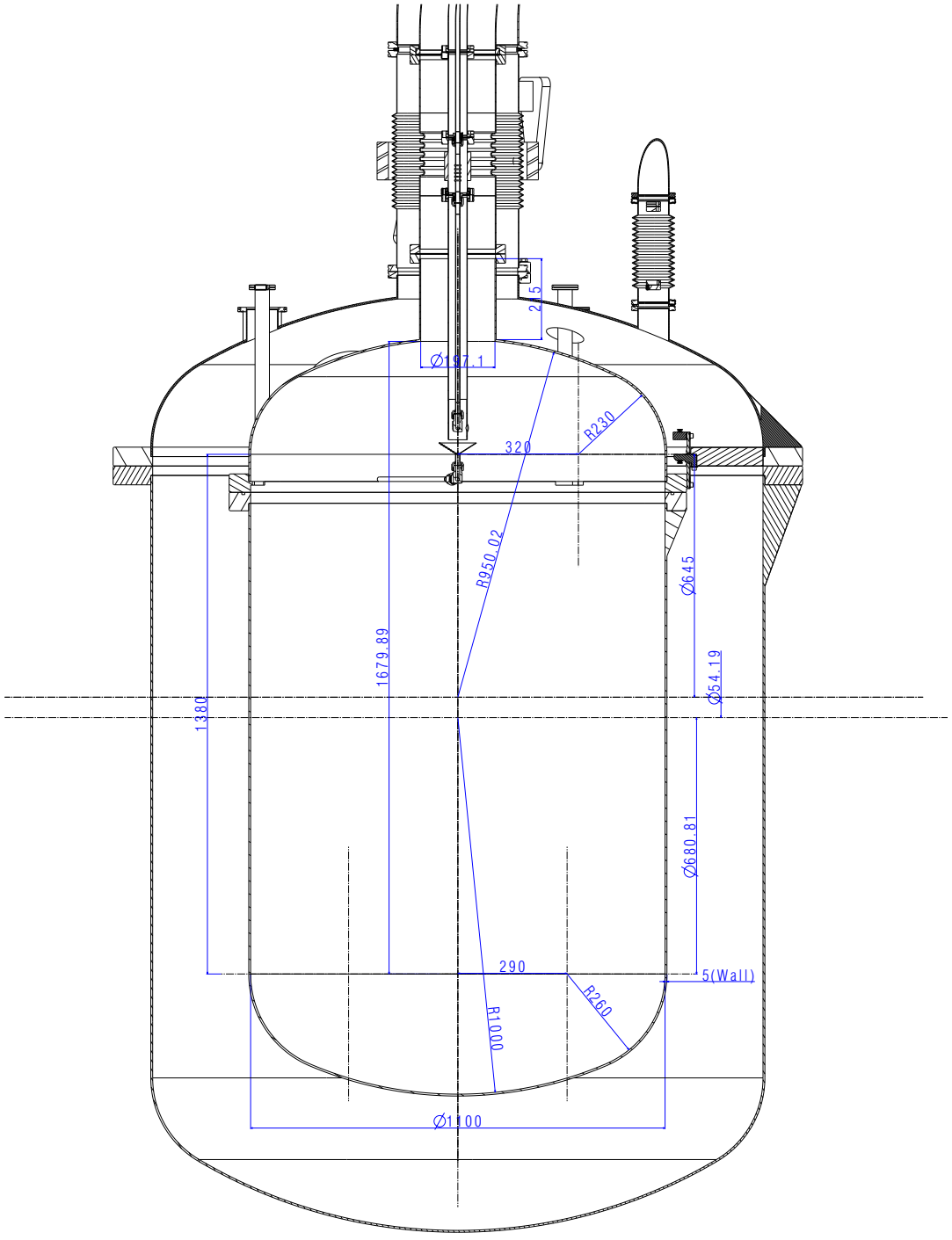


Figure E.14.: The Xenon1T cryostat. The geometrical parameters are shown.

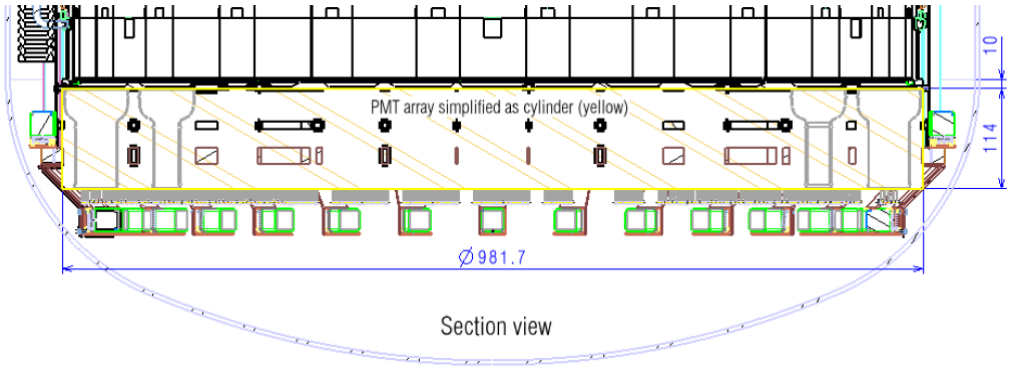


Figure E.15.: The bottom PMT array simplified with a cylinder. The geometrical parameters of the PMT array are shown.

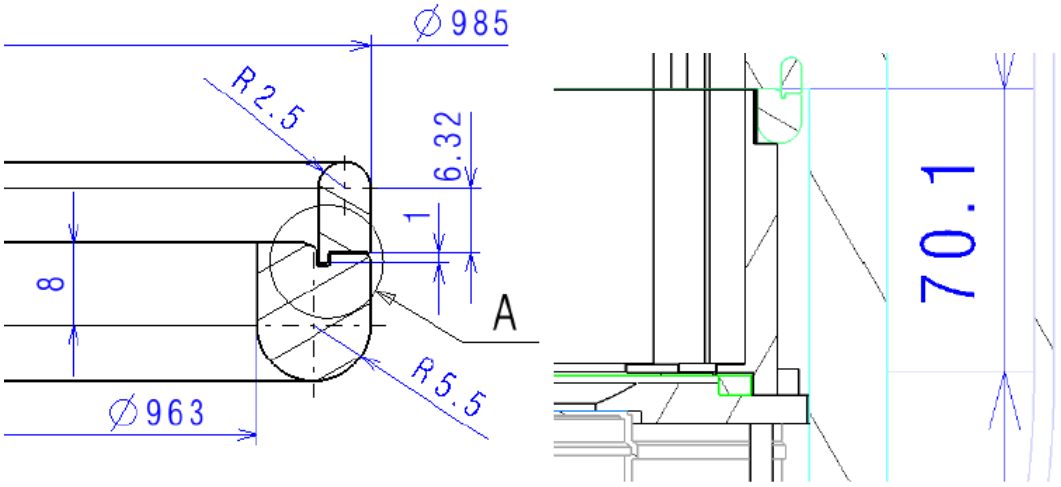


(a) The cathode holder design (b) The Position of the cathode

Figure E.16.: (a) The cathode holder with all geometrical parameters. (b) The position of the cathode holder inside the Xenon1T geometry.

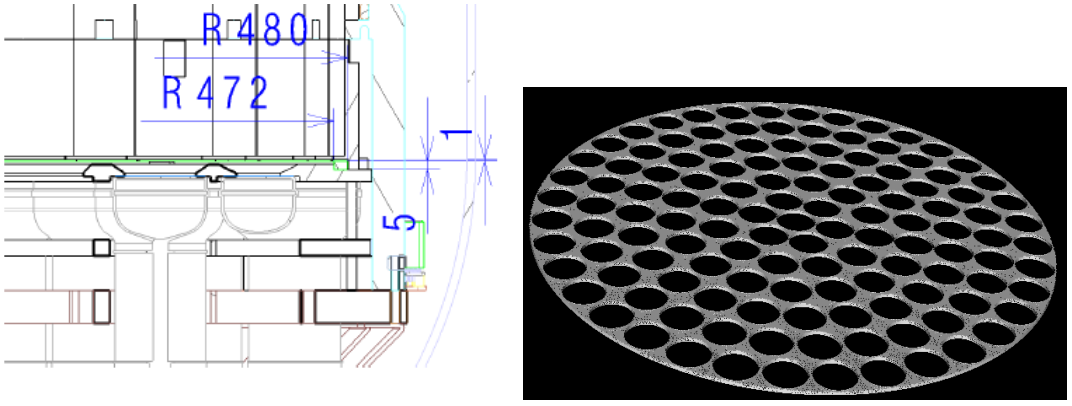


(a) The protection grid holder. (b) The imported Teflon part.

Figure E.17.: (a) The protection grid holder and some Teflon reflection parts. (b) The imported CAD drawing of a Teflon reflection part.

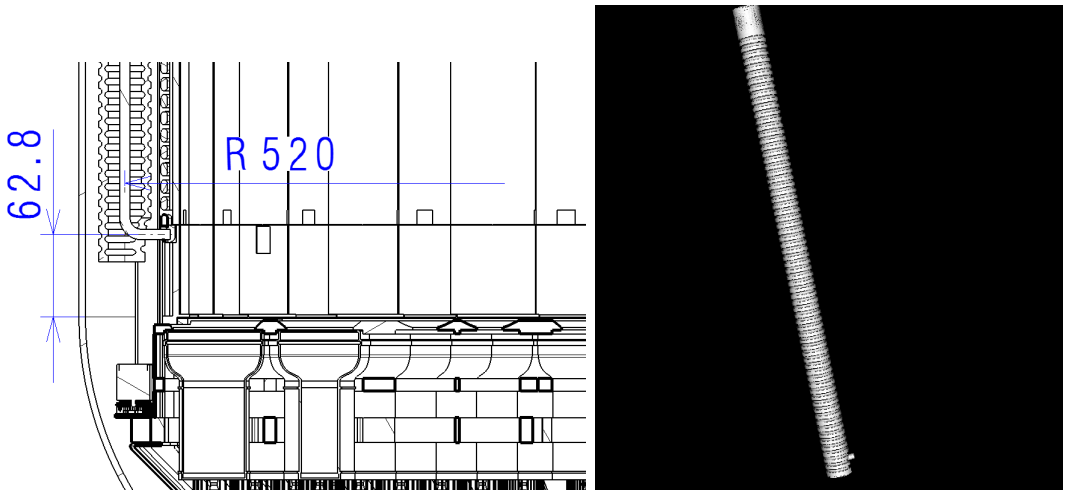


(a) The position of the high voltage power supply.

(b) The imported power supply and isolation.

Figure E.18.: (a) The position of the high voltage power supply. (b) The imported CAD drawing of the power supply and the isolation.

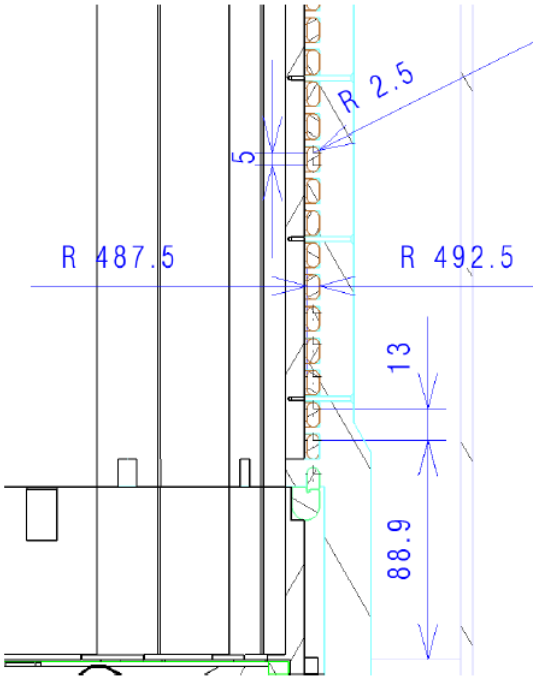


Figure E.19.: The geometrical parameters of the field shaping rings and the Teflon reflection wall. Xenon1T consists of 76 field shaping rings. The position of the rings is also shown.

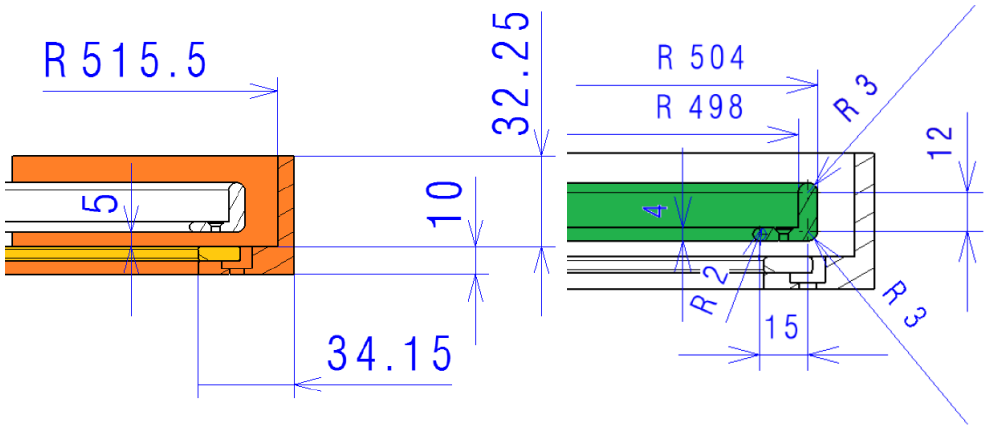


(a) The Gate holder design (b) The Anode holder design

Figure E.20.: (a) The gate holder with all geometrical parameters. (b) The anode holder with all geometrical parameters.

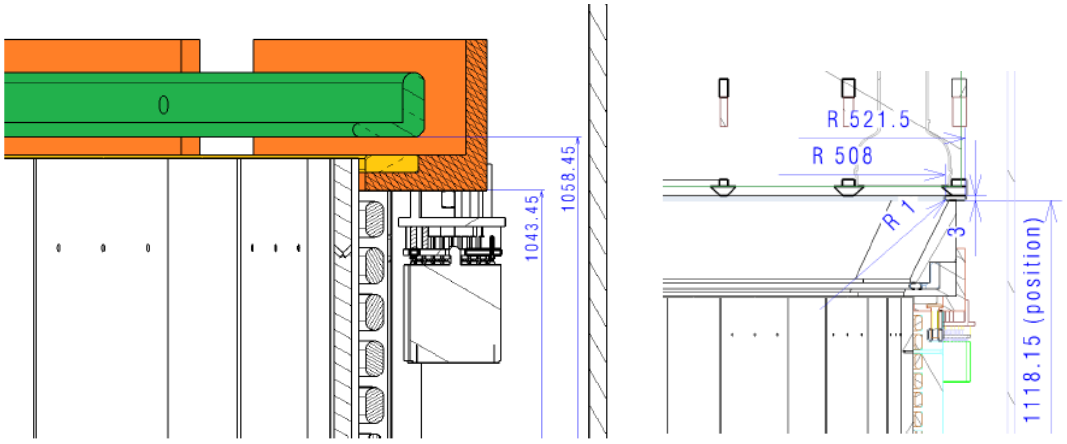


(a) The position of the Gate holder and anode holder. (b) The top assembly.

Figure E.21.: (a) The position of the Gate holder and anode holder inside the geometry. (b) The Position of the top PMT array, the Teflon reflection part and the protection grid holder.

# F. 7-Point Numerical Cubature

Listing 7.6 shows the implemented calculation routine for the potential of a triangle with the 7-Point numerical cubature .

```
...
    KPosition p = source->GetP0() - P;

   // define a characteristic size for computation of distance ratio
    double sideA( source->GetA() );
    double sideB( source->GetB() );
    double sideC( (source->GetP2()-source->GetP1()).Magnitude() );

    // determine distance ratio
    double distanceRatioFactor( p.Magnitude()/((sideA+sideB+sideC)/3.) );

    //Gaussian weights
    const double w3[3]={270/1200.,(155.+sqrt(15.))/1200.,(155.-sqrt(15.))/1200.};

    //
    double w[7];
    double Sum,R,R3,c;
    double Phi( 0. );

  //distance ratio > 60 => 7-point cubature
    if (distanceRatioFactor>60){
          const double ceps0( 1./(4.*KEMConstants::Pi*KEMConstants::Eps0) );
        double Area( source->Area() );
        KEMThreeVector Q[7];


        KEMThreeVector A(source->GetP0());
        KEMThreeVector B(source->GetP1());
        KEMThreeVector C(source->GetP2());

      //alpha, beta, gamma
          int i,j;
        const double c3=1./3.;
        const double alpha[3]={c3,0.059715871789770,0.797426985353087};
        const double beta[3]={c3,0.470142064105115,0.101286507323456};
        const double gamma[3]={c3,0.470142064105115,0.101286507323456};

         //Q = Position of the point charges
        Q[0]=alpha[0]*A+beta[0]*B+gamma[0]*C;
        j=1;
        Q[1]=alpha[j]*A+beta[j]*B+gamma[j]*C;
        Q[2]=beta[j]*A+alpha[j]*B+gamma[j]*C;
        Q[3]=gamma[j]*A+beta[j]*B+alpha[j]*C;
        j=2;
        Q[4]=alpha[j]*A+beta[j]*B+gamma[j]*C;
        Q[5]=beta[j]*A+alpha[j]*B+gamma[j]*C;
        Q[6]=gamma[j]*A+beta[j]*B+alpha[j]*C;

         // "Charge calculation" of the point charges. Sum of all charges is equal to the unit
             charge
          w[0]=w3[0];
          for(int i=1;i<=3;i++)
           w[i]=w3[1];
          for(int i=4;i<=6;i++)
           w[i]=w3[2];
     Sum=0.;
     for(int i=0;i<=6;i++)
     {
      R=(P-Q[i]).Magnitude();
      c=1./R;
      Sum+=w[i]*c;
     }
     //phi = 1/4\pi\epsilon_0 \int_A 1/(\vec{P}-\vec{Q})dA = 1/4\pi\epsilon_0 \cdot A \sum_{i=1}^{ng} w_i/(\vec{P}-\vec{Q}_i)
     Phi=Area*ceps0*Sum;

     return Phi;
...
```

Listing 7.6: The implemented code for the calculation of the triangle potential at a field point P with the 7-point numerical cubature.

Listing 7.7 shows the implemented calculation routine for the electric fields of a triangle with the 7-Point numerical cubature .

```
...
          double w[7];
          double Sum=0;
          double R=0;
          double R3=0;
          double c=0;
          double Phi( 0. );
          double Area=0;

         double sideA( source->GetA() );
         double sideB( source->GetB() );
         double sideC( (source->GetP2()-source->GetP1()).Magnitude() );

         const double ceps0( 1./(4.*KEMConstants::Pi*KEMConstants::Eps0) );
            Area=( source->Area() );
            KEMThreeVector Q[7];
           KEMThreeVector SumE(0,0,0);

            KEMThreeVector A(source->GetP0());
        KEMThreeVector B(source->GetP1());
            KEMThreeVector C(source->GetP2());

           int i,j;
            const double c3=1./3.;
            const double alpha[3]={c3,0.059715871789770,0.797426985353087};
            const double beta[3]={c3,0.470142064105115,0.101286507323456};
            const double gamma[3]={c3,0.470142064105115,0.101286507323456};

        //Q = Position of the point charges
            Q[0]=alpha[0]*A+beta[0]*B+gamma[0]*C;
            j=1;
            Q[1]=alpha[j]*A+beta[j]*B+gamma[j]*C;
            Q[2]=beta[j]*A+alpha[j]*B+gamma[j]*C;
            Q[3]=gamma[j]*A+beta[j]*B+alpha[j]*C;
            j=2;
            Q[4]=alpha[j]*A+beta[j]*B+gamma[j]*C;
            Q[5]=beta[j]*A+alpha[j]*B+gamma[j]*C;
            Q[6]=gamma[j]*A+beta[j]*B+alpha[j]*C;
           // "Charge calculation" of the point charges. Sum of all charges is equal to the unit
               charge
            w[0]=w3[0];
            for(int i=1;i<=3;i++)
                w[i]=w3[1];
            for(int i=4;i<=6;i++)
                w[i]=w3[2];
        Sum=0.;
        double sq=0;
        SumE.SetComponents(0.,0.,0.);
        for(int i=0;i<7;i++)
        {
           R=(P-Q[i]).Magnitude();
           sq=1./R;
           R3=sq*sq*sq;
           SumE+=(w[i]*R3)*(P-Q[i]);
        }


        field=(Area*ceps0)*SumE;

    return field;
...
```

Listing 7.7: The implemented code for the electric field calculation of a triangle with the 7-point numerical cubature.

Figure F.22 shows the electric field $E_z$ of the KATRIN experiement at x=2 m, y=0 m, z=7 m calculated analytically with the newton-leibniz integrals. Figure F.23 shows the electric field $E_z$ of the KATRIN experiment at x=2 m, y=0 m, z=7 m calculated with the 7-point numerical cubature.

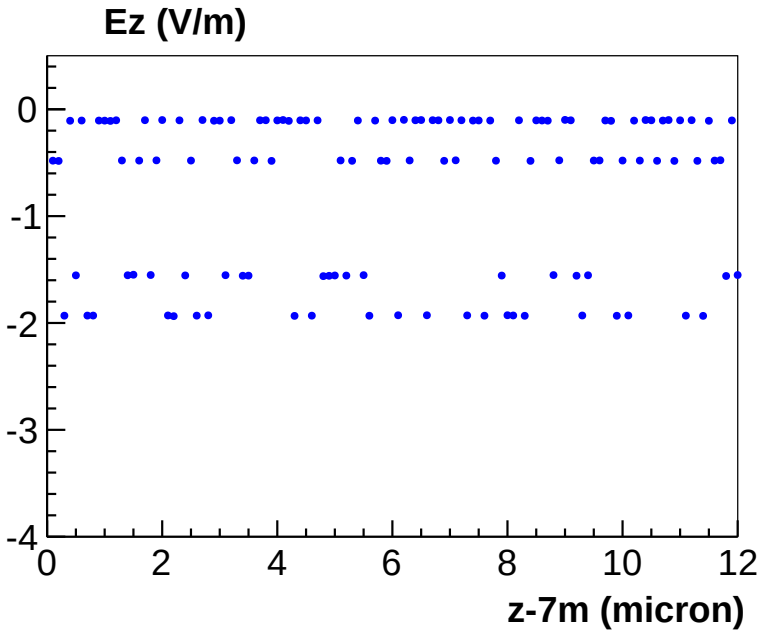


Figure F.22.: The electric field $E_z$of the KATRIN calculated analytically along the z-axis

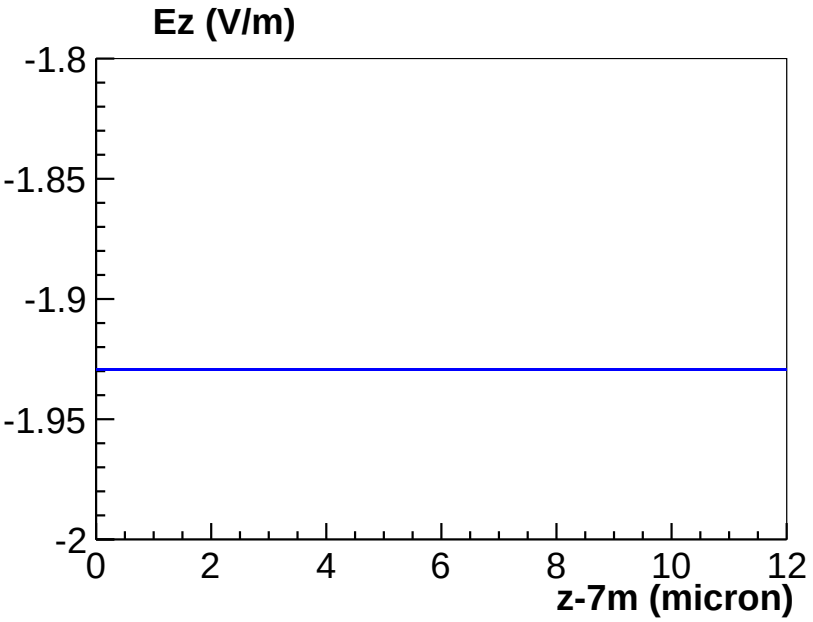


Figure F.23.: The electric field $E_z$ of KATRIN experiment calculated with the 7-point numerical cubature along the z-axis

# G. PMT Spectra of the Amplifier PMT Test

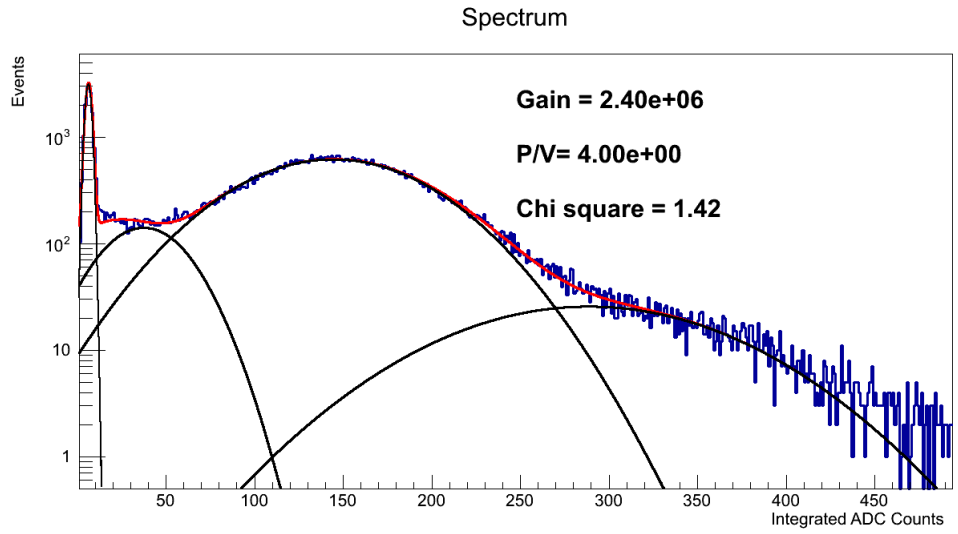


Figure G.24.: The PMT spectrum of PMT1 with the Philipps amplifier. The noise peak, single-photo-electron-Peak (SPE) and the second SPE peak are fitted with Gaussian functions. The plateau between the noise peak and the SPE-peak is not clearly understood and also fitted with a Gaussian function.

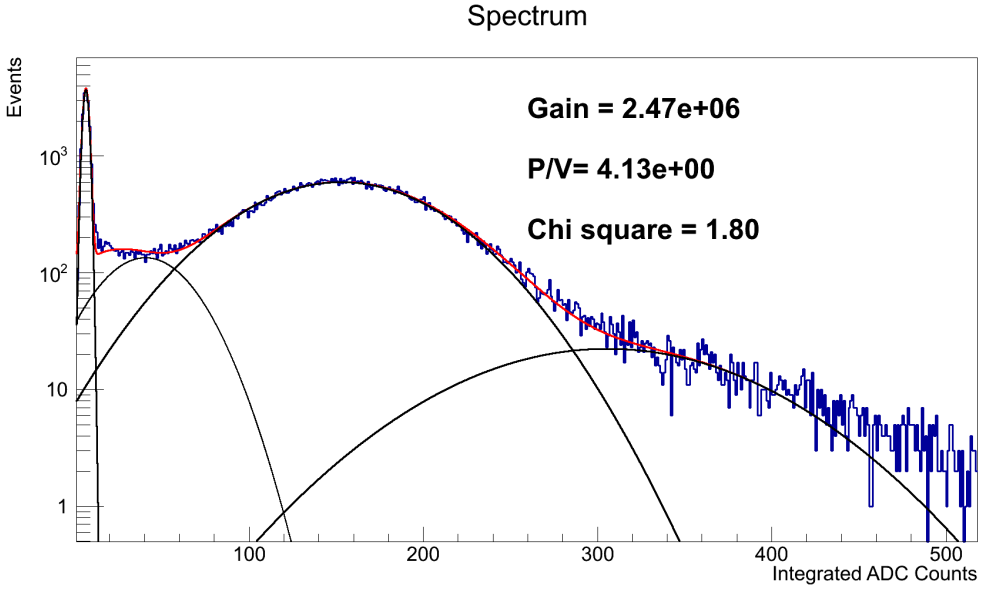


Figure G.25.: The PMT spectrum of PMT1 with the UZH amplifier. The noise peak, single-photo-electron-Peak (SPE) and the second SPE peak are fitted with Gaussian functions. The plateau between the noise peak and the SPE-peak is not clearly understood and also fitted with a Gausian function.

# H. Calibration Curves of the Bell Test

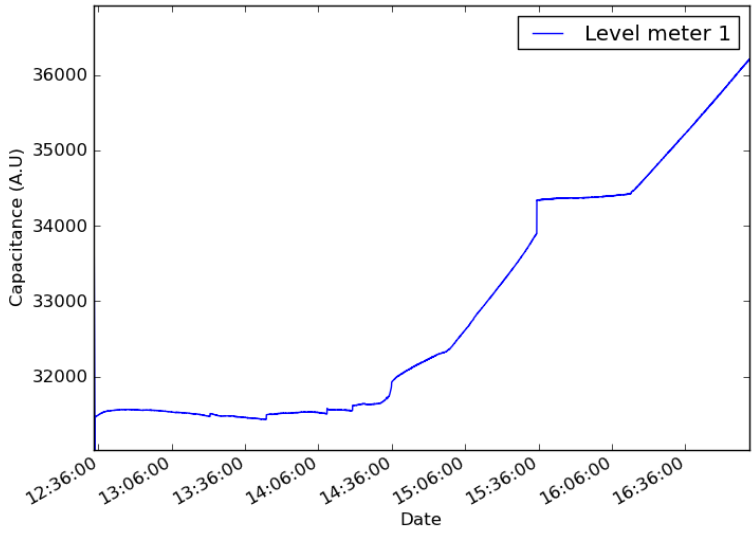


Figure H.26.: The filling curve of the level meter 1. This curve is used to calibrate level meter 1. The step comes from the installed Teflon spacer inside the capacitor.

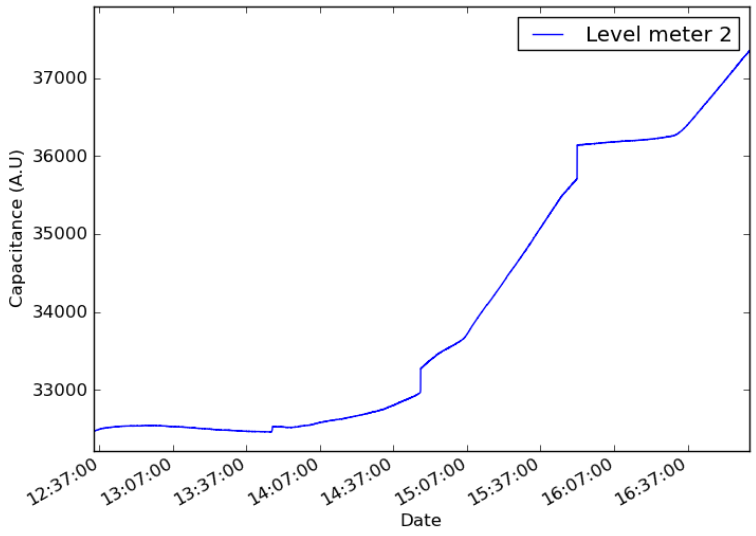


Figure H.27.: The filling curve of the level meter 2. This curve is used to calibrate level meter 2. The step comes from the installed Teflon spacer inside the capacitor.

# List of Figures

# List of Tables

# Acknowledgements

First of all, I would like to thank my first advisor, Prof. Dr. Guido Drexlin, who gave me the opportunity to write my master's thesis in such an exciting field and gave me the chance to do partly my thesis in Switzerland. A special thanks to Prof. Dr. Wim de Boer for being the second reviewer of this thesis. I want to thank Prof. Dr. Laura Baudis, who looked very well after me during my time in Switzerland and gave me the opportunity to present my results at the DARWIN meeting in Naples. She made me feel very welcome at the UZH. It has been a pleasure to be a member of the KATRIN group in Karlsruhe and the XENON group in Zürich. I want to thank both groups for supporting me.
I thank Dr. Martin Auger for his numerous helpful advices, suggestions and for showing me that you can learn from every mistake. With Dr. Alexander Kish I had a good time in Naples during the DARWIN meeting. It was a pleasure to work with you. Thanks to Dr. Ferenc Glück for helping with all the theoretical aspects for a good simulation. He is always willingness to help and finds always a solution for an existing problem. I want to thank Dipl.-Phys Manuel Walter, my office partner in Switzerland, from whom I learned a lot about PMTs. Thanks to M.Sc. Thomas Joseph Corona, a Ph.D. student from the UNC, for all the help with the simulation package *KEMField*. I want to thank Dipl.-Phys. Daniel Hilk for being a very good advisor. He always looked very well after me and thanks for proofreading my work. Also a special thanks to Andreas James, the technical assistant in Zürich, who made a lot of CAD drawings for me and helped me with the construction of several experiments. I also want to thank all my friends in Karlsruhe for having all the great moments during my almost seven years in Karlsruhe.
I have to thank my family for supporting me during the years of study. I am especially grateful to my dear mother. Thank you very much for supporting everything I have been doing, without you I would have never made it. I also want to thank my father, who always encouraged me to do my best and showed me that science is a very interesting topic. I think you would be very proud of me.
The lasting gratitude is to my lovely girlfriend Simone, who has been a great support during my studies and life in Karlsruhe and Zürich. She continuously encouraged me to do my best and she was always there for me when I needed her most. Thank you for the patience and help in difficult moments.